edgeFLEX

D2.3 v1.0

Frequency Control Concepts for Energy Communities with future VPPs

The research leading to these results has received funding from the European Union's Horizon 2020 Research and Innovation Programme, under Grant Agreement no 883710.

Project Name:	edgeFLEX
Contractual Delivery Date:	31.03.2022
Actual Delivery Date:	31.03.2022
Authors:	Georgios Tzounas (UCD), Federico Milano (UCD)
Workpackage:	WP2 – Frequency and Inertia Response Control Concept for Dynamically Controlled VPP Solutions
Security:	P
Nature:	R
Version:	V1.0
Total number of pages:	65

Abstract

This deliverable describes the frequency control concepts and algorithms developed for future virtual power plants and energy communities. These include a new theoretical concept for modeling, estimation and control of frequency variations; a set of combined voltage-frequency controllers for distributed energy resources and virtual power plants; an aggregated virtual power plant model for system-wide transient stability studies; and a stochastic decentralized control strategy for charging large fleets of plug-in electric vehicles. All algorithms are tested through computer-based simulations according to the relevant scenarios defined in deliverable D2.1.

Keyword list

Frequency control, virtual power plants, distributed energy resources, converter-interfaced generation, energy storage systems, electric vehicles, power system dynamics.

Disclaimer

All information provided reflects the status of the edgeFLEX project at the time of writing and may be subject to change.

Executive Summary

This deliverable, which is the major output of task T2.3 in the work package WP2 of edgeFLEX, describes the frequency control concepts and algorithms developed for future Virtual Power Plants (VPPs) and Energy Communitys (ECs). These include a new theoretical concept for modeling, estimation and control of frequency variations; a set of combined primary voltage-frequency control schemes for Distributed Energy Resources (DERs) and VPPs; an aggregated VPP model for system-wide transient stability analysis studies; and a stochastic decentralized control strategy for charging large fleets of Plug-in Electric Vehicles (PEVs). All algorithms are tested through computer-based simulations according to the relevant scenarios defined in deliverable D2.1.

Revealing the meaning of frequency as well as the link between frequency and power variations at the buses of modern power networks is an open research topic and an important problem for system operators. The deliverable generalizes the concepts of the frequency divider and rate of change of regulating power described in deliverable D2.2, to introduce a new quantity, namely, the Complex Frequency (CF), The most significant property of the CF is its ability to give a more robust and clean indication of frequency than the current state-of-art, especially to describe the behavior of frequency variations at buses close to a disturbance. The proposed definition of CF is in accordance with the commonly accepted definition of frequency and generalizes it.

A relevant aspect of DER and VPP regulation is the utilization of the active and reactive control loops and which control signals are dedicated to which control objectives. In this vein, the deliverable takes advantage of the theory on CF to present two control schemes. First, a technique is presented based on a voltage feedback that improves the effectiveness of the Primary Frequency Control (PFC) provided by DERs. This technique relies on remote bus voltage measurements and consists in modifying the reference of the DER voltage control loop. Second, a combined control scheme for DERs and VPPs is presented in which both active and reactive power injections are modified to compensate both for frequency and voltage variations. An important aspect that impacts on the effectiveness of both control schemes is the sensitivity of loads to voltage variations. Accordingly, the deliverable also provides a novel approach to identify accurately and in real-time the parameters of Voltage-Dependent Loads (VDLs).

The operation of the Distributed Generator (DG) units that compose a VPP may rely either on a Grid-Following (GFL) or Grid-Forming (GFM) control strategy. To be able to capture the effects of both strategies on system-wide transient stability studies, the deliverable also proposes an aggregated model that accurately reproduces the dynamic response of VPPs following a disturbance. The proposed VPP model consists of a voltage source and a current source connected in parallel, with a scope to emulate the respective synchronization transients of GFL and GFM-based DGs.

Finally, the deliverable studies the flexibility provision by ECs and provides an efficient algorithm to control PEV chargers by dynamically allocating the available power in an optimized way and without affecting the system stability. The proposed approach is based on an Additive-Increase-Multiplicative-Decrease (AIMD) stochastic decentralized control strategy that manages the charging of PEVs with little communication efforts, and is particularly suited for large numbers of PEVs.

Authors

Partner	Name	e-mail
UCD		
	Georgios Tzounas	georgios.tzounas@ucd.ie
	Federico Milano	federico.milano@ucd.ie

Table of Contents

1. Introduction

1.1 Task 2.3: Frequency Control for Energy Communities with Future VPPs

This deliverable is the major output of task T2.3 in the work package WP2. The main goal of T2.3 is to define novel control concepts for VPPs. Two main approaches are considered. The first is a fully decentralised approach based on a stochastic control approach which requires minimum communications among distributed generation and Energy Storage Systems (ESSs) and guarantees high scalability. The second approach is based on a hybrid centralised/decentralised control. The centralised part of the control is run only at given times (e.g., every 5 minutes) and solves an optimisation problem to properly allocate power and inertia reserves among the resources that compose the VPP. With this aim, each resource has to communicate its current operating point (e.g., state of charge), reserve and generation forecast for the next period to the VPP control centre. The decentralised part of the control is based on a fast frequency control.

1.2 Objectives and Outline of the Deliverable

This deliverable aims at describing the frequency control algorithms developed for ECs with future VPPs. A new theoretical concept that helps better understand and capture the frequency variations in a power network is presented first. Second, two combined voltage-frequency control schemes that efficiently utilize the active and reactive control loops of converter-based resources are proposed. In practice, the performance and tuning of these control schemes depend on the knowledge of the sensitivity of loads to voltage variations and thus, accurate formulas to capture this sensitivity are also provided. Then, an aggregated dynamic model for VPPs consisting of both GFL and GFM-based resources is developed. Finally, an efficient algorithm to control the charging of large fleets of PEVs in an optimized and decentralized way is presented.

1.3 How to Read this Document

The frequency control concepts presented in this deliverable are tested based on the relevant scenarios and using the data and component models provided in deliverable D2.1. Note that the scenario and model description in D2.1 has been revisited and proper modifications and updates are provided in Sections A.1 and A.2 of this deliverable. We thus encourage the reader to go through this document while referring in parallel, first, to the material presented in D2.1 and, second, to Sections A.1 and A.2 of the present deliverable, whenever relevant. Dependencies and links of task T2.3 with other tasks within WP2, as well as of WP2 with other work packages from edgeFLEX, including WP3, WP4, and WP5, are summarized in Figure 1.

1.4 Structure of the Deliverable

The remainder of this deliverable is organized as follows. Chapter 2 proposes the novel concept of CF. Chapter 3 describes two combined voltage-frequency control schemes for DERs and VPPs, as well as proper formulas to estimate the voltage-dependency of loads. Chapter 4 provides an aggregated VPP model for system-wide transient stability studies. Chapter 5 presents a decentralized charging strategy for PEVs. Finally, the deliverable is summarized and conclusions are drawn in Chapter 6.

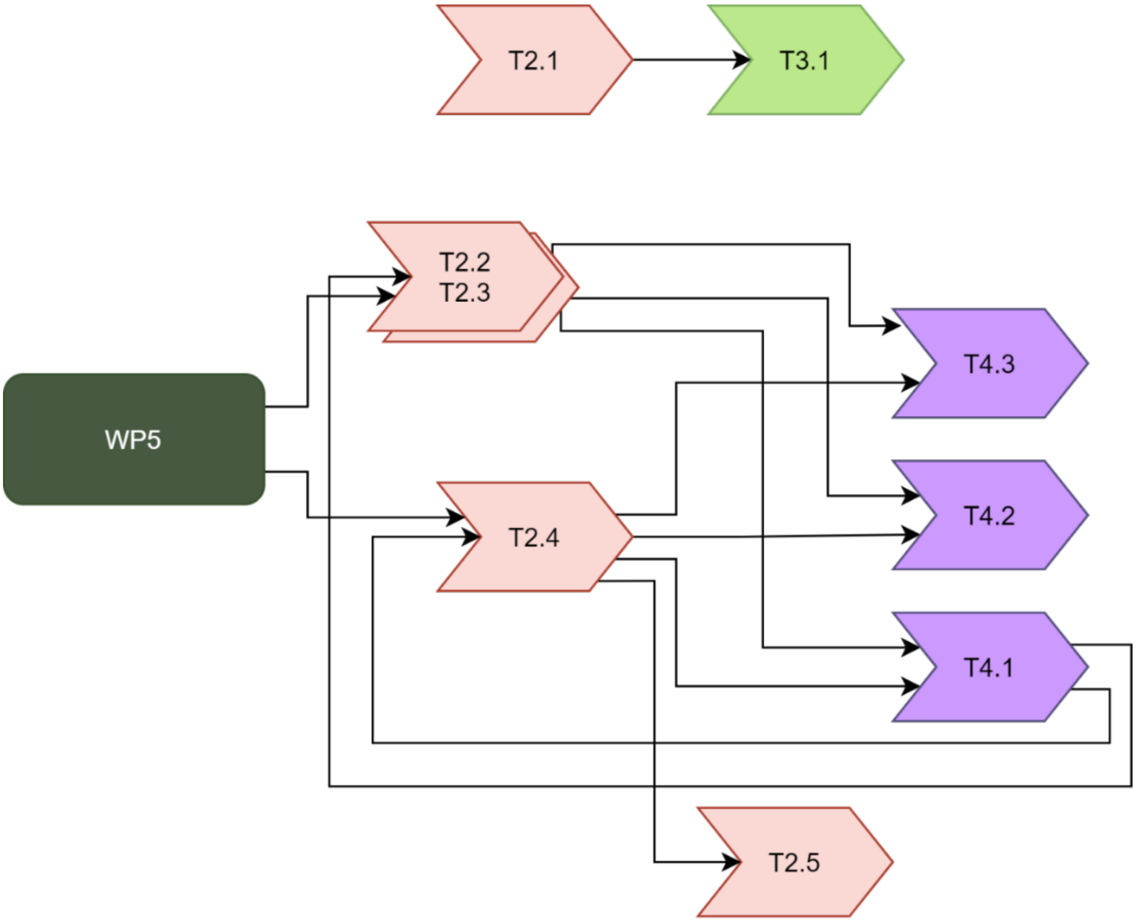

Figure 1 – Relations between WP2 and other work packages

2. The Complex Frequency Concept

2.1 Introduction

A well-known and accepted definition of the frequency of a signal $x(t) = X_m(t)\,\cos\vartheta(t)$ is given in the IEEE Standard IEC/IEEE 60255-118-1 [1], as follows:

$$f(t) = \frac{1}{2\pi}\dot{\vartheta}(t) = \frac{1}{2\pi}\dot{\theta}(t) + f_o\,, \tag{2.1}$$

where θ is the phase difference, in radians, between the angular position ϑ, also in radians, of the signal $x(t)$ and the phase due to the reference nominal frequency f_o, expressed in Hz. If the magnitude X_m of the signal is constant, this definition is adequate. However, if X_m changes with time, the definition of the frequency in (2.1) does not provide a meaningful way to separate the effects of the variations of ϑ and X_m. Thus, the definition of frequency in the most general conditions is a highly controversial concept that has been discussed at length in the literature (e.g. see the interesting discussion in [2] and the references therein).

This chapter provides a novel interpretation of “frequency” as complex quantity. This CF takes into account the time dependency of both ϑ and X_m. The CF allows a neat and compact representation as well as a consistent interpretation of frequency variations in AC power systems. The CF is also capable of explaining the interactions among active and reactive power injections at buses and flows in network branches. It is important to note that the proposed approach does not attempt to substitute the modeling approaches that go beyond the classical phasor representation or that focus on analysis of non-sinusoidal signals (see, for example, [3] for a state-of-the-art survey on this topic and the several references therein). On the contrary, the proposed concept of CF is compatible with the approaches that have been proposed in the literature as it allows interpreting angle and magnitude variations as complementary components of the same phenomenon, provided that one accepts to extend the domain of frequency to the complex numbers.

This chapter focuses on electro-mechanical transients in high-voltage transmission systems. Thus, the starting point is similar to that of [4, 5, 6, 7], that is, the transient conditions during which the magnitude and the phase angle of bus voltage phasors vary, change according to the inertial response of Synchronous Machines (SMs) and the frequency control of synchronous and non-synchronous devices. On the other hand, harmonics, unbalanced conditions and electro-magnetic transients are not taken into consideration. The resulting formulation is:

- *exact*, in the measure that power system models based on the dqo transform for voltage and angle stability analysis are exact;
- *general*, as it provides a framework to study the dynamic effect of any device on the local frequency variations at network buses; and
- *systematic*, because it provides the tools to determine analytically the impact of each device on bus frequencies.

2.2 Background

The starting point is the set of equations that describe the complex power injections, in per unit, at the n network buses of the system, say $\bar{\boldsymbol{s}} \in \mathbb{C}^n$, as follows:

$$\bar{\boldsymbol{s}}(t) = \boldsymbol{p}(t) + \jmath\boldsymbol{q}(t) = \bar{\boldsymbol{v}}(t) \circ \bar{\boldsymbol{\imath}}^*(t)\,, \tag{2.2}$$

where $\boldsymbol{p} \in \mathbb{R}^{n\times 1}$, $\boldsymbol{q} \in \mathbb{R}^{n\times 1}$ are the active and reactive power injections at network buses, respectively; $\bar{\boldsymbol{v}} \in \mathbb{C}^{n\times 1}$ and $\bar{\boldsymbol{\imath}} \in \mathbb{C}^{n\times 1}$ are the voltages and current injections at network buses; $*$ indicates the complex conjugate; and $\circ$ is the element-by-element product of two vectors. In steady-state, balanced conditions, (2.2) expresses the power flow equations. However, it is important to note that, in (2.2), all quantities are assumed to be time-dependent. The elements of $\bar{\boldsymbol{v}}$ and $\bar{\boldsymbol{\imath}}$ that appear in (2.2), in fact, are not to be interpreted as conventional phasors, but as dynamic quantities, which in some studies are called *Park's vectors* [8, 9]. A Park's vector is a complex quantity obtained from the dq-axis components of the well-known dqo transform. For example, for the voltage, one has:

$$\bar{\boldsymbol{v}}(t) = \boldsymbol{v}_{\mathrm{d}}(t) + \jmath \boldsymbol{v}_{\mathrm{q}}(t) \,, \tag{2.3}$$

where the components $v_{\mathrm{d},k}$ and $v_{\mathrm{q},k}$ of the k-th element of the vector $\bar{\boldsymbol{v}}$ are calculated as follows:

$$\begin{bmatrix} v_{\mathrm{d},k}(t) \\ v_{\mathrm{q},k}(t) \\ v_{\mathrm{o},k}(t) \end{bmatrix} = \mathbf{P}(t) \begin{bmatrix} v_{\mathrm{a},k}(t) \\ v_{\mathrm{b},k}(t) \\ v_{\mathrm{c},k}(t) \end{bmatrix} , \quad \mathbf{P}(t) = \sqrt{\tfrac{2}{3}} \begin{bmatrix} \cos(\theta_o(t)) & \cos(\theta_o'(t)) & \cos(\theta_o''(t)) \\ \sin(\theta_o(t)) & \sin(\theta_o'(t)) & \sin(\theta_o''(t)) \\ \frac{1}{\sqrt{2}} & \frac{1}{\sqrt{2}} & \frac{1}{\sqrt{2}} \end{bmatrix} , \tag{2.4}$$

where θ_o is the angle between phase a and the q-axis, with $\dot{\theta}_o = \omega_o$, $\theta_o' = \theta_o - \frac{2\pi}{3}$, and $\theta_o'' = \theta_o + \frac{2\pi}{3}$. Transformation (2.4) is also applied to the abc currents. Since no assumption is made on the abc quantities, the d- and q-axis components of Park's vectors $\bar{\boldsymbol{v}}$ and $\bar{\boldsymbol{\imath}}$ and, hence, (2.2) can be assumed to be valid in transient conditions. It is important to note that the reactive power is not well-defined for non-sinusoidal signals, e.g. see [10]. However, it is a common assumption, which effectively underpins the vast majority of studies on the transient stability of power systems [11], to approximate the reactive power as in (2.2). $v_{\mathrm{o},k}$ is the o-axis or *zero* component and is null for balanced systems. If the system is not balanced and the o-axis components are not null, then the vector $\boldsymbol{p}$ in (2.2) does not represent the total active power injections at network buses as it does not include the term $\boldsymbol{v}_{\mathrm{o}} \circ \boldsymbol{\imath}_{\mathrm{o}}$. The hypothesis of balanced system is not necessary for the developments presented below. However, since the focus is on high-voltage transmission systems, in the remainder of this chapter, balanced, positive sequence operating conditions are assumed.

For the purposes of the developments given below, it is convenient to rewrite (2.3) in polar form, as $\bar{\boldsymbol{v}}(t) = \boldsymbol{v}(t) \circ \angle\boldsymbol{\theta}(t)$, where $\boldsymbol{v} = |\bar{\boldsymbol{v}}|$, $\angle\boldsymbol{\theta} = \cos(\boldsymbol{\theta}) + \jmath \sin(\boldsymbol{\theta})$ and $\boldsymbol{\theta}(t) = \boldsymbol{\vartheta}(t) - \theta_o(t)$. $\boldsymbol{\theta}$ is the vector of bus voltage phase angles referred to the rotating dq-axis reference frame, $\boldsymbol{\vartheta}$ are the bus voltage phase angles referred to a stationary reference, $\theta_o = \int_t \omega_o dt$ is the angle of the rotating dq-axis reference frame and ω_o is the angular frequency in rad/s of the dq-axis reference frame. From (2.1), the time derivative of $\boldsymbol{\theta}$ gives $\boldsymbol{\omega}(t) = \dot{\boldsymbol{\theta}}(t) = \dot{\boldsymbol{\vartheta}}(t) - \omega_o(t)$, where $\boldsymbol{\omega}$ is the vector of frequency deviations with respect to the reference frequency at the network buses. In [1], it is assumed that $\omega_o = 2\pi f_o$ is constant and equal to the nominal angular frequency of the grid, e.g., $\omega_o = 2\pi\,50$ rad/s in European transmission grids. Note that ω_o being constant is not a requirement in (2.4). However, for the derivations presented below, ω_o is assumed to be constant when it is utilized to calculate the values of reactances and susceptances. As for the reactive power, this is again a widely-accepted approximation utilized in RMS models for angle and voltage stability analysis and consists in assuming that the link between current injections and voltages is given by:

$$\bar{\boldsymbol{\imath}}(t) \approx \bar{\mathbf{Y}}\, \bar{\boldsymbol{v}}(t) \,, \tag{2.5}$$

where $\bar{\mathbf{Y}} = \mathbf{G} + \jmath\mathbf{B} \in \mathbb{C}^{n \times n}$ is the well-known admittance matrix of the network. It is important not to confuse (2.5) with the conventional relationship between current and voltage phasors (in which case (2.5) is an exact equality). $\bar{\boldsymbol{\imath}}$ and $\bar{\boldsymbol{v}}$ are Park's vectors, i.e., complex quantities with time-varying real and imaginary parts and, hence, (2.5) represents an approximation of the dynamics of the grid. In turn, to obtain (2.5), it is assumed that, for network inductances and capacitances the relationships between voltages and currents can be approximated with:

$$\begin{aligned} \bar{v} &= L\dot{\bar{\imath}} = L(\frac{d}{dt} + \jmath\omega_o)\bar{\imath} \approx \jmath\omega_o L \bar{\imath} = \jmath X \bar{\imath} \,, \\ \bar{\imath} &= C\dot{\bar{v}} = C(\frac{d}{dt} + \jmath\omega_o)\bar{\imath} \approx \jmath\omega_o C \bar{v} = \jmath B \bar{v} \,, \end{aligned} \tag{2.6}$$

where $\frac{d}{dt}$ is the time derivative relative to the Park rotating frame; $\jmath\omega_o$ is the term due to the rotation of the Park reference; and L, C, X, B are the inductance, capacitance, reactance and susceptance, respectively. The quantities in (2.6) are assumed in absolute values. In turn, the approximation above assumes that electro-magnetic transients in the elements of the transmission lines and transformers are *fast* and can be assumed to be in Quasi-Steady State (QSS). The approximation (2.6) is applied also to the equations of the circuits of the devices connected to the grid, e.g., the equations of the SM. The focus of this chapter is, in fact, on the time scales of electro-mechanical and primary frequency and voltage control transients, which are a few orders of magnitude slower than electro-magnetic dynamics. Merging (2.2) and (2.5) yields:

$$\bar{\boldsymbol{s}}(t) = \bar{\boldsymbol{v}}(t) \circ [\bar{\mathbf{Y}}\,\bar{\boldsymbol{v}}(t)]^* \,. \tag{2.7}$$

These equations resemble the well-known power flow equations except for the fact that voltages are Park's vectors, not phasors, and, thus, bus power injections are, in general, time-varying quantities.

2.3 Formulation

According to the concept of the CF, the relationship between frequency variations and power flows in an AC grid is given by the following expression:

$$\dot{\bar{\boldsymbol{s}}} - \bar{\boldsymbol{s}} \circ \bar{\boldsymbol{\eta}} = \bar{\mathbf{S}}\,\bar{\boldsymbol{\eta}}^* \tag{2.8}$$

where $\bar{\mathbf{S}} \in \mathbb{C}^{n\times n}$ is a matrix whose (h,k)-th element is the complex power flow from bus h to bus k; and:

$$\bar{\boldsymbol{\eta}} \equiv \boldsymbol{\varrho} + \jmath\,\boldsymbol{\omega} \tag{2.9}$$

where $\bar{\boldsymbol{\eta}}$ is the vector of CFs of the buses of an AC grid. The derivation of (2.8) and (2.9) is provided in Section A.3 of the ANNEX. In (2.9), the imaginary part is the usual angular frequency (relative to the reference ω_o). On the other hand, the real part $\boldsymbol{\varrho}$ represents the transient rate of change of the bus voltages normalized with respect to their magnitude.

Equation (2.8) contains the information on how power injections of the devices connected to the grid impact on the frequency at their point of connection as well as on the rest of the grid. In (2.8), the elements of $\bar{s}$ are the inputs or *boundary conditions* at network buses and depend on the devices connected to grid, whereas $\bar{\mathrm{S}}$ depends only on network quantities. An alternative and more compact formulation to rewrite (2.8) is as a function of the currents, as follows:

$$\bar{\boldsymbol{v}} \circ \dot{\bar{\boldsymbol{\imath}}}^* = \bar{\mathbf{S}}\,\bar{\boldsymbol{\eta}}^* \tag{2.10}$$

or:

$$\dot{\bar{\boldsymbol{\imath}}} = \bar{\mathbf{I}}\,\bar{\boldsymbol{\eta}} \tag{2.11}$$

where $\bar{\mathbf{I}} = \bar{\mathbf{Y}}\,\mathrm{diag}(\bar{\boldsymbol{v}})$. The derivation of (2.10) and (2.11) is provided in Section A.3 of the ANNEX. As per (2.8), the right-hand sides of (2.10) and (2.11) depend exclusively on network quantities, whereas the left-hand side is device-dependent. While equivalent, the relevant feature of (2.10) and (2.11) with respect to (2.8) is that the CF vector only appears once.

Finally, (2.11) requires less calculations than (2.8). Thus, in a software where currents are modeled as states and, thus, their first derivatives are available as a byproduct of the integration of the system model, (2.11) can be an efficient alternative to (2.8) for the calculation of $\bar{\boldsymbol{\eta}}$.

2.4 Approximated Expressions

The developments of this chapter so far have assumed no simplifications except for neglecting the electro-magnetic dynamics of network branches. All formulas that have been deduced are thus accurate in the measure that the effects of electro-magnetic transients are negligible. In this section we discuss how the derived expressions can be approximated while retaining the information on the relationship between power injections and frequency variations at network buses.

Except during faults and some post-fault transients, it is not uncommon the case for which one can assume that $v_h \approx 1$ pu and that bus voltage phase angle differences are small, hence $\sin(\theta_h - \theta_k) \approx \theta_h - \theta_k$ and $\cos(\theta_h - \theta_k) \approx 1$. These assumptions, which, in turn, are the approximation utilized in the fast decoupled power flow method [12], lead to $\bar{s}_{hk} \approx \bar{Y}^*_{hk}$. Moreover, for high-voltage transmission systems, $\bar{\mathbf{Y}} \approx \jmath\mathbf{B}$. These approximations, allow obtaining the simplified expressions $\dot{\bar{\boldsymbol{s}}} - \bar{\boldsymbol{s}} \circ \bar{\boldsymbol{\eta}} \approx -\jmath\mathbf{B}$ and $\dot{\bar{\boldsymbol{\imath}}} \approx \jmath\mathbf{B}\,\bar{\boldsymbol{\eta}}$ [13]. Then, approximating the term $\bar{\boldsymbol{s}} \circ \bar{\boldsymbol{\eta}} \approx \bar{\mathbf{Y}}^*_{\mathrm{diag}}\bar{\boldsymbol{\eta}}$, where $\bar{\mathbf{Y}}_{\mathrm{diag}}$ is a matrix obtained using the diagonal elements of $\bar{\mathbf{Y}}$, and splitting the real and imaginary part of $\bar{\boldsymbol{\eta}}$, we arrive at:

$$\dot{\boldsymbol{p}}' \approx \mathbf{B}'\boldsymbol{\omega}\,, \tag{2.12}$$

$$\dot{\boldsymbol{q}}'' \approx \mathbf{B}''\boldsymbol{\varrho}\,, \tag{2.13}$$

where $B'_{hk} = -B_{hk}$ and $B'_{hh} = \sum_{h\neq k}^{n} B_{hk}$ are the elements of $\mathbf{B}'$; $B''_{hk} = -B_{hk}$ and $B''_{hh} = -2B_{hh}$ are the elements of $\mathbf{B}''$. (2.12) is the expression deduced in [7] and that, with due simplifications, leads to the Frequency Divider Formulas (FDFs), see [5, 14]. Considering the resistive parts of the network branches, the following dual expressions hold:

$$\dot{\boldsymbol{p}}'' \approx \mathbf{G}''\boldsymbol{\varrho}\,, \qquad \dot{\boldsymbol{q}}' \approx \mathbf{G}'\boldsymbol{\omega}\,, \tag{2.14}$$

where the elements of $\mathbf{G}'$, $\mathbf{G}''$ are defined as $G'_{hk} = G''_{hk} = -G_{hk}$, $G'_{hh} = \sum_{h\neq k}^{n} G_{hk}$, and $G''_{hh} = -2G_{hh}$. From (2.14) it descends that, in lossy networks, the reactive power can be utilized to regulate the frequency. The implications of this observation are further explored in Chapter 3. Combining together (2.12), (2.13) and (2.14) leads to the following approximated expressions:

$$\dot{\bar{\boldsymbol{s}}}' \approx \jmath\bar{\mathbf{Y}}'^{*}\,\boldsymbol{\omega}\,, \qquad \dot{\bar{\boldsymbol{s}}}'' \approx \bar{\mathbf{Y}}''\,\boldsymbol{\varrho}\,. \tag{2.15}$$

2.5 Simulation Results

Simulation results that illustrate the transient behavior of the CF as well as its accuracy in providing bus frequency estimations are presented in Section A.4.1 of the ANNEX based on Use Case FC_E.1 (see Section A.1.3).

3. Voltage-Frequency Control for Future DERs and VPPs

3.1 Introduction

Frequency regulation in power systems is traditionally provided by modifying the active power, while the reactive power is modified to regulate the voltage. This appears as an intuitive choice for conventional large-scale systems, where the active and reactive power flows are largely decoupled due to the highly inductive nature of transmission lines [15]. On the other hand, DERs are integrated within Distribution Networks (DNs), where the resistance/inductance ratio of feeders is large, thus leading to a strong interaction of active and reactive power with voltage and frequency, respectively. In this vein, a solution that has been proposed is to artificially impose the active/reactive power decoupling through the control of power converters, see e.g. the virtual impedance control approach [16, 17]. Instead, in this chapter we focus on the potential of exploiting the coupling between the active and reactive power for the design of efficient control loops that can improve the frequency and voltage regulation of the power grid.

Some recent studies have explored the ability of power electronics-based devices to regulate the frequency through voltage control. This concept of Voltage-based Frequency Control (VFC) effectively takes advantage of the sensitivity of loads to voltage variations. Examples of relevant applications include resources in small isolated systems [18], DERs integrated within microgrids [19], smart transformers [20], and Static Var Compensators (SVCs) installed at the transmission system level [21].

The focus of this chapter is on the utilization of DER active/reactive control loops and on which control signal is dedicated to which control objective. In this vein, the chapter presents two control schemes, as follows:

- Section 3.2 presents a technique based on a voltage feedback that improves the effectiveness of the PFC provided by DERs. This technique requires remote bus voltage measurements and consists in modifying the reference of the DER voltage control loop.
- Section 3.3 presents a combined control scheme for DERs and VPPs, in which both active and reactive power injections are modified to compensate both for frequency and voltage variations.

In both schemes, we keep each control loop simple yet practical, by employing standard filters and controllers widely used in industrial applications.

We note that, similarly to most controllers that mix the voltage and frequency feedback loops see e.g. [18, 19, 20], the effectiveness of the control schemes proposed in this chapter depend upon the sensitivity of loads to voltage variations. For the purpose of assessing these schemes through simulations, it is acceptable to assume that the voltage-dependency of loads is known *a priori*. However, in order to ensure that the performance of the proposed controls will not be compromised when put in practice, there is also a need for a way to accurately identify and track in real-time the voltage dependency of loads. With this in mind, Section 3.4 proposes an optimization-free method to estimate the parameters of VDLs through the measurements of only the load active and reactive power consumption and frequency deviations at the load bus. The technique is a relevant consequence of the CF concept described in Chapter 2. Both an exact and an approximated formulation of the method are discussed.

3.2 Frequency Control Through Modified Voltage Control Reference

This section presents a technique to improve the effectiveness of the PFC provided by DERs and ESSs, through synthesizing a proper voltage-based feedback signal. The feedback signal is utilized to modify the reference of the DER voltage control loop. The technique is a byproduct of the theoretical concepts introduced in Chapter 2 of this deliverable.

3.2.1 Description of Control Scheme

In standard DER voltage control schemes, the voltage reference is constant, at least for a given period. Hence, we have that:

$$v^{\rm ref}(t) = v_o^{\rm ref} = v_{h,o}\,, \tag{3.1}$$

where $v_o^{\rm ref}$ is the desired reference voltage and $v_{h,o}$ denotes the value, in steady-state, of the voltage magnitude at bus h where the DER is connected. Our goal in this section it to examine the effectiveness of modifying (3.1) by using a proper feedback signal that aims to mitigate the part of the injected active power that does not contribute to frequency regulation.

In general, a device that regulates the frequency imposes the total variation of power at its point of connection. In terms of the theoretical derivations of Chapter 2, this implies imposing dp_h in (A.5). Recall from Chapter 2 that dp_h can be expressed as a sum of two components, as $dp_h = dp_h' + dp_h''$. The term dp_h' is the component of the active power that can effectively modify or impact the frequency in the grid. This observation is the key of the control proposed in this section. To better illustrate this point, one can consider dp_h', dq_h' in (A.7) with respect to time and substitute $\frac{d\theta_k}{dt} = \omega_o\,\omega_k$, where ω_k is the frequency at bus k and ω_o is the reference synchronous speed in rad/s. On the other hand, the term dp_h'' mainly depends on the variations of the bus voltage magnitudes and, thus, has a negligible impact on the frequency response of the system.

The proposed control has the objective to reduce – ideally, nullify – the term dp_h''. Since this term does not contribute to the frequency response of the system, the effect is to make $dp_h \approx dp_h'$ and, hence, optimize the effectiveness of the frequency control. The control considered, in turn, is designed to impose the following constraint:

$$dp_h'' = 0\,. \tag{3.2}$$

Using (A.2), and assuming for simplicity a lossless transmission system, i.e. $G_{hk} = 0$, and defining $\tilde{B}_{hk} = B_{hk}\,\sin\theta_{hk}$, we can express dp_h'' as follows [22]:

$$dp_h'' = \textstyle\sum_{k=1}^{n} \tilde{B}_{hk}(t)\,\big(v_k\,dv_h + v_h\,dv_k\big)\,. \tag{3.3}$$

From (3.3), a sufficient condition so that (3.2) is satisfied reads as follows:

$$\textstyle\sum_{k=1}^{n}\big(v_k(t)\,dv_h + v_h(t)\,dv_k\big) = 0\,. \tag{3.4}$$

The last equation is equivalent to $v_h(t)\sum_{k=1}^{n} v_k(t) = c_o$, where c_o is a constant, which, following from the system initialization, is $c_o = v_{h,o}(t)\sum_{k=1}^{n} v_{k,o}(t)$. Finally, the modified voltage control reference that is used to achieve the control objective (3.2) is:

$$v^{\rm ref}(t) = \frac{c_o}{\sum_{k=1}^{n} v_k(t)}\,. \tag{3.5}$$

(3.5) is valid also for lossy transmission systems, i.e. $G_{hk} \neq 0$, and is, thus, a general condition. Implementation of (3.5) requires measuring the voltage magnitudes at the buses to which the DER is connected which in turn depends on the topology of the system. Figure 2a shows a DER connected to the grid in antenna. In this case, only one remote measurement is needed, namely v_2. If the DER is connected to the grid through multiple buses, more measurements are required. For example, in the topology shown in Figure 2b, one has to measure v_2 and v_3.

3.2.2 Simulation Results

The effectiveness of the proposed voltage control reference in improving the frequency response of DERs is tested by considering Use Case FC_A.1 defined in deliverable D2.1. The modifications with respect to the original Western Systems Coordinating Council (WSCC) system are as follows. SMs at buses 2 and 3 have been replaced by DERs. Then, the mechanical starting time of the SM connected to bus 1 is decreased to 23 s. With the above changes, the inertia of the system has been reduced by 65 % compared to the data of the original system. Finally, in Section A.4.2.1.2 an ESS is connected to bus 5.

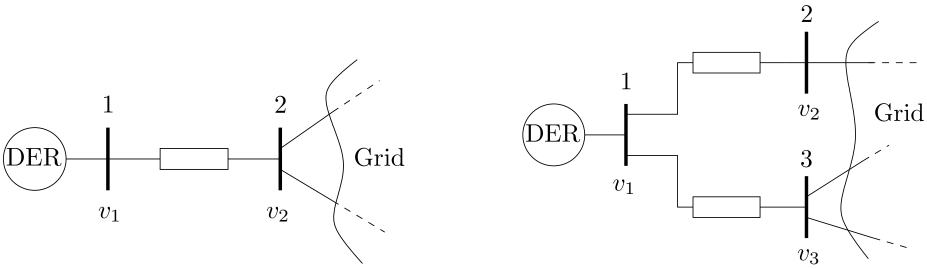

(a) Antenna **(b) Multiple Connections**

Figure 2 – Examples of DER connectivity to the grid

The DER and ESS frequency control models employed in this section are described in Section A.2.1 of D2.1 [23], while voltage control models are described in Section A.2.1 of this document. We consider the following control modes:

1. CPC (Constant Power Control), i.e. without the frequency and voltage control loops;
2. FC, i.e. with the frequency control connected and the voltage control disconnected;
3. FC+VC, i.e. with both frequency and voltage control connected and the voltage control reference given by (3.1);
4. FC+MRVC (Modified-Reference Voltage Control), i.e. with both frequency and voltage control connected and with the modified voltage control reference given by (3.5).

Simulation results are presented in Section A.4.2.1 of the ANNEX.

3.3 Coupled Voltage-Frequency Control Scheme

This section presents a control scheme for DERs, in which both active and reactive power are varied to regulate both frequency and voltage. This is in contrast to current practice, where frequency and voltage controllers are decoupled.

3.3.1 Control Structure

The block diagram of the proposed control is depicted in Figure 3. The control scheme consists of an inner current control loop and two outer loops for frequency and voltage regulation, respectively. The current control loop regulates the d and q axis components of the current ($\imath_{\mathrm{d}}$, $\imath_{\mathrm{q}}$) in the dq reference frame. These components are limited between their minimum and maximum values through an anti-windup limiter. The frequency control loop receives the frequency error ϵ_ω and applies a droop control and a washout filter in parallel. On the other hand, the voltage control loop adjusts the bus voltage error ϵ_v by means of a Proportional-Integral (PI) controller and a washout filter also in parallel. The outputs of the frequency and voltage controls are then added to the DER's active and reactive power references. Observe that we have adopted simple conventional controllers, as these are the most commonly implemented in practice. The main objective is to show how combining the effect of different control channels impact on the performance of the overall power system.

The examined DER control scheme includes four channels that can be combined to formulate different active and reactive power control modes. A summary of the available control modes for the active power of the DER is as follows:

- FP: The active power is employed to regulate the frequency. The FP mode is the standard way to regulate the frequency in conventional power systems.
- VP: The active power is employed to regulate the voltage. In this mode, a voltage control channel acts by modifying the DER active power reference.

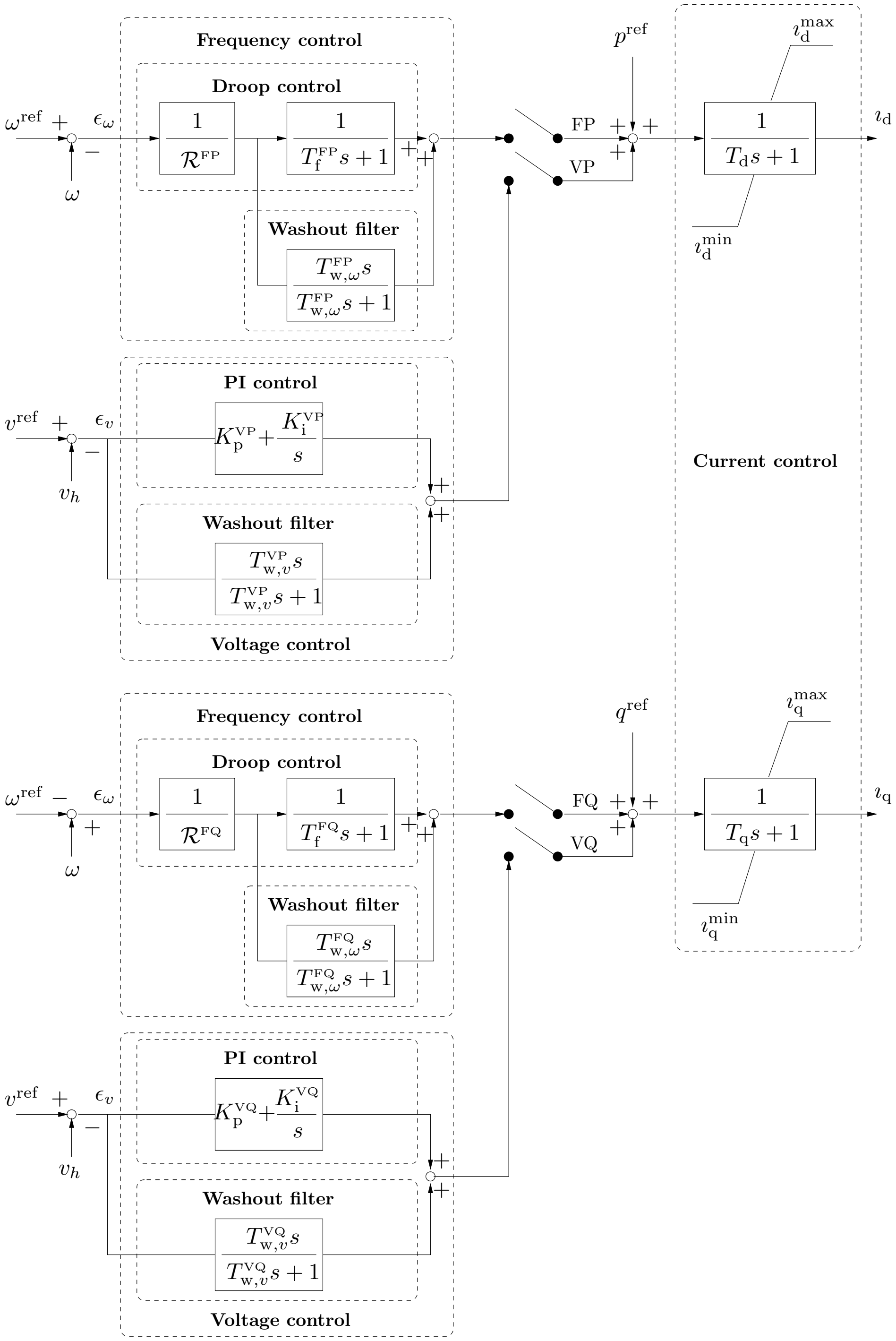

Figure 3 – DER control scheme

- FVP: The active power reference is modified to control both the frequency and the voltage. In this case, both FP and VP in Figure 3 are switched on.

Similarly, a summary of the available modes for the control of the DER reactive power is as follows:

- VQ: The reactive power is utilized to regulate the voltage. This is the classic approach, i.e. voltage regulation is conventionally realized by means of the VQ mode.
- FQ: The reactive power reference of the DER is modified to provide frequency regulation.

- FVQ: Both VQ and FQ are switched on in a combined control of the reactive power.

In this deliverable we study the effectiveness of frequency and voltage regulation provision through both the active and reactive power of DERs, which leads to the combined scheme FVP+FVQ. In Section A.4.2.2 of the ANNEX, the dynamic performance of this configuration is compared to other configurations, including the conventional approach to frequency-voltage control, i.e. FP+VQ.

3.3.2 Assessment Metric

The examined control configurations are assessed using standard criteria, such as the deviation of frequency and voltages from their nominal values. As a complementary assessment tool, this section presents a scalar metric that is employed to capture the combined effect of frequency/voltage response provided at a bus of the power network. Consider equations (A.5), (A.6). The parts of dp'_h, dq''_h and dp''_h, dq'_h that are due to local variations of the frequency and the voltage at bus h, respectively, are given by the following expressions [24]:

$$dp'^{\rm loc}_h = -q_h d\theta_h \,, \quad dq''^{\rm loc}_h = p_h d\theta_h \,, \quad dp''^{\rm loc}_h = \frac{p_h}{v_h} dv_h \,, \quad dq'^{\rm loc}_h = \frac{q_h}{v_h} dv_h \,. \tag{3.6}$$

Then rewriting equations (3.6) using time derivatives, one has:

$$\frac{dp'^{\rm loc}_h}{dt} = -q_h \theta'_h \,, \quad \frac{dq''^{\rm loc}_h}{dt} = p_h \theta'_h \,, \quad \frac{dp''^{\rm loc}_h}{dt} = p_h \varrho_h \,, \quad \frac{dq'^{\rm loc}_h}{dt} = q_h \varrho_h \,, \tag{3.7}$$

where

$$\theta'_h = \frac{d\theta_h}{dt} \,, \qquad \varrho_h = \frac{1}{v_h}\frac{dv_h}{dt} \,. \tag{3.8}$$

Note that θ'_h, ϱ_h, are, in fact, the components of the CF described in Chapter 2. θ'_h is the deviation of the bus frequency with respect to the synchronous frequency; whereas ϱ_h represents the transient rate of change of the voltage normalized with respect to the bus voltage magnitude. The latter quantity has the unit of a frequency and is thus comparable with the frequency deviation θ'_h. Since we are interested in assessing the combined active/reactive injection effect on voltage and frequency, we utilize as a metric of the joint frequency/voltage response at bus h the following quantity:

$$\mu_h = \int_{t_0}^{t} \sqrt{(\theta'_h)^2 + (\varrho_h)^2} \,. \tag{3.9}$$

This metric is obtained since we are interested in assessing the cumulative effect of $\sqrt{(\theta'_h)^2 + (\varrho_h)^2}$ for a given time interval $[t_0, t]$. This interval is determined based on the time scale of the primary response of generators, which lasts from few seconds to few tens of seconds. The metric in (3.9) has the property that the two components corresponding to the frequency and voltage are considered with the same weights and have the same units, thus being summable and directly comparable. The metric is used to compare the effectiveness of different DER active/reactive control configurations. In this regard, note that smaller values of μ_h are obtained for smaller frequency/voltage variations, which in turn, indicate a better dynamic response at bus h.

3.3.3 Simulation Results

The proposed control scheme is tested for DERs and VPPs, by considering Use Case FC_A.2 and Use Case FC_B.2 (see Section A.1 of the ANNEX). The modified New England system includes a 30 % penetration of non-synchronous generation. In particular, the SMs connected to buses 34, 35 and 37, are substituted by converter-based DERs. Considering the practical capacity of a single DER, the DERs connected to each bus here are not single generation sources but are modeled as a combination of several DERs. Loads are modeled using the ZIP model [25]. ZIP loads in this study consist of 20 % constant power, 10 % constant current, and 70 % constant impedance consumption. Finally, SMs are assumed to participate to Secondary Frequency Control (SFC) through an Automatic Generation Control (AGC) scheme. The AGC is modeled as an integrator whose output is used to update the active power set-points of the SMs every 5 s. The modified New England system is shown in Figure 4. DERs and their controls are modeled as described in Section 3.3.1.

Simulation results are presented in Section A.4.2 of the ANNEX. These results evaluate the proposed control in comparison to the classic frequency-active power, voltage-reactive power scheme, and assess the effects on its performance of the behavior of the loads; of the resistance/inductance ratio of the network lines; of the level of DER penetration to the grid; and of the system's granularity. In particular for the scope of showing the effect of the system's granularity, Section A.4.2.2.7 considers a more detailed modeling of the DN and loads, as shown in Figure 5.

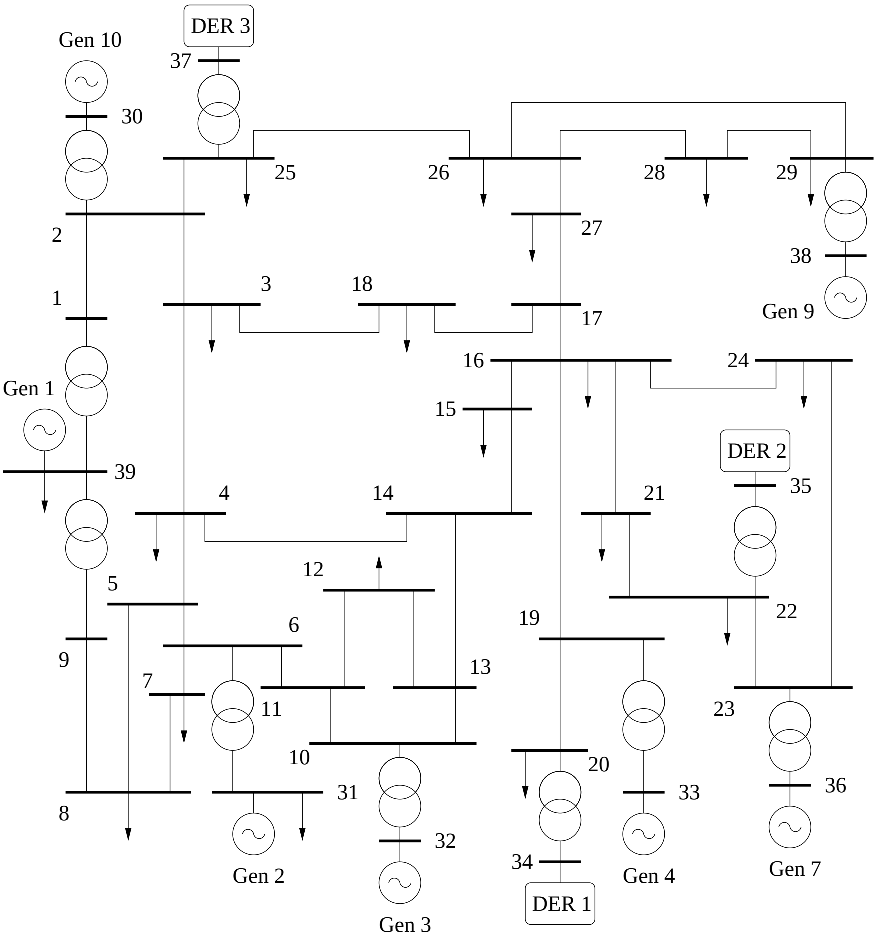

Figure 4 – Modified New England system with DERs

3.4 Estimation of Voltage Sensitivity of Loads

3.4.1 Formulation

This section proposes a technique to estimate the parameters of VDLs using non-confidential measurements. This technique is an application of the CF concept described in Chapter 2. We start with the power consumption of a VDL, which is defined as:

$$\bar{s}_h = p_h + \jmath q_h = -p_{\mathrm{L},o} v_h^{\gamma_p} - \jmath\, q_{\mathrm{L},o} v_h^{\gamma_q} \, . \tag{3.10}$$

Then:

$$\dot{\bar{s}}_h = -p_{\mathrm{L},o}\, \gamma_p\, \dot{v}_h\, v_h^{\gamma_p-1} - \jmath\, q_{\mathrm{L},o}\, \gamma_q\, \dot{v}_h\, v_h^{\gamma_q-1} = (\gamma_p\, p_h + \jmath\, \gamma_q\, q_h)\, \varrho_h \, , \tag{3.11}$$

where it is assumed that the exponents γ_p and γ_q are constant and that $p_{\mathrm{L},o}$ and $q_{\mathrm{L},o}$ vary "slowly" with respect to v_h. From (2.8) and (3.11), one obtains $(\gamma_p\, p_h + \jmath\, \gamma_q\, q_h)\, \varrho_h = \sum_{k=1}^{n} [\bar{s}_{hk}(\bar{\eta}_h + \bar{\eta}_k^*)]$,

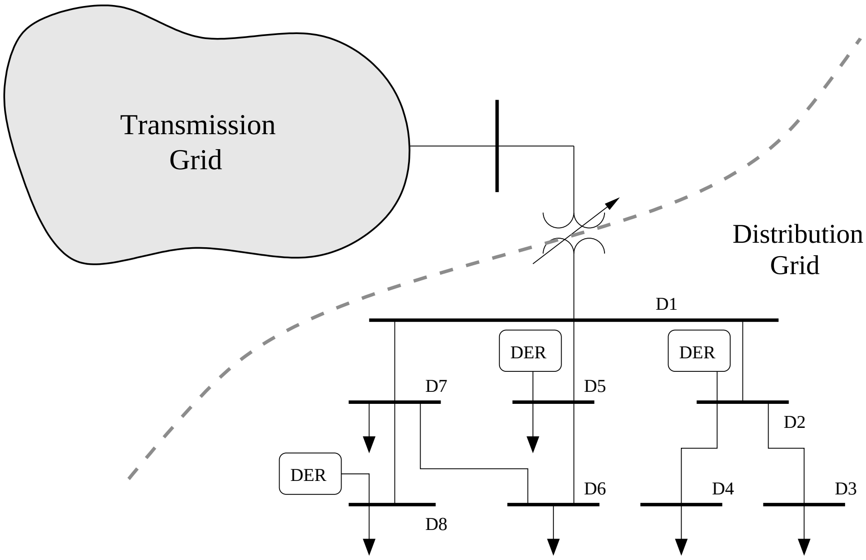

Figure 5 – Topology of DN model used in Section A.4.2.2.7

and, splitting real and imaginary parts:

$$\gamma_p = (p_h\, \varrho_h)^{-1}\, \Re\{\textstyle\sum_{k=1}^{n} \bar{s}_{hk}(\bar{\eta}_h + \bar{\eta}_k^*)\} \ , \quad \gamma_q = (q_h\, \varrho_h)^{-1}\, \Im\{\textstyle\sum_{k=1}^{n} \bar{s}_{hk}(\bar{\eta}_h + \bar{\eta}_k^*)\} \ , \tag{3.12}$$

where the right-hand sides can be determined based on measurements. The fact that $\varrho_h \to 0$ in steady-state can create numerical issues, which can be solved using finite differences over a period of time Δt, namely $\bar{\eta}_h \approx \Delta\bar{\zeta}_h/\Delta t$, $\bar{\eta}_k^* \approx \Delta\bar{\zeta}_k^*/\Delta t$, and $\varrho_h \approx \Delta u_h/\Delta t$, as follows:

$$\begin{aligned} \hat{\gamma}_p &\approx (p_h\, \Delta u_h)^{-1}\, \Re\{\textstyle\sum_{k=1}^{n} \bar{s}_{hk}(\Delta\bar{\zeta}_h + \Delta\bar{\zeta}_k^*)\} \ , \\ \hat{\gamma}_q &\approx (q_h\, \Delta u_h)^{-1}\, \Im\{\textstyle\sum_{k=1}^{n} \bar{s}_{hk}(\Delta\bar{\zeta}_h + \Delta\bar{\zeta}_k^*)\} \ . \end{aligned} \tag{3.13}$$

Using the approximation $\bar{s}_{hk} \approx -jB_{hk}$ in (3.13), the following approximate yet accurate empirical formula can be obtained for the estimation of the load active power voltage exponent, see [13, 26]:

$$\breve{\gamma}_p(t) \approx (2-\rho)\, \frac{\Delta p_h(t)}{\Delta p_h(t) + \Delta p_h'(t)} \, , \tag{3.14}$$

where $\breve{}$ indicates that estimated quantities and the time derivatives can, in practice, be approximated with finite differences [26]; the factor κ is a function of the ratio of the branches that connect the VDL to the rest of the grid, i.e. $\kappa = \kappa(R_{hk}/X_{hk})$. Moreover, the coefficient γ_q of the reactive power of the VDL can be deduced from (3.14), as follows:

$$\breve{\gamma}_q(t) \ln\left(\epsilon - \frac{p_h(t)}{p_{\mathrm{L},o}}\right) - (\breve{\gamma}_p(t) - \lambda) \ln\left(\epsilon - \frac{q_h(t)}{q_{\mathrm{L},o}}\right) = 0 \, , \tag{3.15}$$

where $\epsilon, \lambda \ll 1$, are positive coefficients to prevent initialization issues when $p_h/p_{\mathrm{L},o} \approx 1$ and/or $q_h/q_{\mathrm{L},o} \approx 1$, as well as the trivial solution $\breve{\gamma}_p = \breve{\gamma}_q = 0$ Note that, due to the approximations adopted to obtain (3.14), (3.15), expressions (3.13) are in general more accurate in estimating the VDL parameters. On the other hand, note that (3.14), (3.15) are relatively simpler to use in practice, since they can be readily implemented exclusively through standard power and frequency measurements.

3.4.2 Simulation Results

The VDL estimation techniques described in the previous section are tested using Use Case FC_E.1 and Use Case FC_E.2 defined in deliverable D2.1 and updated in see Section A.1 of this deliverable. Simulation results are presented in Section A.4.2.3 of the ANNEX.

4. Aggregated Virtual Power Plant Model

4.1 Introduction

The vast majority of existing aggregated VPP models are aimed to solve the economic dispatch and energy management problems and are thus steady-state models [27, 28]. On the contrary, this chapter proposes an aggregated VPP model for power system transient stability analysis.

To date, the transient analysis of systems with high penetration of renewables is based on models of individual DGs. Based on the structure of their controls, i.e. current source or voltage source control, the converters of these DGs are classified as GFL or GFM [29]. Recent research has focused on developing both detailed [30, 31] and simplified [32, 33] models of GFL-DGs and GFM-DGs. However, modeling VPPs using such models may lead to a considerable computational burden, especially if the number of the VPP resources is large and/or there is a large number of VPPs in the grid. From the viewpoint of Transmission System Operators (TSOs), in fact, it is not viable to model the transient behavior of each small unit of a VPP. In contrast, what is of primary interest is the transient response of the VPP as a whole.

Aggregating the capacities of several small units is common practice. In fact, TSOs often rely on aggregated grid models for dynamic security assessment. Examples of aggregated models of SMs, Wind Power Plants (WPPs), ESSs, can be found in [34, 35, 36]. Regarding VPPs, developing an aggregated model with good accuracy is a challenging task to complete. For example, most available models of DGs assume that DGs apply a GFL mode, whereas VPPs mix GFL and GFM units with various frequency and voltage controls, and thus their response is more involved. Moreover, in order to model a VPP accurately, system identification is also required to determine the parameters of the aggregated model, e.g. see [37, 38].

This chapter proposes an aggregated dynamic model able to accurately reproduce the transient response of a VPP. Since the units in a VPP can be either GFL or GFM, the proposed VPP model consists of a voltage source and a current source in parallel to emulate synchronization transients separately.

4.2 Background

This section provides a brief overview of the Grid-Following (GFL) and Grid-Forming (GFM) DG control strategies.

4.2.1 Grid-Following DG

The GFL-DG behaves like a current source. Its grid synchronization is based on a Phase-Locked Loop (PLL), which tracks the voltage phase angle at the Point of Common Coupling (PCC). Assuming that the phase angle of the PCC voltage is the reference, the phase of the VPP at the Point of Connection (POC) is $-\delta$. Then the PCC voltage components in the synchronous dq-frame can be written as follows:

$$\upsilon_{\rm d} = \upsilon_{\rm poc}\,\cos(-\delta) - (\omega_g + \Delta\omega)\,l_g\,\imath_{\rm q}\,, \quad \upsilon_{\rm q} = \upsilon_{\rm poc}\,\sin(-\delta) + (\omega_g + \Delta\omega)\,l_g\,\imath_{\rm d}\,, \tag{4.1}$$

where ω_g is the grid frequency, $\Delta\omega = \omega - \omega_g$, l_g is the inductance from the DG to the POC. The GFL-DG synchronization time constant is typically in the range [50, 100] ms. When the converter is perfectly synchronized with the grid, $\upsilon_{\rm q} = 0$ and $\upsilon_{\rm d} = \upsilon_{\rm poc}$. Moreover, the active and reactive power are decoupled. The converter control reference currents are:

$$\imath_{\rm d}^{\rm ref} = \frac{p^{\rm ref}}{\upsilon_{\rm d}}\,, \quad \imath_{\rm q}^{\rm ref} = -\frac{q^{\rm ref}}{\upsilon_{\rm d}}\,, \tag{4.2}$$

where the reference active and reactive powers are given by:

$$p^{\mathrm{ref}} = p_o^{\mathrm{ref}} + K_{\mathrm{d}}(\omega^{\mathrm{ref}} - \omega) - M\,\dot{\omega}\,, \quad q^{\mathrm{ref}} = q_o^{\mathrm{ref}} + K_{\mathrm{q}}(v^{\mathrm{ref}} - v_{\mathrm{d}})\,, \tag{4.3}$$

where ω^{ref} and v^{ref} are the reference frequency and voltage, respectively. The active power reference p^{ref} contains the feed-forward power p_o^{ref} from the DC source of the DG and the power for the fast frequency response and the PFC, where the frequency signal ω is obtained from the PLL; and the reactive power reference q^{ref} contains the reactive power set point q_o^{ref} and the compensated reactive power for the voltage support. The power delivered by the GFL-DG to the POC is:

$$p = \imath_{\mathrm{d}}\, v_{\mathrm{poc}} \cos(-\delta) \,+\, \imath_{\mathrm{q}}\, v_{\mathrm{poc}} \sin(-\delta)\,, \quad q = -\imath_{\mathrm{q}}\, v_{\mathrm{poc}} \cos(-\delta) \,+\, \imath_{\mathrm{d}}\, v_{\mathrm{poc}} \sin(-\delta)\,. \tag{4.4}$$

Note that converter current control dynamics can be neglected as their time scale is in the order of 1 ms i.e. much faster than the synchronization dynamics. Thus, we assume $\imath_{\mathrm{d}} = \imath_{\mathrm{d}}^{\mathrm{ref}}$, $\imath_{\mathrm{q}} = \imath_{\mathrm{q}}^{\mathrm{ref}}$.

4.2.2 Grid-Forming DG

The GFM-DG aims to substitute SMs in imposing the voltage and frequency to the grid. Its grid synchronization is based on the same principle as the SM, i.e. based on the power balance. A particular synchronization method for GFM-DGs is the Virtual Synchronous Generator (VSG), which consists in emulating the inertia through a swing equation. Again assuming that the PCC is the reference, the phase of the VPP at the POC is $-\delta$. Then the synchronization of the VSG is:

$$M\dot{\omega} = p - p_o^{\mathrm{ref}} + K_{\mathrm{d}}(\omega^{\mathrm{ref}} - \omega_g) + D(\omega - \omega_g)\,, \tag{4.5}$$

where D is the damping coefficient. The voltage support in the GFM-DG is an Automatic Voltage Regulator (AVR) with gain K_v:

$$v = v^{\mathrm{ref}} + K_v(v^{\mathrm{ref}} - v_{\mathrm{poc}})\,. \tag{4.6}$$

Since the GFM-DG controls the voltage directly, its reactive power couples with the active power and the power at the POC as a consequence of the voltage difference between the PCC and POC. Assuming the that system impedance is purely reactive, the power at the POC is:

$$p = \frac{v\,v_{\mathrm{poc}}}{\omega\, l_g}\,\sin\delta\,, \quad q = \frac{v\,v_{\mathrm{poc}}}{\omega\, l_g}\,\cos\delta - \frac{v_{\mathrm{poc}}^2}{\omega\, l_g}\,. \tag{4.7}$$

The converter voltage control dynamics are of the order of 10 ms and are thus neglected. For the same reason, the dynamics of the current control are also not considered, as in the GFL-DG model.

4.3 Aggregated VPP Model

GFL-DG and GFM-DG have different dynamic responses (see Section 4.2). To properly capture their transients, the proposed aggregated VPP model includes one current and one voltage source. Then, the loads in the VPP are represented with three aggregated loads according to their locations, i.e. based on whether they are located close to GFL-DG, close to GFM-DG, or close to the VPP POC to the grid. In steady-state, since GFL-DGs control the active and reactive power directly, the aggregated current source is modeled as PQ bus with negative power; whereas, since GFM-DGs control the active power and voltage directly, the aggregated voltage source model is modeled as a PV bus. The remainder of this section describes the components of the proposed aggregated VPP model.

4.3.1 Aggregated Current Source Model

Let the VPP include n GFL-DGs. Taking the POC as the observation point, these GFL-DGs can be represented by a Norton equivalent circuit where, the n current sources are connected in parallel.

The resulting aggregated model is [39]:

$$\imath_{\mathrm{d,a}} = \frac{\sum_{i=1}^{n} p_{o,i}^{\mathrm{ref}} + \sum_{i=1}^{n} \Delta p_i}{v_{\mathrm{d}}} , \quad \imath_{\mathrm{q,a}} = -\frac{\sum_{i=1}^{n} q_{o,i}^{\mathrm{ref}} + \sum_{i=1}^{n} \Delta q_i}{v_{\mathrm{d}}} , \quad \frac{1}{l_{g,\mathrm{a}}} = \sum_{i=1}^{n} \frac{1}{l_{g,i}} , \tag{4.8}$$

where Δp_i (Δq_i) is the active (reactive) power compensation of the i-th GFL-DG for frequency (voltage) support, i.e.:

$$\sum_{i=1}^{n} \Delta p_i = \sum_{i=1}^{n} K_{\mathrm{d},i}(\omega^{\mathrm{ref}} - \omega_i) - \sum_{i=1}^{n} M_i \dot{\omega}_i , \quad \sum_{i=1}^{n} \Delta q_i = \sum_{i=1}^{n} K_{\mathrm{q},i}(v^{\mathrm{ref}} - v_{\mathrm{poc}}) , \tag{4.9}$$

where the same set points ω^{ref} and v^{ref} are assumed for all GFL-DGs. In turn, the *f-P* gain, rate of change of frequency gain and *V-Q* gain of the aggregated current source model are obtained by summing the respective values of all the GFL-DGs in the VPP.

The synchronism difference of the GFL-DGs mainly depends on the term $l_g \imath_{\mathrm{d}}$. The larger $l_g \imath_{\mathrm{d}}$ is, the longer the synchronizing dynamics. In fact, the feed-forward loop of the GFL-DG synchronizing dynamics depends on $l_g \imath_{\mathrm{d}}(K_p + \frac{K_i}{s})$. Then, the aggregated PLL parameters can be computed as the weighted sum of the PI parameters of all GFL-DGs in the VPP:

$$K_{p,\mathrm{a}} + \frac{K_{i,\mathrm{a}}}{s} = \frac{\sum_{i=1}^{n} l_{g,i}\, \imath_{\mathrm{d},i}\, (K_{p,i} + \frac{K_{i,i}}{s})}{\sum_{i=1}^{n} l_{g,i}\, \imath_{\mathrm{d},i}} \approx \frac{\sum_{i=1}^{n} l_{g,i}\, p_{o,i}^{\mathrm{ref}}\, (K_{p,i} + \frac{K_{i,i}}{s})}{\sum_{i=1}^{n} l_{g,i}\, p_{o,i}^{\mathrm{ref}}} . \tag{4.10}$$

4.3.2 Aggregated Voltage Source Model

Let the VPP include m GFM-DGs. Taking the POC as the observation point, the GFM-DGs can be represented by a Thevenin equivalent circuit where the m voltage sources are connected in parallel. The resulting aggregated model is a voltage source connected to the POC through a line. The power of the aggregated voltage source is the sum of the powers of all GFM-DGs:

$$p_{\mathrm{a}} = \sum_{i=1}^{m} p_i \approx v_i v_{\mathrm{poc}} \sin\delta_i \sum_{i=1}^{m} \frac{1}{\omega_o l_{g,i}} , \quad q_{\mathrm{a}} = \sum_{i=1}^{m} q_i \approx v_i v_{\mathrm{poc}} \cos\delta_i \sum_{i=1}^{m} \frac{1}{\omega_o l_{g,i}} - v_{\mathrm{poc}}^2 \sum_{i=1}^{m} \frac{1}{\omega_o l_{g,i}} , \tag{4.11}$$

where for simplicity we use the approximation $\omega_i \approx \omega_o$. From (4.11), the line susceptance of the aggregated voltage source is the sum of all GFM-DG susceptances. Then, substituting (4.6) into (4.7) and (4.11), the reactive power due to the voltage change ($\Delta v = v^{\mathrm{ref}} - v_{\mathrm{poc}}$) at the POC is:

$$\Delta q_{\mathrm{a}} = \Delta v \sum_{i=1}^{m} \frac{K_{v,i} \cos\delta_i}{\omega_o\, l_{g,i}} , \tag{4.12}$$

where, again, we assume $\omega_i \approx \omega_o$, $\forall i = 1, \ldots, m$. Finally, the aggregated AVR gain $K_{v,\mathrm{a}}$ is computed as the weighted sum of the AVR gains $K_{v,i}$ of all GFM-DGs:

$$K_{v,\mathrm{a}} = \frac{\sum_{i=1}^{m} (K_{v,i} \cos\delta_i / \omega_o l_{g,i})}{\sum_{i=1}^{m} \cos\delta_i / \omega_o\, l_{g,i}} \approx \frac{\sum_{i=1}^{m} K_{v,i}\, q_i}{\sum_{i=1}^{m} q_i} . \tag{4.13}$$

The dynamics of the frequency response and synchronization are in a loop whose dynamic behavior is determined by the inertia, damping and droop coefficients. The inertia M_{a} and droop $K_{\mathrm{d,a}}$ of the aggregated voltage source model is the sum of inertias and droops of all GFM-DGs:

$$M_{\mathrm{a}} = \sum_{i=1}^{m} M_i , \qquad K_{\mathrm{d,a}} = \sum_{i=1}^{m} K_{\mathrm{d},i} . \tag{4.14}$$

The equivalent frequency is obtained as the weighted sum of the frequencies of all GFM-DGs, similarly to the concept of the Center-Of-Inertia (COI). However, the synthetic damping cannot be simply computed as the sum of the damping coefficients of the GFM-DGs, because it is also affected by the losses within the VPP. Instead, the damping is computed through (4.5), as follows [39]:

$$D_{\mathrm{a}} = \frac{\sum_{i=1}^{m} p_i - p_o^{\mathrm{ref}} - K_{\mathrm{d}}^{\mathrm{a}} \left(\omega^{\mathrm{ref}} - \omega\right) + \dot{\omega} M_{\mathrm{a}}}{\omega - \omega_g} \,. \tag{4.15}$$

4.3.3 Aggregated Load Model

We assume the VDL model described in Secton A.2.3 of D2.1. Loads are distributed within the VPP and we assume that their voltages depend on nearby DGs. GFL-DGs control the power directly, while their terminal voltages are passively controlled as a consequence of the assigned power set point. On the other hand, GFM-DGs control the voltage directly. That said, loads are classified into three categories, depending on their location. In particular, v_i is set to the voltage (i) at the POC if the load is close to the POC; (ii) of the aggregated current source output if the load is close to the GFL-DG; (iii) of the aggregated voltage source output if the load is close to the GFM-DG. Then, the distributed loads are aggregated into three clusters, namely at the buses of the POC, current source and voltage source, respectively. Note that, in reality, v_i is not exactly equal to the aggregated bus voltage. Hence a small mismatch on loading is inevitable.

4.3.4 Model Identification

A VPP generally measures $(v_i, \imath_{\mathrm{d},i}, \imath_{\mathrm{q},i})$ or (p_i, q_i, ω_i) at the terminal of each DG, and commands the set point $p_{o,i}^{\mathrm{ref}}$, $q_{o,i}^{\mathrm{ref}}$, v^{ref}, ω^{ref} and the primary control gains $K_{\mathrm{d},i}$, $K_{\mathrm{q},i}$, $K_{v,i}$ to each DG. However, the internal dynamic parameters, inertia M_i, input inductance $l_{g,i}$ and damping D_i are not known by the VPP. In the aggregated model, the damping can be identified with (4.15) but the inertia M_i and input impedance $l_{g,i}$ still need to be identified. The power system identification is a broad and open research topic and there exist plenty of relevant methods in the literature. Inertia in this model is estimated using the method described in [40]. The system reactance from each DG to the POC is computed via a derivation of the power flow equations [7, 41]:

$$l_{g,i} = \frac{v_i v_g \sin(\delta_i)}{\Delta p_i} \approx \frac{v_i v_g \int(\omega_i - \omega_g)}{\Delta p_i} \,. \tag{4.16}$$

4.4 Simulation Results

The suitability of the proposed VPP model for system-wide applications is tested considering different contingencies and based on Use Case FC_B.2, see Section A.1.2 of the ANNEX. The New England system is modified to include 3 VPPs, i.e. 3 SMs with nearby loads are replaced by VPPs. The modified system is shown in Figure 6. For simplicity, the topology of each VPP is identical, but the capacities and parameters of the DGs, as well as the distributed loads in the VPP, are different. GFL- and GFM-DGs are represented by detailed models [42], including the dynamics of voltage and current controllers and converter filters.

Simulation results are presented in Section A.4.3.

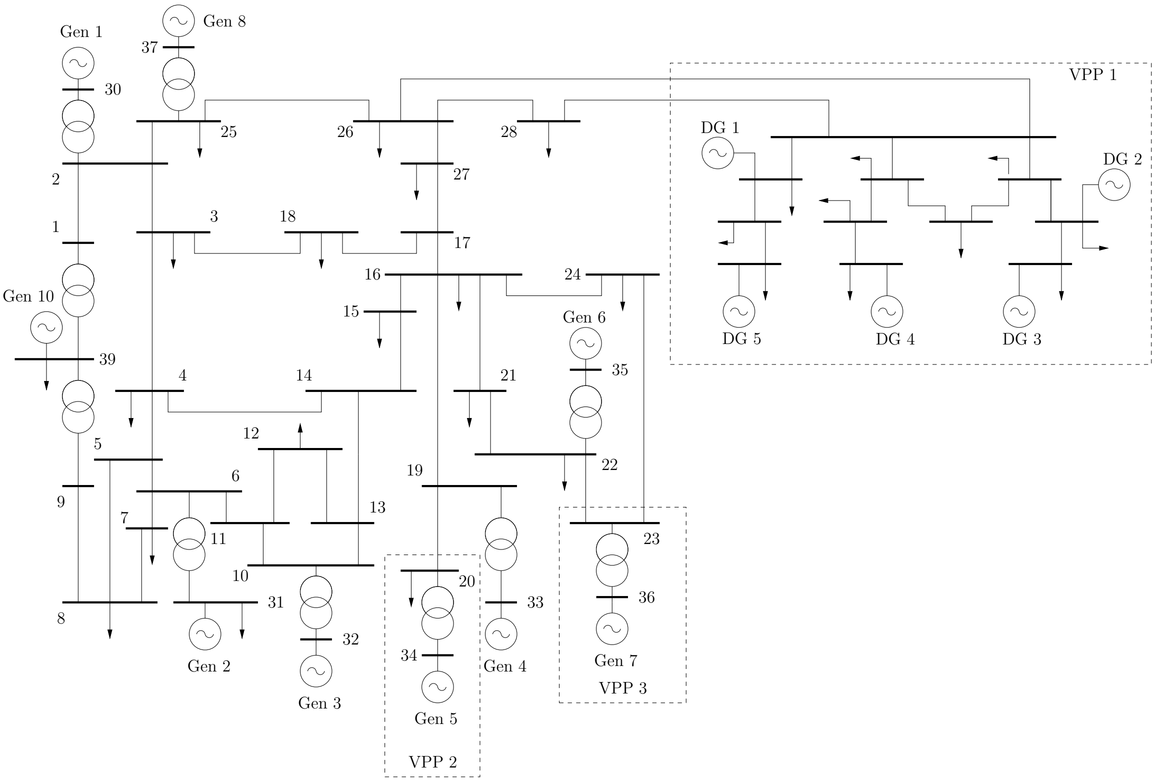

Figure 6 – Modified New England system with VPPs

5. Decentralized Charging of Plug-In Electric Vehicles

5.1 Introduction

PEVs are a valuable resource of flexibility for the power system. This section proposes an algorithm that exploits this flexibility, by providing an efficient way to control the charging of PEVs without affecting the system stability. The proposed approach is based on an Additive-Increase-Multiplicative-Decrease (AIMD) stochastic decentralized control strategy to efficiently and seamlessly manage the charging of PEVs with little communication efforts, and is particularly suited for large numbers of PEVs.

The impact of PEVs on power system dynamics is intrinsically tied to their charging strategy. Without a suitable control, in fact, the charging of large fleets of PEVs may compromise the operation and security of power systems [43]. Among existing studies that investigate the impact of large numbers of PEVs on power system dynamics, we cite [44, 45, 46]. On the other hand, if proper control schemes are applied, PEVs can help maintain or even improve the performance of the power grid [43]. Relevant literature studies solutions for provision of flexibility by PEVs both in short-term [47, 48] and long-term [49, 50] time scales.

The charging control system of PEVs can be implemented following either a decentralized or a centralized strategy [51]. Comparison between the two shows that centralized management of the charging process of a large number of PEVs may become computationally intractable and impractical, and thus, most charging algorithms are evolving towards a decentralized structure [52]. For this reason, the strategy proposed in this chapter follows a decentralized approach. In particular, the decentralized AIMD algorithm is considered; this approach has been applied for a particular class of resource-sharing problems, where a group of agents with limited or no communication abilities wish to optimally share a given resource [53]. In our case, the algorithm coordinates the charging rates of PEVs, so that the available power can be utilized by all vehicles in a fair and safe fashion. Since this approach is fully decentralized, it implies that the solution is scalable and independent from the number of agents. In our case particularly, this means that it is neither required to count the number of PEVs connected for charging, nor the amount of energy that they need. Accordingly, neither PEVs, nor charging stations, require to communicate any information, contrary to the vast majority of other existing distributed charging algorithms. In fact, AIMD algorithms have been already discussed for PEV charging in some works [54, 55, 56]. These references envisage the adoption of AIMD but they do not consider any model of the power grid. Recently, [57] proposes AIMD algorithms for PEV charging control supported by a distribution grid model, and measurements of local voltages are used to decentralize the charging operation. While this approach is similar to the one proposed in this chapter, yet no optimization problem is formulated in [57] and, thus, the whole power capacity of the network is not fully utilized during the charging process.

5.2 AIMD-Based Decentralized Control of PEVs

The problem of optimal allocation of a shared resource (here, power) among a set of competing agents (here, PEVs) arises in many different scientific and engineering applications. The AIMD algorithm, which was initially introduced to address internet congestion problems and optimally share bandwidth between connected computers, may be efficiently used to solve this problem. In particular, AIMD is known to be very attractive when the number of agents is continuously changing (here, PEVs connect and disconnect from the grid), with limited or no communication abilities. The algorithm consists of two alternating phases:

1. the Additive Increase (AI) phase: the resource consumption of each agent increases linearly in time with a certain step $\alpha > 0$;
2. the Multiplicative Decrease (MD) stage: each agent decreases its consumption in a multiplicative fashion, with a certain slope $\beta > 0$.

In particular, the MD step is performed when a Capacity Event (CE) occurs, which means that the limit of the shared resource has been reached, e.g. all the available power is fully shared by the connected PEVs. Let $t_1 < t_2 < \cdots < t_k < \ldots$ denote the time instants when CEs occur; if t_{k+1}^+ is the instant after the agent i performs an MD step at time t_k, its share of the resource $x_i(t_{k+1}^+)$ is:

$$x_i(t_{k+1}^+) = \beta \lim_{t \to t_{k+1}} x_i(t)\,, \tag{5.1}$$

and then agent i will return to the AI phase, until the next CE occurs. Therefore, the equation describing the behaviour of the i-th agent is the following:

$$x_i(t) = \beta x_i(t_k) + \alpha(t - t_k), \quad t \in (t_k, t_{k+1})\,, \tag{5.2}$$

where t_k and t_{k+1} represent two consecutive time instants at which a CE occurs.

We tailor the general AIMD algorithm for our application, as follows: each bus of the network has a maximum allowed power $p_s^{\max}$ that is shared among PEVs; let us denote with $p_{i,s}$ the power consumption of the i-th agent at the s-th bus. Then a CE occurs at the s-th bus when the sum of the charge rates $p_{i,s}$ of all connected PEVs exceeds the maximum available power $p_s^{\max}$.

5.3 Unsynchronized AIMD Control

The version of the AIMD algorithm described above is also known as the *synchronized* AIMD, as *all* PEVs reduce the charging rate in a multiplicative fashion when a CE is notified. In reality, it is sufficient that only a subset of PEVs decrease their charge rates and this possibility is useful to prioritize some PEVs over others [58]. This can be achieved by implementing an *unsynchronized* version of the AIMD, where only a subset of PEVs react to a CE, in a probabilistic way.

Priorities of single buses can be formally stated by assuming that each PEV i has its own Utility Function (UF) $f_{i,s}(p_{i,s})$, where for convenience we consider convex, strictly differentiable UFs $f_{i,s}(\cdot)$ that have a global minimum for the maximum allowed charge rate (i.e., here 3.3 kW). Roughly speaking, this implies that the minimum value of the UF of PEVs is achieved when PEVs are charged at the maximum power. Accordingly, we formulate an optimization problem for each bus as follows:

$$\begin{cases} \min\limits_{p_{i,s} \in [0,3.3]\text{kW}} \sum_{i=1}^{n(s)} f_{i,s}(p_{i,s}) \\ \sum_{i=1}^{n(s)} p_{i,s} \le p_s^{\max}\,, \end{cases} \tag{5.3}$$

where $n(s)$ is the number of PEVs connected to the s-th bus. Roughly speaking, Problem (5.3) works as follows: when there are no stability issues, then the minimization of the sum of the UFs is achieved when PEVs are charged at the maximum charging rate; when the aggregated vehicles load reaches the power limit, then PEVs are charged at a lower charging rate and safer system configurations are restored. The optimization problem (5.3) can be solved in a fully decentralized way if we let each vehicle asynchronously perform the decrease step with probability [59]:

$$\pi_{i,s}(\bar{p}_{i,s}(t)) = \Gamma \frac{f'_{i,s}(\bar{p}_{i,s}(t))}{\bar{p}_{i,s}(t)}\,, \tag{5.4}$$

where $f'(\cdot)$ is the derivative of function $f(\cdot)$ with respect to time, and $\bar{p}_{i,s}(t)$ is the average charge rate of PEV i at bus s at previous time steps (to improve smoothness of the solution):

$$\bar{p}_{i,s}(t) = \frac{1}{t} \int_0^t p_{i,s}(\tau)\, d\tau\,, \tag{5.5}$$

and Γ appearing in (5.4) is a constant required to map $\pi_{i,s}$ into a probability, i.e., $0 \le \pi_{i,s} \le 1$. Equation (5.4) means that each PEV i reacts to a CE independently from the others, with the customized probability $\pi_{i,s}(\bar{p}_{i,s}(t))$ based on its historical power consumption. Algorithm 1 provides a pseudocode to implement the AIMD algorithm at each bus. If convex UFs are considered as in our case, and parameters α and β are the same for all agents, then the convergence analysis described in [59, Section 4] can be used, and Algorithm 1 produces a long-term average that converges almost surely to the optimal solution of (5.3).

Algorithm 1 Unsynchronized AIMD algorithm at the s-th bus

```
Initialisation: $k = 1$;
  while $k < k_{simulation}$ do
    if $\sum_i p_{i,s}(k) \geq p_s^{\max}(k)$ then
      $p_{i,s}(k+1) = \begin{cases} \beta p_{i,s}(k), & \text{with probability } \pi_{i,s}(\bar{p}_{i,s}(k)) \\ p_{i,s}(k) + \alpha, & \text{with probability } 1 - \pi_{i,s}(\bar{p}_{i,s}(k)) \end{cases};$
    else
      $p_{i,s}(k+1) = p_{i,s}(k) + \alpha;$
    end if
    $k = k + 1;$
  end while
```

Unlike many other optimization approaches, the AIMD does not require to solve a new optimization problem as new PEVs connect for charging, but a new optimized solution is obtained; all the communication is restricted to a CE, i.e. a 0 or 1 bit of communication.

In a practical implementation of Algorithm 1 in a power grid, we assume that it would be too complicated, and anyway not fundamental, to change the charging rates of PEVs too often, and for this reason we assume that CEs only occur every 30 s, in accordance with [60].

5.4 Simulation Results

The proposed AIMD-based charging control strategy is tested based on Use Case FC_C.1 defined in deliverable D2.1 [23]. The New England system is modified by replacing Gens 1 and 5 with WPPs of same capacity, with detailed dynamic models of the doubly-fed induction generator, wind turbine and maximum power point tracking and voltage control of the power electronic converters [25].

Loads are connected to the grid through Under-Load Tap Changers (ULTCs) with discrete control of the voltage. Moreover, aggregated models of the PEV charging stations (see Section A.2.2) are assumed to be located at buses 3, 4, 7, 8 and 12; for simplicity, all stations have the same maximum charging rate, i.e. 3.3 kW, which is the typical nominal rate of domestic chargers [61]. SVCs have also been included at these buses to prevent collapses due to shortage of reactive power in the grid. Note that, since the focus is on PEVs, we have not included in the system a fast frequency control in WPPs nor large batteries. The load consumption of the system has been increased by 10 pu with respect to the original data, and pre-existing loads (including industrial and residential loads) at each bus of the system are considered constant, which allows one to separate the effects of the PEVs from those of conventional loads.

Simulation results are presented in Section A.4.4 of the ANNEX.

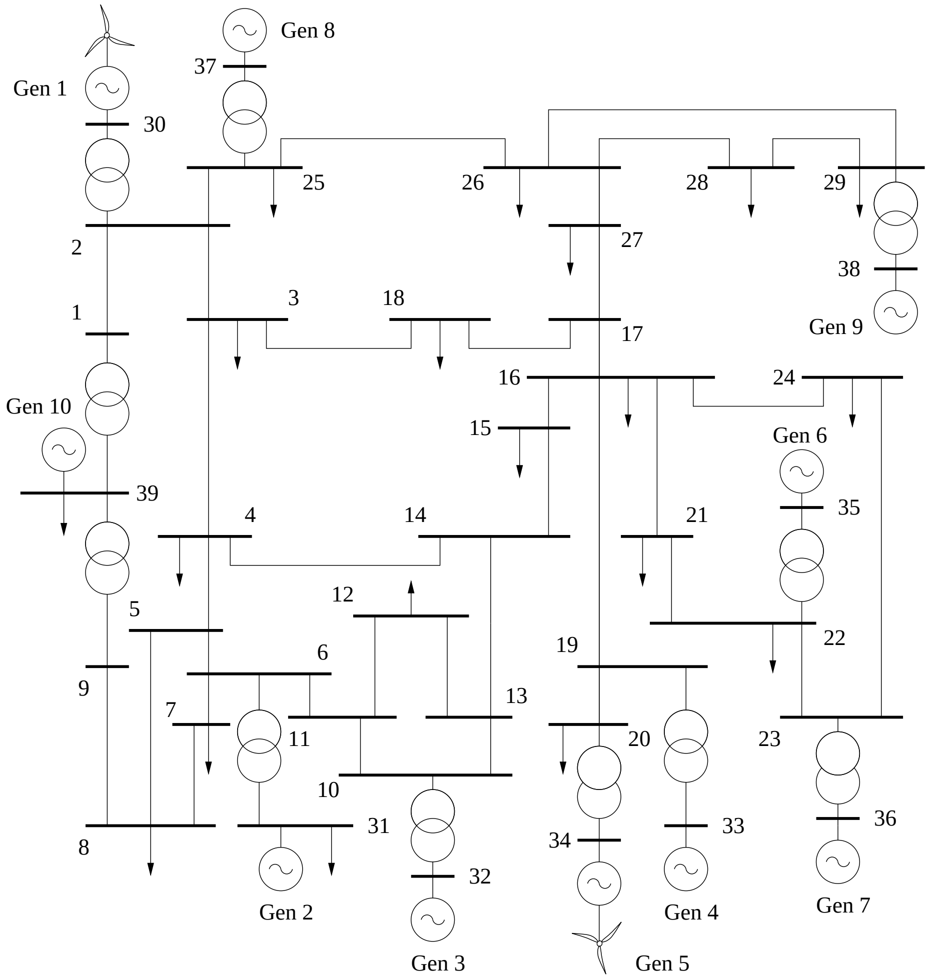

Figure 7 – Modified New England system. Gens 1 and 5 are modeled as WPPs

6. Conclusions

This deliverable presents the frequency control algorithms developed for future VPPs and ECs, including modeling and estimation of frequency and power variations with the CF concept, combined active and reactive power regulation of DERs and VPPs, frequency measurement-based estimation of VDLs, aggregated modeling of VPPs comprising GFL and GFM-based resources, and decentralized charging control of large fleets of PEVs.

Results on the concepts described in Chapter 2 show that the newly defined CF is able to better capture the power and frequency variations in a power network compared to state-of-the-art approximated expressions, including the FDF described in deliverable D2.2. Moreover, the CF is useful for evaluating how good is the estimation of the frequency obtained with a given PLL, and also appears as a valuable tool for the design of efficient control schemes and novel dynamic estimation techniques.

The deliverable presents two control schemes for DERs and VPPs. The first control scheme consists in modifying the reference of the DER voltage control loops according to a proper voltage-based feedback. Simulation results show that this control provides a significant improvement of the frequency regulation for a class of disturbances, e.g., short-circuits and line outages. The second scheme is a combined controller for converter-based DERs and VPPs, in which both active and reactive power injections are modified to compensate both for frequency and voltage variations. The controller is evaluated in terms of local voltage variations and system COI frequency dynamic response, as well as in terms of a properly defined joint voltage/frequency response metric. Several simulations are carried out and results indicate that, overall, the proposed scheme outperforms other possible active/reactive power control modes and provides a significant improvement to the dynamic response of the system. The performance of both control schemes is dependent upon the voltage sensitivity of nearby loads. Consequently, the deliverable also describes a novel dynamic estimation technique to identify in real-time the parameters of VDLs. Both exact and approximated formulas are discussed and simulation results confirm the accuracy of the proposed approach.

The deliverable also proposes an aggregated low-order model that is able to accurately capture the transient response of VPPs with respect to system contingencies. The proposed aggregated model consists of a current source to represent GFL-DG dynamics and a voltage source to represent GFM-DG dynamics in the VPP. Aggregated loads are also properly represented. Simulation results indicate that, with the proposed model, TSOs can study the dynamic response of the grid without loss of accuracy and with no need to model in detail the topology and the various units that comprise the VPP.

Finally, the deliverable proposes a decentralized AIMD algorithm for charging PEVs without affecting the system stability, by dynamically allocating the available power in an optimized way. The proposed strategy requires neither PEV nor charging stations to communicate any information, e.g. their connection for charging, and is particular suitable for large numbers of PEVs. An interesting conclusion in this study is that automatic frequency-based, or voltage-based control strategies fail to preserve the stability of the network. On the other side, power-based control strategies can be used to automatically and seamlessly adjust charging rates of PEVs to optimize a desired cost function of interest.

7. List of Tables

8. List of Figures

9. References

[1] *IEEE/IEC International Standard - Measuring relays and protection equipment - Part 118-1: Synchrophasor for power systems - Measurements*, IEC/IEEE Std., 2018.

[2] H. Kirkham, W. Dickerson, and A. Phadke, "Defining power system frequency," in *Proceedings of the IEEE PES General Meeting*, 2018, pp. 1–5.

[3] M. Paolone, T. Gaunt, X. Guillaud, M. Liserre, S. Meliopoulos, A. Monti, T. Van Cutsem, V. Vittal, and C. Vournas, "Fundamentals of power systems modelling in the presence of converter-interfaced generation," *Electric Power System Research*, vol. 189, p. 106811, 2020.

[4] J. Nutaro and V. Protopopescu, "Calculating frequency at loads in simulations of electro-mechanical transients," *IEEE Transactions on Smart Grid*, vol. 3, no. 1, pp. 233–240, March 2012.

[5] F. Milano and Á. Ortega, "Frequency divider," *IEEE Transactions on Power Systems*, vol. 32, no. 2, pp. 1493–1501, Mar. 2017.

[6] H. Golpira and A. R. Messina, "A center-of-gravity-based approach to estimate slow power and frequency variations," *IEEE Transactions on Power Systems*, vol. PP, no. 99, pp. 1–1, 2017.

[7] F. Milano and Á. Ortega, "A method for evaluating frequency regulation in an electrical grid – Part I: Theory," *IEEE Transactions on Power Systems*, vol. 36, no. 1, pp. 183–193, Jan. 2021.

[8] F. Saccomanno, *Electric Power Systems - Analysis and Control*. New York: John Wiley & Sons, 2003.

[9] F. Milano and Á. Ortega, *Frequency Variations in Power Systems: Modeling, State Estimation, and Control*. John Wiley & Sons, 2020.

[10] H. Akagi, E. H. Watanabe, and M. Aredes, *Instantaneous Power Theory and Applications to Power Conditioning*, 2nd ed. New York: Wiley IEEE Press, 2017.

[11] P. W. Sauer and M. A. Pai, *Power System Dynamics and Stability*. Upper Saddle River, NJ: Prentice Hall, 1998, vol. 101.

[12] B. Stott and O. Alsaç, "Fast decoupled load flow," *IEEE Transactions on Power Systems*, vol. PAS-93, no. 3, pp. 859–869, 1974.

[13] F. Milano, "Complex frequency," *IEEE Transactions on Power Systems*, pp. 1–1, 2021.

[14] H2020 edgeFLEX, "D2.2 frequency control concepts for current VPPs in large scale deployment," 2021, https://www.edgeflex-h2020.eu/progress/work-packages.html.

[15] P. Kundur, *Power System Stability and Control*. New York: McGraw-Hill, 1994.

[16] J. M. Guerrero, Luis Garcia de Vicuna, J. Matas, M. Castilla, and J. Miret, "Output impedance design of parallel-connected UPS inverters with wireless load-sharing control," *IEEE Transactions on Industrial Electronics*, vol. 52, no. 4, pp. 1126–1135, 2005.

[17] Y. W. Li and C. Kao, "An accurate power control strategy for power-electronics-interfaced distributed generation units operating in a low-voltage multibus microgrid," *IEEE Transactions on Power Electronics*, vol. 24, no. 12, pp. 2977–2988, 2009.

[18] G. Delille, J. Yuan, and L. Capely, "Taking advantage of load voltage sensitivity to stabilize power system frequency," in *2013 IEEE Grenoble Conference*. IEEE, 2013, pp. 1–6.

[19] M. Farrokhabadi, C. A. Cañizares, and K. Bhattacharya, "Frequency control in isolated/islanded microgrids through voltage regulation," *IEEE Transactions on Smart Grid*, vol. 8, no. 3, pp. 1185–1194, 2017.

[20] G. De Carne, G. Buticchi, M. Liserre, and C. Vournas, "Load control using sensitivity identification by means of smart transformer," *IEEE Transactions on Smart Grid*, vol. 9, no. 4, pp. 2606–2615, July 2018.

[21] M. A. A. Murad, G. Tzounas, M. Liu, and F. Milano, "Frequency control through voltage regulation of power system using SVC devices," in *Proceedings of the IEEE PES General Meeting*, 2019, pp. 1–5.

[22] G. Tzounas and F. Milano, "Improving the frequency response of DERs through voltage feedback," in *Proceedings of the IEEE PES General Meeting*, 2021, pp. 1–5.

[23] H2020 edgeFLEX, "D2.1 scenario description for frequency and inertia response control for VPPs," 2021, https://www.edgeflex-h2020.eu/progress/work-packages.html.

[24] J. Arrillaga and N. Watson, *Computer Modelling of Electrical Power Systems*. New York: John Wiley & Sons, 2001, ch. 4, pp. 81–128.

[25] F. Milano, *Power System Modelling and Scripting*. London: Springer, 2010.

[26] Á. Ortega and F. Milano, “Estimation of voltage dependent load models through power and frequency measurements,” *IEEE Transactions on Power Systems*, vol. 35, no. 4, pp. 3308–3311, 2020.

[27] E. Mashhour and S. M. Moghaddas-Tafreshi, “Bidding strategy of virtual power plant for participating in energy and spinning reserve markets—part i: Problem formulation,” *IEEE Transactions on Power Systems*, vol. 26, no. 2, pp. 949–956, 2011.

[28] G. Zhang, C. Jiang, and X. Wang, “Comprehensive review on structure and operation of virtual power plant in electrical system,” *IET Generation, Transmission Distribution*, vol. 13, no. 2, pp. 145–156, 2019.

[29] J. Rocabert, A. Luna, F. Blaabjerg, and P. Rodríguez, “Control of power converters in AC microgrids,” *IEEE Transactions on Power Electronics*, vol. 27, no. 11, pp. 4734–4749, 2012.

[30] J. Hu, L. Sun, X. Yuan, S. Wang, and Y. Chi, “Modeling of type 3 wind turbines with df/dt inertia control for system frequency response study,” *IEEE Transactions on Power Systems*, vol. 32, no. 4, pp. 2799–2809, 2017.

[31] S. D’Arco, J. A. Suul, and O. B. Fosso, “A virtual synchronous machine implementation for distributed control of power converters in smartgrids,” *Electric Power Systems Research*, vol. 122, pp. 180 – 197, 2015.

[32] D. Dong, B. Wen, D. Boroyevich, P. Mattavelli, and Y. Xue, “Analysis of phase-locked loop low-frequency stability in three-phase grid-connected power converters considering impedance interactions,” *IEEE Transactions on Industrial Electronics*, vol. 62, no. 1, pp. 310–321, 2015.

[33] J. Chen and T. O’Donnell, “Parameter constraints for virtual synchronous generator considering stability,” *IEEE Transactions on Power Systems*, vol. 34, no. 3, pp. 2479–2481, 2019.

[34] Q. Shi, F. Li, and H. Cui, “Analytical method to aggregate multi-machine SFR model with applications in power system dynamic studies,” *IEEE Transactions on Power Systems*, vol. 33, no. 6, pp. 6355–6367, 2018.

[35] H. Ye, W. Pei, and Z. Qi, “Analytical modeling of inertial and droop responses from a wind farm for short-term frequency regulation in power systems,” *IEEE Transactions on Power Systems*, vol. 31, no. 5, pp. 3414–3423, 2016.

[36] H. Huang, P. Ju, Y. Jin, X. Yuan, C. Qin, X. Pan, and X. Zang, “Generic system frequency response model for power grids with different generations,” *IEEE Access*, vol. 8, pp. 14 314–14 321, 2020.

[37] J. Zhang and H. Xu, “Online identification of power system equivalent inertia constant,” *IEEE Transactions on Industrial Electronics*, vol. 64, no. 10, pp. 8098–8107, 2017.

[38] A. Tarkiainen, R. Pollanen, M. Niemela, and J. Pyrhonen, “Identification of grid impedance for purposes of voltage feedback active filtering,” *IEEE Power Electronics Letters*, vol. 2, no. 1, pp. 6–10, 2004.

[39] J. Chen, M. Liu, and F. Milano, “Aggregated model of virtual power plants for transient frequency and voltage stability analysis,” *IEEE Transactions on Power Systems*, vol. 36, no. 5, pp. 4366–4375, 2021.

[40] M. Liu, J. Chen, and F. Milano, “On-line inertia estimation for synchronous and non-synchronous devices,” *IEEE Transactions on Power Systems*, vol. 36, no. 3, pp. 2693–2701, 2020.

[41] Á. Ortega and F. Milano, “A method for evaluating frequency regulation in an electrical grid – Part II: Applications to non-synchronous devices,” *IEEE Transactions on Power Systems*, vol. 36, no. 1, pp. 194–203, Jan. 2021.

[42] J. Chen, M. Liu, C. O’Loughlin, F. Milano, and T. O’Donnell, “Modelling, simulation and hardware-in-the-loop validation of virtual synchronous generator control in low inertia power system,” in *Proceedings of the Power Systems Computation Conference (PSCC)*, 2018, pp. 1–7.

[43] D. B. Richardson, “Electric vehicles and the electric grid: A review of modeling approaches, impacts, and renewable energy integration,” *Renewable and Sustainable Energy Reviews*, vol. 19, pp. 247–254, 2013.

[44] A. Hajimiragha, C. A. Canizares, M. W. Fowler, and A. Elkamel, “Optimal transition to plug-in hybrid electric vehicles in Ontario, Canada, considering the electricity-grid limitations,” *IEEE Transactions on Industrial Electronics*, vol. 57, no. 2, pp. 690–701, 2009.

[45] R. C. Green, L. Wang, M. Alam, and S. S. S. R. Depuru, “Evaluating the impact of plug-in hybrid electric vehicles on composite power system reliability,” in *2011 North American Power Symposium*. IEEE, 2011, pp. 1–7.

[46] M. Moschella, M. A. A. Murad, E. Crisostomi, and F. Milano, “On the impact of PEV charging on transmission system: Static and dynamic limits,” in *Proceedings of the IEEE PES General Meeting*. IEEE, 2020, pp. 1–5.

[47] S. Izadkhast, P. Garcia-Gonzalez, P. Frìas, L. Ramìrez-Elizondo, and P. Bauer, “An aggregate model of plug-in electric vehicles including distribution network characteristics for primary frequency control,” *IEEE Transactions on Power Systems*, vol. 31, no. 4, pp. 2987–2998, 2015.

[48] J. A. P. Lopes, F. J. Soares, and P. M. R. Almeida, “Integration of electric vehicles in the electric power system,” *Proceedings of the IEEE*, vol. 99, no. 1, pp. 168–183, 2010.

[49] Y. Shi, H. D. Tuan, A. V. Savkin, T. Q. Duong, and H. V. Poor, “Model predictive control for smart grids with multiple electric-vehicle charging stations,” *IEEE Transactions on Smart Grid*, vol. 10, no. 2, pp. 2127–2136, 2018.

[50] M. E. Khodayar, L. Wu, and Z. Li, “Electric vehicle mobility in transmission-constrained hourly power generation scheduling,” *IEEE Transactions on Smart Grid*, vol. 4, no. 2, pp. 779–788, 2013.

[51] J. García-Villalobos, I. Zamora, J. I. San Martín, F. J. Asensio, and V. Aperribay, “Plug-in electric vehicles in electric distribution networks: A review of smart charging approaches,” *Renewable and Sustainable Energy Reviews*, vol. 38, pp. 717–731, 2014.

[52] J. C. Mukherjee and A. Gupta, “A review of charge scheduling of electric vehicles in smart grid,” *IEEE Systems Journal*, vol. 9, no. 4, pp. 1541–1553, 2014.

[53] M. Corless, C. King, R. Shorten, and F. Wirth, *AIMD dynamics and distributed resource allocation*. SIAM, 2016.

[54] S. Stüdli, E. Crisostomi, R. Middleton, and R. Shorten, “A flexible distributed framework for realising electric and plug-in hybrid vehicle charging policies,” *International Journal of Control*, vol. 85, no. 8, pp. 1130–1145, 2012.

[55] S. Stüdli, E. Crisostomi, R. Middleton, and R. Shorten, “Optimal real-time distributed V2G and G2V management of electric vehicles,” *International Journal of Control*, vol. 87, no. 6, pp. 1153–1162, 2014.

[56] S. N. Shah, G. P. Incremona, P. Bolzern, and P. Colaneri, “Optimization based AIMD saturated algorithms for public charging of electric vehicles,” *European Journal of Control*, vol. 47, pp. 74–83, 2019.

[57] E. Ucer, M. C. Kisacikoglu, and M. Yuksel, “Analysis of decentralized AIMD-based EV charging control,” in *Proceedings of the IEEE PES General Meeting*. IEEE, 2019, pp. 1–5.

[58] E. Crisostomi, R. Shorten, S. Stüdli, and F. Wirth, *Electric and plug-in hybrid vehicle networks: optimization and control*. CRC Press, 2017.

[59] F. R. Wirth, S. Stuedli, J. Y. Yu, M. Corless, and R. Shorten, “Nonhomogeneous place-dependent Markov chains, unsynchronised AIMD, and optimisation,” *Journal of the ACM (JACM)*, vol. 66, no. 4, pp. 1–37, 2019.

[60] P. Ferraro, E. Crisostomi, M. Raugi, and F. Milano, “Decentralized stochastic control of microgrids to improve system frequency stability,” in *2017 IEEE PES Innovative Smart Grid Technologies Conference Europe (ISGT-Europe)*. IEEE, 2017, pp. 1–6.

[61] European Environment Agency, “Electric vehicles in Europe,” 2016, eEA Report No 20/2016.

[62] P. Haugneland, C. Bu, and E. Hauge, “The Norwegian EV success continues,” in *EVS29 Symposium, Montreal, Quebec, Canada*, 2016, p. 9.

[63] S. Hardman, A. Jenn, G. Tal, J. Axsen, G. Beard, N. Daina, E. Figenbaum, N. Jakobsson, P. Jochem, N. Kinnear, *et al.*, “A review of consumer preferences of and interactions with electric vehicle charging infrastructure,” *Transportation Research Part D: Transport and Environment*, vol. 62, pp. 508–523, 2018.

[64] J. Quirós-Tortós, L. F. Ochoa, and B. Lees, “A statistical analysis of EV charging behavior in the UK,” in *2015 IEEE PES Innovative Smart Grid Technologies Latin America (ISGT LATAM)*. IEEE, 2015, pp. 445–449.

[65] F. Milano and R. Zárate Miñano, “A systematic method to model power systems as stochastic differential algebraic equations,” *IEEE Transactions on Power Systems*, vol. 28, no. 4, pp. 4537–4544, Nov. 2013.

[66] H. Stephani, *Differential Equations: Their Solution Using Symmetries*, M. MacCallum, Ed. Cambridge University Press, 1990.

[67] F. Milano, “A Python-based software tool for power system analysis,” in *Proceedings of the IEEE PES General Meeting*, Vancouver, BC, July 2013.

[68] Á. Ortega and F. Milano, “Comparison of different PLL implementations for frequency estimation and control,” in *Proceedings of the 18th International Conference on Harmonics and Quality of Power (ICHQP)*, May 2018, pp. 1–6.

[69] W. Zhong, G. Tzounas, and F. Milano, “Improving the power system dynamic response through a combined voltage-frequency control of distributed energy resources,” *IEEE Transactions on Power Systems*, 2021, under review. Available online at: http://faraday1.ucd.ie.

[70] C. Murphy and A. Keane, “Local and remote estimations using fitted polynomials in distribution systems,” *IEEE Transactions on Power Systems*, vol. 32, no. 4, pp. 3185–3194, 2016.

[71] K. Jimma, A. Tomac, K. Vu, and C. Liu, “A study of dynamic load models for voltage collapse analysis,” in *Proc. Bulk Power System Voltage Phenomena, Voltage Stability and Security NFS Workshop*, Deep Creek Lake, Maryland, August 1991.

[72] T. Van Cutsem, M. Glavic, W. Rosehart, C. Canizares, M. Kanatas, L. Lima, F. Milano, L. Papangelis, R. A. Ramos, J. A. d. Santos, B. Tamimi, G. Taranto, and C. Vournas, “Test systems for voltage stability studies,” *IEEE Transactions on Power Systems*, vol. 35, no. 5, pp. 4078–4087, 2020.

[73] V. Ajjarapu and C. Christy, “The continuation power flow: a tool for steady state voltage stability analysis,” *IEEE transactions on Power Systems*, vol. 7, no. 1, pp. 416–423, 1992.

[74] North American Electric Reliability Council, “Transmission capability margins and their use in ATC determination,” 1999, white paper.

10. List of Abbreviations

AGC	Automatic Generation Control
AVR	Automatic Voltage Regulator
CE	Capacity Event
CF	Complex Frequency
CIG	Converter Interfaced Generator
COI	Center-Of-Inertia
DER	Distributed Energy Resource
DG	Distributed Generator
DN	Distribution Network
EC	Energy Community
EMT	Electromagnetic Transient
ESS	Energy Storage System
FDF	Frequency Divider Formula
KPI	Key Performance Indicator
PCC	Point of Common Coupling
PEV	Plug-in Electric Vehicle
PFC	Primary Frequency Control
PI	Proportional-Integral
PLL	Phase-Locked Loop
POC	Point of Connection
SFC	Secondary Frequency Control
SM	Synchronous Machine
SVC	Static Var Compensator
TCL	Thermostatically-Controlled Load
TSO	Transmission System Operator
UF	Utility Function
ULTC	Under-Load Tap Changer
VDL	Voltage-Dependent Load
VPP	Virtual Power Plant
VSG	Virtual Synchronous Generator
VSM	Virtual Synchronous Machine
WPP	Wind Power Plant
WSCC	Western Systems Coordinating Council

ANNEX

A.1 Revisited Scenario Description

This section provides an update to the frequency control scenarios defined in deliverable D2.1 [23]. The modifications with respect to the scenario description provided in D2.1 are three, namely, this section (i) defines a new use case for scenario FC_A, namely Use Case FC_A.2; (ii) provides a modification in the description of Use Case FC_B.2 of scenario FC_B; and (iii) provides a modification in the description of Use Case FC_E.1 of scenario FC_E.

A.1.1 Use Case FC_A.2: Modified New England System

A.1.1.1 Narrative of the Use Case

The goal of this use case is to study the dynamic response of power systems with inclusion of DERs that participate in the PFC. This use case is based on the New England system described in Section 2.5.3 of deliverable D2.1. The system is modified to connect the dynamic models of DERs of different technologies.

A.1.1.2 KPIs

The following are the Key Performance Indicators (KPIs) that are evaluated in this use case:

- Frequency of the COI of the SMs connected to the system.
- Bus voltage profiles of the system.
- Voltage/frequency performance metric μ described in Section 3.3.2.

A.1.2 Updated Use Case FC_B.2: Modified New England System

This use case is modified to include the study of the dynamic response of VPPs that participate in the PFC. With this change, the updated narrative of the use case is as follows.

The goal of this use case is to study the dynamic response of VPPs *that participate in the* PFC *and* SFC *of a power system. The use case also serves to study the dynamic response of aggregated* VPP *models. This use case is based on the New England system described in Section 2.5.3 of D2.1. The system is modified to include a* VPP.

A.1.3 Updated Use Case FC_E.1: Modified WSCC System

This use case is modified to include the parameter estimation of non-synchronous devices, such as VDLs, as well as the assessment of bus frequency estimation methods. The updated narrative of the use case is as follows.

The goal of this use case is to estimate the inertia and equivalent inertia of synchronous and non-synchronous, respectively, devices connected to a power grid, the parameters of non-synchronous device models, such as the voltage exponents of VDLs*, as well as to assess bus frequency estimation methods. To this aim, the WSCC system described in Section 2.5.1 of D2.1 is modified to include non-synchronous devices of different technologies, such as* VDLs*,* ESSs*, Thermostatically-Controlled Loads (TCLs),* WPPs*, and Virtual Synchronous Machines (VSMs), of which the equivalent inertia and parameter estimation is of interest*.

The updated KPIs of the use case are as follows:

- *Error between actual and estimated inertia constant.*
- *Error between estimated and actual parameter of non-synchronous device.*

A.2 Revisited Description of Model Components

A.2.1 Voltage Controllers of Non-Synchronous Devices

This section outlines the basic voltage control schemes of DERs and ESSs. These models are utilized to test the control schemes described in Chapter 3.

A.2.1.1 Distributed Energy Resources

Figure 8 shows the DER model voltage control structure. It consists of an inner loop that regulates the q-axis current component and an outer loop for voltage control. The voltage control loop applies a PI control to the error $v^{\mathrm{ref}} - v_h$ and the output is fed to the DER reactive power reference.

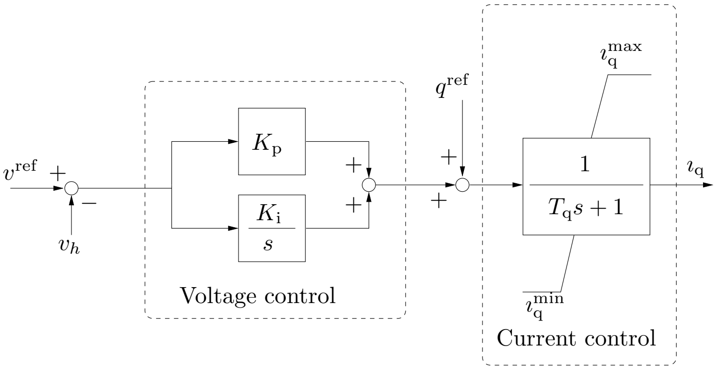

Figure 8 – Voltage control scheme of DER model

A.2.1.2 Energy Storage Systems

Figure 9 shows the voltage control structure of the ESS. The voltage control loop filters the voltage error and implements a lead-lag control whose output is fed to the ESS reactive power dynamics.

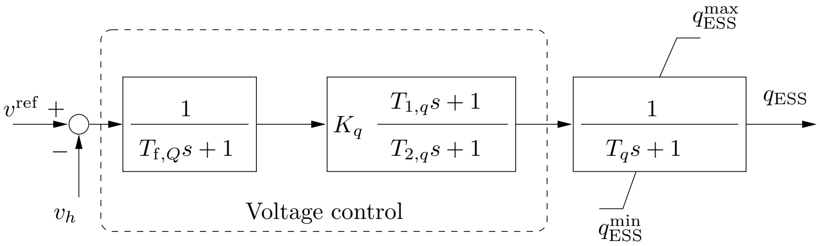

Figure 9 – Voltage control scheme of ESS model

A.2.2 PEV Fleets Model

Statistical analyses have shown that in the near future a significant number of PEVs is expected to charge in a domestic scenario [62, 63], as soon as the drivers come back home after work [48, 64]. In this case, the number of connected PEVs may quickly increase in a short time, e.g. right before dinner time, and may give rise to a new evening load peak. This peak of PEV domestic charging can be modeled as many active power load ramps at some buses of the network, where other conventional loads are also present. The load model at buses where PEVs are also connected is:

$$p = p_0 + R_{\mathrm{PEV}}(t - t_0) + \eta_p \,, \quad \dot{\eta}_p = -a\eta_p + b\xi_p \,, \tag{A.1}$$

where p is the total load; p_0 is the aggregated pre-existing VDL; R_{PEV} is the ramp rate of the PEVs; t_0 is the time at which the evening ramp begins; η_p is a Gaussian mean-reverted stochastic process that reproduces load random fluctuations; a is the drift; b is the diffusion; and ξ_p is white noise [65].

A.3 Derivation of Complex Frequency

For the sake of the derivation, it is convenient to drop the dependency on time and rewrite (2.7) in an element-wise notation. For a network with n buses, one has:

$$\begin{aligned} p_h &= v_h \textstyle\sum_{k=1}^{n} v_k \, \left[G_{hk} \, \cos\theta_{hk} + B_{hk} \, \sin\theta_{hk} \right] \, , \\ q_h &= v_h \textstyle\sum_{k=1}^{n} v_k \, \left[G_{hk} \, \sin\theta_{hk} - B_{hk} \, \cos\theta_{hk} \right] \, , \end{aligned} \tag{A.2}$$

where G_{hk}, B_{hk} are the real and imaginary part of the element (h, k) of the network admittance matrix, i.e. $\bar{Y}_{hk} = G_{hk} + \jmath B_{hk}$; v_h, v_k are the voltage magnitudes at buses h and k, respectively; and $\theta_{hk} = \theta_h - \theta_k$, where θ_h and θ_k are the voltage phase angles at buses h and k, respectively. $h = 1, 2, \ldots, n$. Equations (A.2) can be equivalently written as:

$$p_h = \textstyle\sum_{k=1}^{n} p_{hk} \, , \quad \text{and} \quad q_h = \textstyle\sum_{k=1}^{n} q_{hk} \, , \tag{A.3}$$

where

$$\begin{aligned} p_{hk} &= v_h v_k \, \left[G_{hk} \, \cos\theta_{hk} + B_{hk} \, \sin\theta_{hk} \right] \, , \\ q_{hk} &= v_h v_k \, \left[G_{hk} \, \sin\theta_{hk} - B_{hk} \, \cos\theta_{hk} \right] \, . \end{aligned} \tag{A.4}$$

Differentiating (A.2) gives [13]:

$$dp_h = \textstyle\sum_{k=1}^{n} \dfrac{\partial p_h}{\partial \theta_{hk}} \, d\theta_{hk} + \textstyle\sum_{k=1}^{n} \dfrac{\partial p_h}{\partial v_k} \, dv_k \equiv dp_h' + dp_h'' \, . \tag{A.5}$$

$$dq_h = \textstyle\sum_{k=1}^{n} \dfrac{\partial q_h}{\partial \theta_{hk}} \, d\theta_{hk} + \textstyle\sum_{k=1}^{n} \dfrac{\partial q_h}{\partial v_k} \, dv_k \equiv dq_h' + dq_h'' \, . \tag{A.6}$$

In (A.5), dp_h is the total variation of power at bus h; dp_h' is the quota of the active power that depends on bus voltage phase angle variations; and dp_h'' is the quota of active power that depends on bus voltage magnitude variations. From (A.3), it is relevant to observe that $\frac{\partial p_h}{\partial \theta_{hk}} = -q_{hk}$, and $\frac{\partial q_h}{\partial \theta_{hk}} = p_{hk}$. Recalling also that $\theta_{hk} = \theta_h - \theta_k$ and using (A.3), leads to rewrite dp_h' and dq_h' as:

$$dp_h' = -q_h \, d\theta_h + \textstyle\sum_{k=1}^{n} q_{hk} \, d\theta_k \, , \quad dq_h' = p_h \, d\theta_h - \textstyle\sum_{k=1}^{n} p_{hk} \, d\theta_k \, . \tag{A.7}$$

In the same vein, from (A.3), (A.5) and (A.6), dp_h'' and dq_h'' can be rewritten as:

$$dp_h'' = \frac{p_h}{v_h} \, dv_h + \textstyle\sum_{k=1}^{n} \dfrac{p_{hk}}{v_k} \, dv_k \, , \quad dq_h'' = \dfrac{q_h}{v_h} \, dv_h + \textstyle\sum_{k=1}^{n} \dfrac{q_{hk}}{v_k} \, dv_k \, . \tag{A.8}$$

Let us define the quantity $u_h \equiv \ln(v_h)$, where both the logarithm and its argument are dimensionless. With this aim, v_h is in per unit, namely it is the ratio of two voltages (thus without units). Considering the differential of u_h, (A.8) can be rewritten as [13]:

$$dp_h'' = p_h \, du_h + \textstyle\sum_{k=1}^{n} p_{hk} \, du_k \, , \quad dq_h'' = q_h \, du_h + \textstyle\sum_{k=1}^{n} q_{hk} \, du_k \, . \tag{A.9}$$

Equations (A.7) and (A.9) can be expressed in terms of complex power variations:

$$\begin{aligned} d\bar{s}_h' &= dp_h' + \jmath dq_h' = \jmath \bar{s}_h \, d\theta_h - \jmath \textstyle\sum_{k=1}^{n} \bar{s}_{hk} \, d\theta_k \, , \\ d\bar{s}_h'' &= dp_h'' + \jmath dq_h'' = \bar{s}_h \, du_h + \textstyle\sum_{k=1}^{n} \bar{s}_{hk} \, du_k \, , \end{aligned} \tag{A.10}$$

and, finally, defining the complex quantity $\bar{\zeta}_h \equiv u_h + \jmath \, \theta_h$, the total complex power variation can be written in a compact matrix form, as follows [13]:

$$d\bar{\boldsymbol{s}} = \bar{\boldsymbol{s}} \circ d\bar{\boldsymbol{\zeta}} + \bar{\mathbf{S}} \, d\bar{\boldsymbol{\zeta}}^* \, , \tag{A.11}$$

where $\bar{\mathbf{S}} \in \mathbb{C}^{n \times n}$ is a matrix whose (h, k)-th element is $\bar{s}_{hk}$. Expression (A.11) has been obtained in general, i.e., assuming a differentiation with respect to a generic independent parameter. If this parameter is the time t, (A.11) the we arrive at (2.8), where $\bar{\boldsymbol{\eta}} = \dot{\bar{\boldsymbol{\zeta}}} = \dot{\boldsymbol{u}} + \jmath \dot{\boldsymbol{\theta}}$. Recalling that $\boldsymbol{\omega}(t) = \dot{\boldsymbol{\theta}}(t) = \dot{\boldsymbol{\vartheta}}(t) - \omega_o(t)$ and defining $\boldsymbol{\varrho} \equiv \dot{\boldsymbol{u}}$, we obtain (2.9). Note that both real and imaginary part of (2.9) have, in fact, the dimension of s^{-1}, as $\boldsymbol{u}$ is dimensionless and $\boldsymbol{\omega}$ is expressed in rad/s.

From the definition of u_h, one has $v_h = \exp(u_h)$, i.e., the magnitude of the voltage is expressed as a function whose derivative is equal to the function itself. This concept is key in the theory of Lie groups and algebra, which defines the space of linear transformations of generalized "rates of change" [66].

Another way to write (2.8) is by splitting $\dot{\bar{\boldsymbol{s}}}$ into its components $\dot{\bar{\boldsymbol{s}}}'$ and $\dot{\bar{\boldsymbol{s}}}''$. According the definitions of $\bar{\boldsymbol{s}}'$ and $\bar{\boldsymbol{s}}''$, $\dot{\bar{\boldsymbol{s}}}'$ does not depend on $\boldsymbol{\varrho}$, whereas $\dot{\bar{\boldsymbol{s}}}''$ does not depend on $\boldsymbol{\omega}$, as follows:

$$\begin{aligned} \dot{\bar{\boldsymbol{s}}}' &= \jmath \bar{\boldsymbol{s}} \circ \boldsymbol{\omega} - \jmath \bar{\mathbf{S}}\, \boldsymbol{\omega}\,, \\ \dot{\bar{\boldsymbol{s}}}'' &= \bar{\boldsymbol{s}} \circ \boldsymbol{\varrho} + \bar{\mathbf{S}}\, \boldsymbol{\varrho}\,. \end{aligned} \tag{A.12}$$

It is important to note that, in general, the expressions of $\dot{\bar{\boldsymbol{s}}}'$ and $\dot{\bar{\boldsymbol{s}}}''$ are not known *a priori*. These components, however, can be determined using (2.8), (A.12) and:

$$\dot{\bar{\boldsymbol{s}}} = \dot{\bar{\boldsymbol{s}}}' + \dot{\bar{\boldsymbol{s}}}''\,. \tag{A.13}$$

For the sake of completeness, we finally note that, an important aspect of the developments discussed in this section is whether (2.7) can be differentiated with respect to an independent variable and, in particular, with respect to time. With this regard, the interested reader is referred to [13].

We now derive (2.8) in an alternative and more compact formulation as a function of the currents. First, observe that:

$$\dot{\bar{\boldsymbol{v}}} = \bar{\boldsymbol{v}} \circ \bar{\boldsymbol{\eta}}\,. \tag{A.14}$$

The proof of the last expression is given in [13]. Using this expression, as well as the time derivative of $\bar{s}$ with respect to the dq-axis reference frame, we arrive at (2.10) [13].

Another way to write (2.8) is by differentiating with respect to time (2.5) or by dividing each row of $\bar{\mathbf{S}}$ by the corresponding voltage $\bar{v}_h$ in (2.10). Implementing this division and using (A.14) gives:

$$\dot{\bar{\boldsymbol{\imath}}} = \bar{\mathbf{Y}}\, [\bar{\boldsymbol{v}} \circ \bar{\boldsymbol{\eta}}] = \bar{\mathbf{Y}}\, \mathrm{diag}(\bar{\boldsymbol{v}})\, \bar{\boldsymbol{\eta}}\,, \tag{A.15}$$

and, defining $\bar{\mathbf{I}} = \bar{\mathbf{Y}}\, \mathrm{diag}(\bar{\boldsymbol{v}})$, we arrive at (2.11) [13].

A.4 Simulation Results

This section presents the simulation results on the concepts and techniques described in this deliverable. All results are obtained using the power system analysis software tool Dome [67].

A.4.1 Behavior of CF During Transients

This section presents simulation results that illustrate the behavior of the CF described in Chapter 2. Results are obtained using the WSCC system.

A.4.1.1 Behavior of CF components

Figures 10 and 11 show the transient behavior of the 2 components of the CF at a generator and a load bus, bus 2 and bus 8, respectively. The estimation of ω_h and ϱ_h at grid buses is obtained through a synchronous-reference frame PLL model [23, 68].

Simulation results show that $|\omega_h| \gg |\varrho_h|$. This inequality holds for all networks and scenarios that we have tested for the preparation of this work.

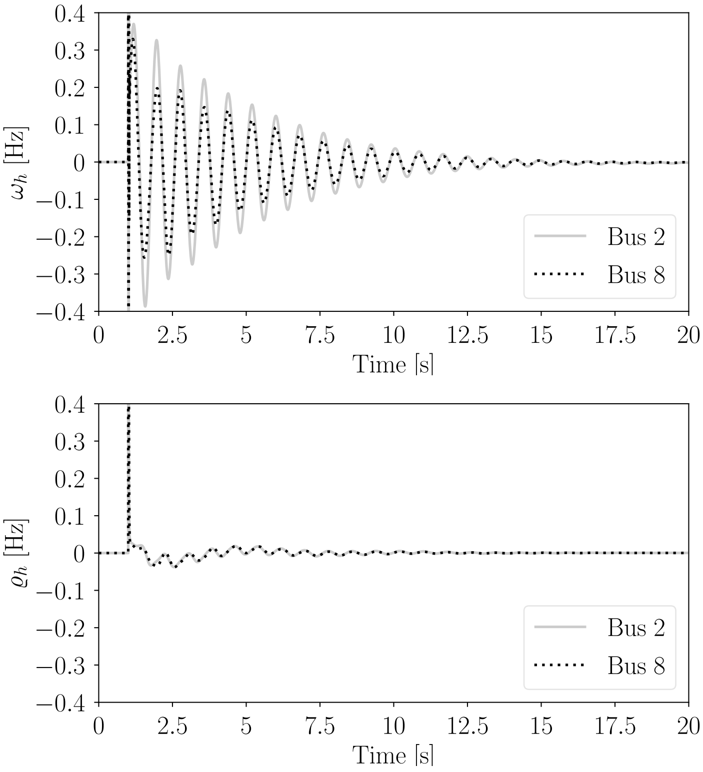

Figure 10 – Use Case FC_E.1 – CF components: outage of load at bus 5

A.4.1.2 Bus Frequency Estimation

The implementation of (2.8) in a software tool for the simulation of power systems can be useful to determine the “exact” frequency variations at network buses in a RMS model for transient stability analysis. This topic has been discussed and solved under various hypotheses in [4, 5, 6]. In particular, the FDF proposed in [5] is based on (2.12), which is an approximation of (2.8).

The expression (2.8) states the link between the CF and the rest of the variables of the system. Thus, in (2.8), the unknowns are $\bar{\boldsymbol{\eta}}$ or, equivalently, $\boldsymbol{\rho}$ and $\boldsymbol{\omega}$. One can, of course, calculate these quantities by differentiating with respect to time $\boldsymbol{u}$ and $\boldsymbol{\theta}$, respectively. However, since $\boldsymbol{u}$ and $\boldsymbol{\theta}$

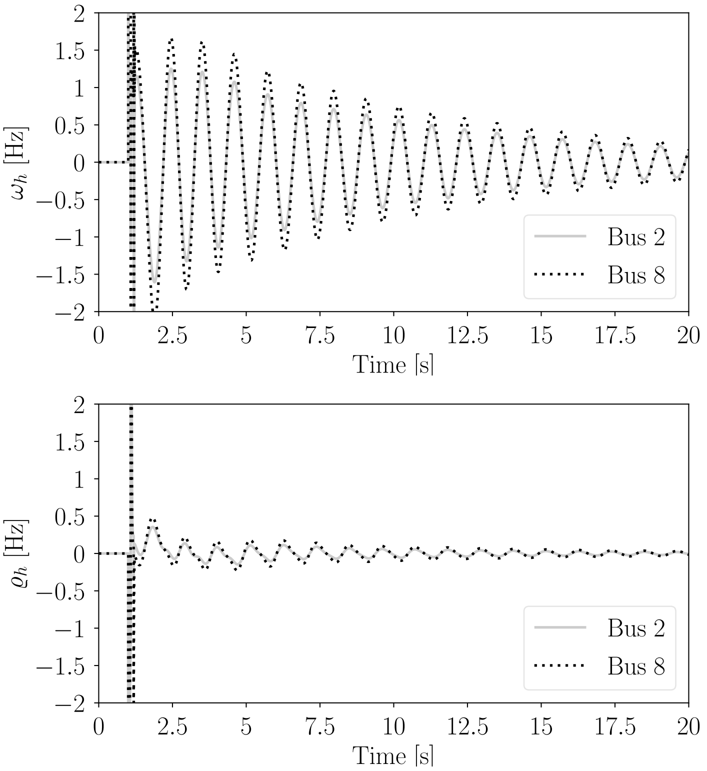

Figure 11 – Use Case FC_E.1 – CF components: fault at bus 7 cleared by tripping line 5-7

are algebraic variables, the numerical solution of the system model does not provide directly the values of their time derivatives. So either one has to use some sort of numerical differentiation (with the issues that arise at discontinuities); use some sort of estimation (e.g., the PLL utilized in the previous example); or solve (2.8). The latter is the approach utilized in this example.

The procedure implemented in the simulations of this section is detailed in [13]. Figure 12 shows the imaginary part of the CF as obtained using a 4th and a 2nd order model of the SMs, as well as for a scenario where the SM at bus 3 is substituted for a Converter Interfaced Generator (CIG). The model used to represent the CIG in this example is provided in [13]. The plots refer to the disconnection at $t = 1$ s of the load at bus 5. The results obtained using PLLs matches well the "exact" results obtained with the CF except for the numerical spikes that follow the load disconnection and a small delay that is due to the control loop of the PLL. The proposed formula is also robust with respect to noise as shown in Figure 12b.

The events create spikes in the estimation of ω obtained with the PLL. The behavior of ω as estimated with the CF, on the other hand, depends on the dynamics of the device connected to the bus where the frequency is estimated. It is smooth for the 2nd order SM and show a small jump for the 4th order SM. The latter behavior is due to the dependence of the frequency on the voltage magnitude, which is modeled as an algebraic variable. On the other hand, the behavior of the ω estimated with the CF at the CIG bus shows a relatively fast transient after the load disconnection (see Figure 12d). This is due to the dynamics of the currents of the converter.

Figure 12 also shows the results obtained using the FDF. The FDF matches closely the results of the proposed method when considering the simplified 2nd order model of the SMs but introduces some errors if the SM model includes rotor flux dynamics or when considering the CIG.

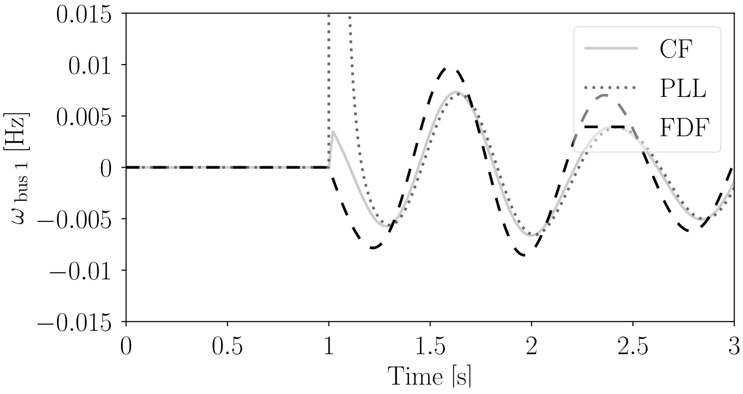

(a) 4th order machine models

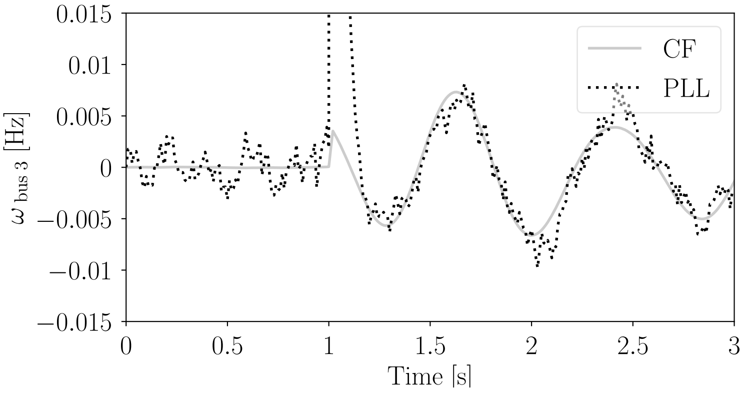

(b) 4th order machine models & noise

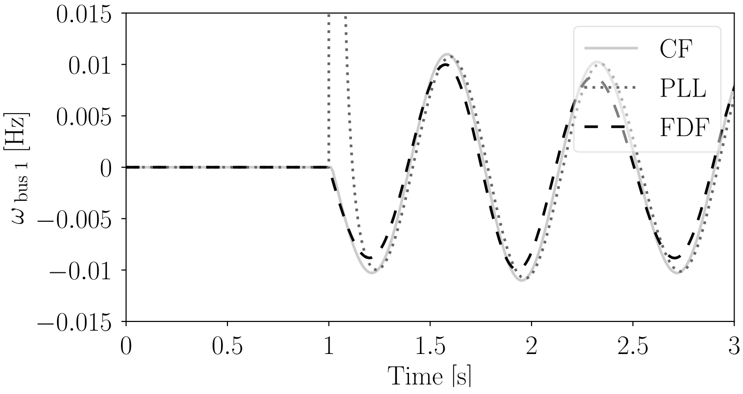

(c) 2nd order machine models

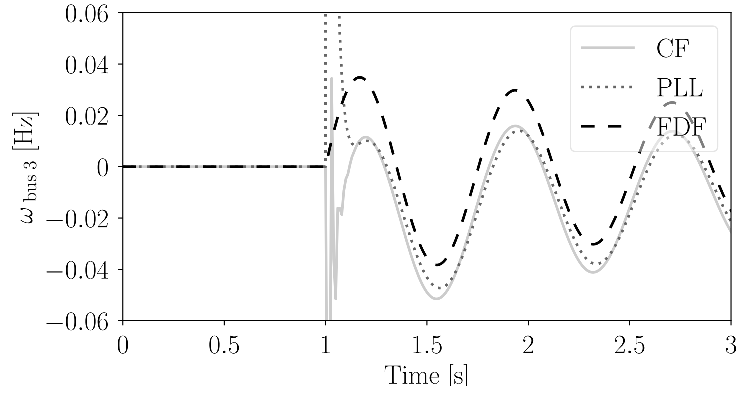

(d) CIG connected to bus 3

Figure 12 – Use Case FC_E.1 – Bus frequencies using PLL, FDF and CF

A.4.2 Combined Voltage-Frequency Control

A.4.2.1 FC+MRVC Scheme

This section presents simulation results on the modified voltage reference control scheme presented in Section 3.2. The parameters used for the DER and ESS controls are provided in [22].

A.4.2.1.1 DERs Connected to Buses 2 and 3

We test the impact of voltage reference (3.5) on the frequency regulation provided by the DERs connected to buses 2 and 3 of the modified WSCC system. In this scenario, no ESS is included in the system. The control modes that include frequency regulation consider as frequency control input signal the frequency of the COI, which, since there is only one SM left in the system, coincides with the rotor speed of the SM connected to bus 1 (ω_1). Moreover, for the FC+MRVC, the DERs at buses 2 and 3 are connected to the transmission system in antenna and thus require the voltage magnitudes at buses 7 (v_7) and 9 (v_9), respectively, to implement reference (3.5).

We consider the transient that follows the tripping of the line that connects buses 4 and 6. Results are presented in Figures 13-15. In particular, Figure 13 shows the the rotor speed of the SM (in Hz) following the disturbance. The system dynamic behavior for the CPC and FC is not acceptable, while for the examined disturbance, inclusion of the voltage control loop significantly improves the frequency response. The FC+MRVC provides a further significant improvement in the frequency regulation (> 0.1 Hz) with respect to the FC. A comparison of the voltage references of the FC+MRVC and FC+VC for the DER connected to bus 2 is shown in Figure 14. It is important to note that the improvement provided by the FC+MRVC comes without jeopardizing the voltage response of the system. This is shown in Figure 15. Overall, in the case of a line trip, the FC+MRVC provides an important improvement in the frequency regulation of the system. We have applied trips to other lines of the network and obtained similar results and same conclusions.

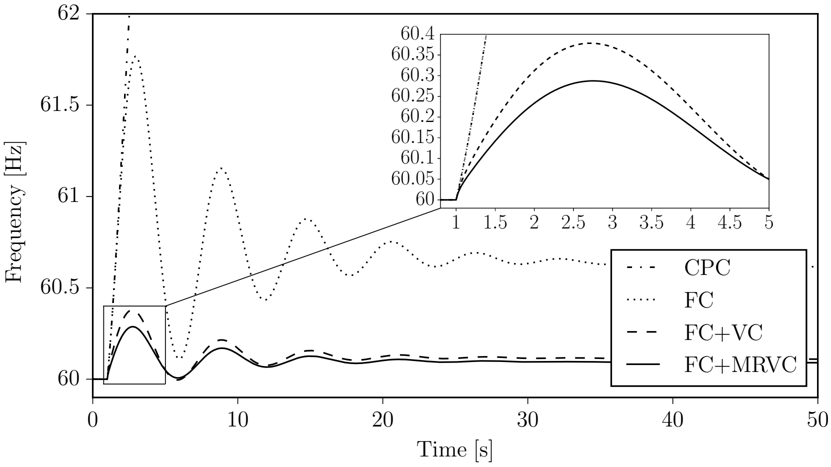

Figure 13 – Use Case FC_A.1 – Frequency response after the outage of line 4-6

A.4.2.1.2 ESS Connected to Bus 5

In this scenario, an ESS is connected to bus 5 of the modified WSCC system. The objective is to assess the impact of the FC+MRVC on the frequency response provided by the ESS. With this aim, in this scenario, the DERs connected to buses 2 and 3 do not provide frequency and voltage control (see CPC in Section A.4.2.1.1).

The test system is simulated considering a three-phase fault at bus 6. The fault occurs at $t = 1$ s and is cleared after 80 ms by tripping the line that connects buses 6 and 9. Two modes are com-

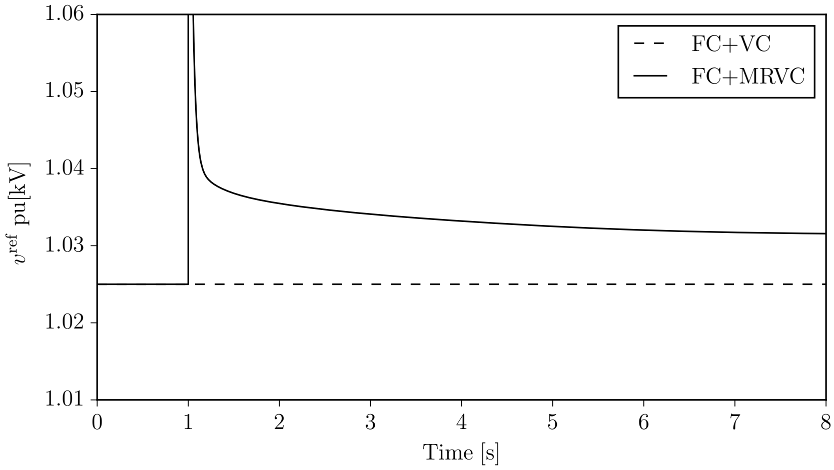

Figure 14 – Use Case FC_A.1 – DER at bus 2: voltage reference after the outage of line 4-6

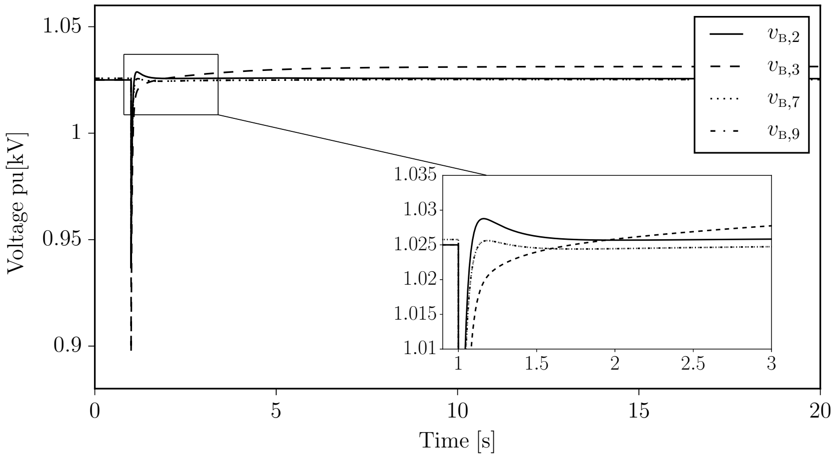

Figure 15 – Use Case FC_A.1 – Voltage response following the outage of line 4-6, FC+MRVC

pared for the ESS control: FC+VC and FC+MRVC. The voltage reference (3.5) of the FC+MRVC is implemented with the measurements of the voltage magnitudes at buses 4 and 7. The frequency response of the system is shown in Figure 16. The FC+MRVC provides a significant improvement in the frequency regulation of the system, while this is achieved in an economic way, since a lower variation of the stored energy is required (see Figure 17).

We have thoroughly tested the dynamic behavior of the modified WSCC system with inclusion of the FC+MRVC for a variety of different contingencies. There exist scenarios for which the difference between the FC+MRVC and FC+VC is smaller than the cases shown in Figures 13 and 16. In Figure 18, we consider a 15 % sudden increase of the susceptance and conductance of all system loads occurring at $t = 1$ s. In this case, FC+VC and FC+MRVC show substantially the same dynamic behavior. In general, we can conclude that the FC+MRVC, in the cases where it is not beneficial, at least does not worsen the dynamic response of the system.

A.4.2.2 FVP+FVQ Control Scheme

This section presents simulation results on the combined voltage-frequency control scheme presented in Section 3.3. The parameters of the DER frequency, voltage, and inner current controllers are given in [69]. To ensure a fair comparison, different control modes are compared keeping constant control parameters. Note that, when preparing the simulations, we also tried different approaches, e.g. we tuned each mode separately with an aim to achieve the best dynamic response. However, since, as discussed above, the controllers perform well for a relative large range of their parameters, their set up does not modify the main conclusions that are drawn in this section.

A.4.2.2.1 FQ and VP Control Modes

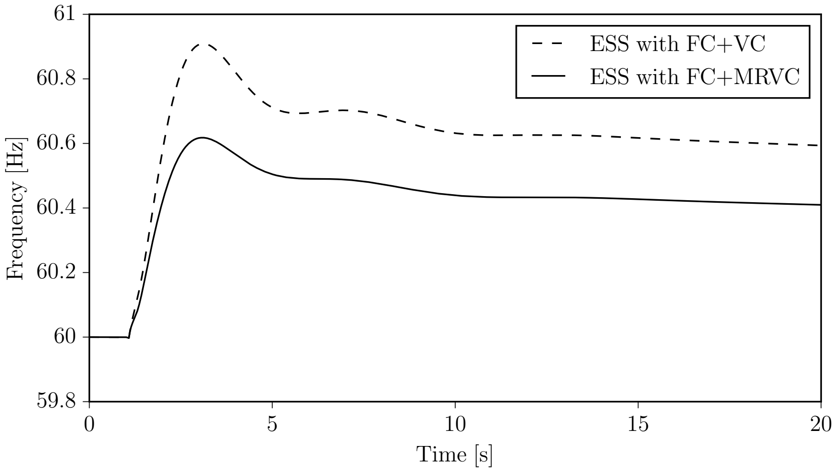

Figure 16 – Use Case FC_A.1 – Frequency response following a three-phase fault

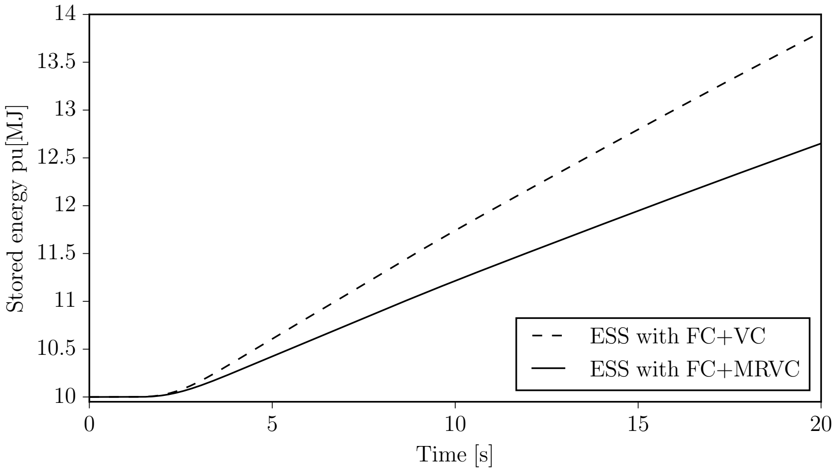

Figure 17 – Use Case FC_A.1 – ESS stored energy following a three-phase fault

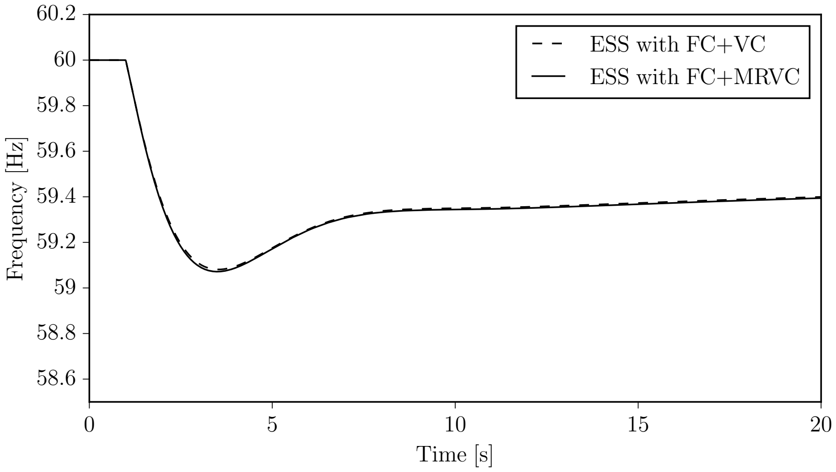

Figure 18 – Use Case FC_A.1 – Frequency response following a load increase

In this section, we consider the FQ and VP controls, which are the components that differentiate the FVP+FVQ control strategy from the classical approach, where frequency and voltage regulation are provided only by means of FP and VQ, respectively (see mode definitions in Section 3.3.1). We first examine the FQ mode, i.e. the ability of DERs 1-3 to improve the dynamic response of the system by controlling the frequency through the reactive power. To this aim, the system is simulated for both positive/negative signs of the input control error assuming the tripping of Gen 10. lResults are shown in Figure 19 where, for the sake of comparison, we have included the response of the system when DERs (i) do not provide any control and (ii) act based on the classic FP control. Figure 19 indicates that the FQ control improves the COI frequency response of the system if utilized with input error $\epsilon_\omega = \omega - \omega^{\mathrm{ref}}$. The main reason for FQ's effectiveness in this case is that the DERs respond to the under-frequency by reducing their reactive power injection and thus the voltage levels at the network. Due to the voltage dependency of loads the power demand level decreases, thus reducing the imbalance and helping the recovery of the frequency [69]. Note that the improvement provided by the FQ mode is lower than the one of the classic FP. This result is as expected. Yet, as shown in Section A.4.2.2.5, the benefits of using FQ are more apparent when applied at the DN level.

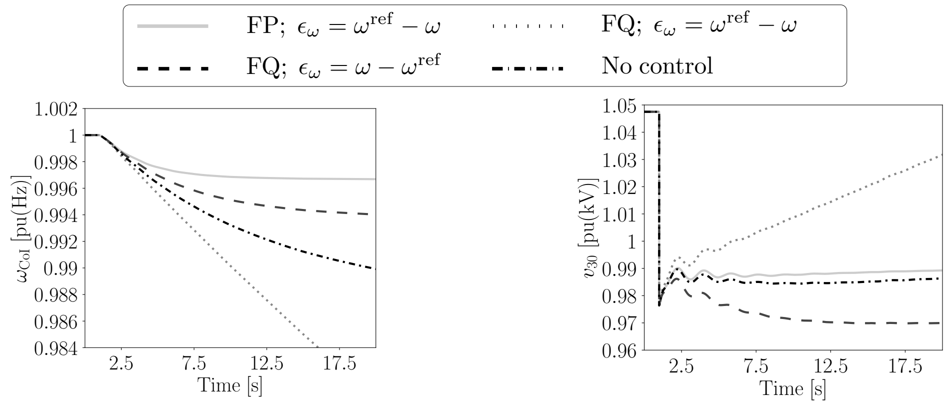

(a) COI frequency **(b) Voltage at bus 30**

Figure 19 – Use Case FC_A.2 – Transient response following the loss of Gen 10

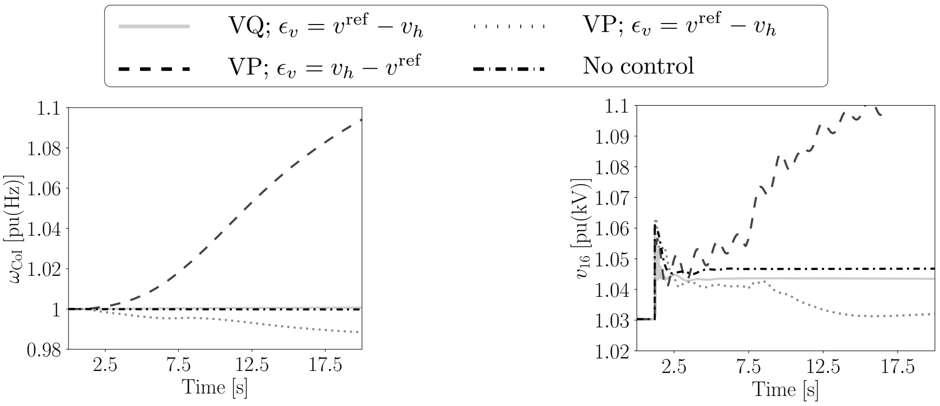

(a) COI frequency **(b) Voltage at bus 16**

Figure 20 – Use Case FC_A.2 – Transient response following the outage of line 15-16

We show the effect of regulating the voltage at the DER terminal bus through its active power injection, i.e. the VP mode. A simulation is carried out considering the outage of line 15-16 and results are shown in Figure 20. The VP mode improves the transient behavior of the voltage when the control input error is $\epsilon_v = v^{\mathrm{ref}} - v_h$. However, as shown in [69], this mode also introduces large deviations in the power sharing among the DERs connected to the system and thus, using it individually is not suggested. The VP can still contribute to improve the overall system dynamic response if utilized with a relatively small gain and as an auxiliary control that coordinates with other modes. This point is further discussed in the remainder of this study.

We note that, for the frequency response of the system to improve, ϵ_ω in FQ has to be the opposite from the one utilized in FP. The need for opposite actions when regulating the frequency through the active and reactive power, respectively, can be also observed in the structure of (3.7). On the other hand, to improve the voltage regulation, ϵ_v needs to be implemented with the same sign for both VP and VQ modes. This is again consistent with (3.7), which suggests that regulating the voltage variations requires actions in the same direction for both active and reactive power. Hence, $\epsilon_\omega = \omega - \omega^{\mathrm{ref}}$ and $\epsilon_v = v^{\mathrm{ref}} - v_h$ are chosen for FQ and VP in this case study.

A.4.2.2.2 Performance of FVP+FVQ Control

In this subsection, we study the performance of the FVP+FVQ control scheme. This scheme is compared to the classic FP+VQ control, as well as to FP+FQ, VP+VQ, and FP+FVQ. A simulation is carried out considering the disconnection of the load at bus 3 ($p_3 = 3.22$ pu, $q_3 = 0.024$ pu). The transient behavior of the system following the disturbance is presented in Figure 21 where, the response of the system with all DER controls disconnected as well as that of the original New England system serve as references for comparison.

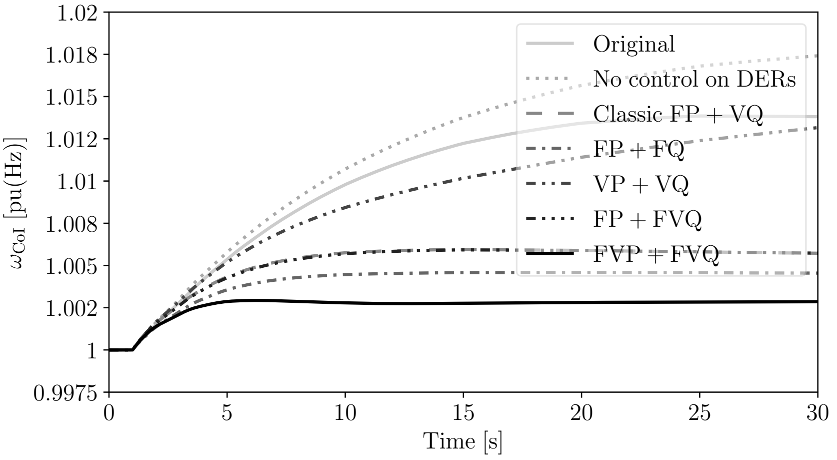

(a) COI frequency

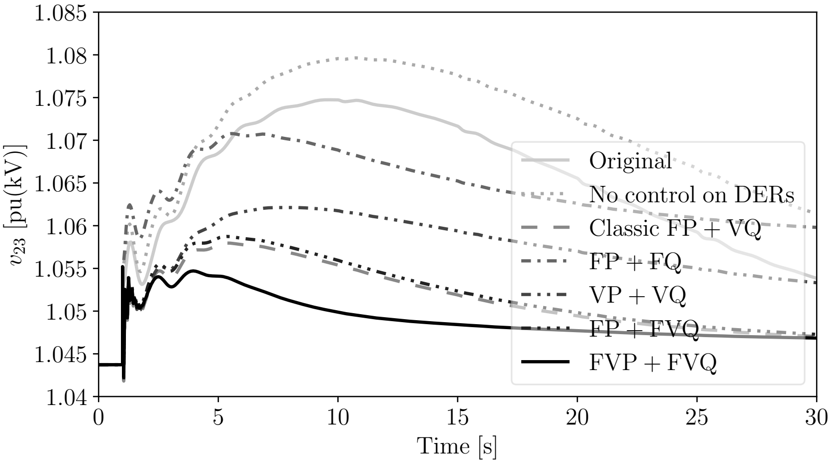

(b) Voltage at bus 23

Figure 21 – Use Case FC_A.2 – Transient response after disconnection of load at bus 3

The following remarks are relevant. (i) Compared to the original system, a 30 % penetration of DERs worsens the overall dynamic behavior of the system, when these resources provide no restorative control actions. This result is as expected. (ii) The FP+FQ control shows a better frequency response than the classic FP+VQ, yet, it leads to a poor voltage behavior (see Figure 21b). (iii)

Control	Classic FP+VQ		FP+FQ		FVP+FVQ	
$\Delta\omega$ (%)	max	at 20 s	max	at 20 s	max	at 20 s
Load 3 out.	0.5814	0.5946	0.4593	0.4593	**0.2934**	**0.2817**
Load 20 out.	1.1452	1.1318	0.9476	0.9456	**0.5533**	**0.5202**
Gen 4 out.	-1.1478	-1.1404	-0.7056	-0.7050	**-0.5141**	**-0.4727**
Gen 7 out.	-1.0663	-1.0495	-0.7422	-0.7348	**-0.5393**	**-0.4826**
Line 8-9 out.	0.0231	0.0229	0.0180	0.0180	**0.0121**	**0.0118**
Line 21-22 out.	0.1610	0.1598	0.1544	0.1544	**0.1390**	**0.1354**
Fault at bus 4	**0.3066**	**-0.0201**	0.3970	-0.0217	0.3505	-0.0238
Fault at bus 8	**0.2527**	**0.0042**	0.3182	0.0049	0.2989	0.0059
Δv (%)	max	at 10 s	max	at 10 s	max	at 10 s
Load 3 out.	1.2867	0.7845	1.7309	1.5417	**1.2533**	**0.6042**
Load 20 out.	2.6464	1.5891	6.7898	6.7588	**2.6464**	**1.4299**
Gen 4 out.	-7.4634	-3.5033	-10.319	-10.264	**-7.4634**	**-3.2346**
Gen 7 out.	-4.8425	-2.9453	-8.0907	-8.0907	**-4.8425**	**-2.8840**
Line 8-9 out.	-2.8946	-1.9047	-2.8946	-1.9217	**-2.8946**	**-1.9044**
Line 21-22 out.	-6.2882	-4.2634	-6.6219	**-4.1781**	**-6.2882**	-4.2203
Fault at bus 4	-100	-2.1525	-100	**-2.1329**	-100	-2.1749
Fault at bus 8	-100	-1.3188	-100	**-1.3138**	-100	-1.3244

Table 1 – Use Case FC_A.2 – Frequency/voltage deviations for different contingencies and control modes, ZIP loads

Although the VP+VQ scheme shows a very good voltage response, it leads to a poor frequency response. (iv) Combining the FP+FQ and VP+VQ modes in a single scheme leads to the FVP+FVQ which provides the best frequency and voltage dynamic response among the schemes compared.

To validate the tuning of the parameters of the controllers and build the trust of the adequateness of this tuning for the system stability, we have assessed the transient behavior of the system for a wide range of operating conditions and disturbance scenarios. With this aim, we have tested the FVP+FVQ control under a variety of disturbances, including generator tripping, line outages, short circuits, and load disconnections. Moreover, we have considered the impact of varying the voltage dependency of loads by considering a constant impedance load model. A summary of the results obtained is presented in Tables 1, 2, where $\Delta\omega$ refers to the relative variation of the COI frequency and Δv refers to the relative variation of a bus voltage magnitude that is local to the disturbance. For each scenario, the table provides the maximum relative variations, as well as the variations few seconds for primary frequency and voltage responses after the disturbance. The smallest frequency/voltage variations obtained for each scenario are marked in bold. Simulation results suggest that, overall, the FVP+FVQ control leads to an improvement of both primary frequency and voltage regulation of the system. This improvement is significant in case of an outage of a SM, a load switching, or a line trip, while for short circuits, FVP+FVQ performs as the conventional FP+VQ. Finally, note that in contrast to commonly proposed solutions, the performance enhancement provided by FVP+FVQ comes in an inexpensive way, i.e. without the need to install any extra equipment, e.g. storage devices.

A.4.2.2.3 Performance of Voltage/Frequency Response Metric

We study the accuracy of metric μ_h, presented in Chapter 3, to assess the joint voltage/frequency response of DERs. In particular, Table 3 shows the value of the metric at bus 34, where DER 1

Control	Classic FP+VQ		FP+FQ		FVP+FVQ	
$\Delta\omega$ (%)	max	at 20 s	max	at 20 s	max	at 20 s
Load 3 out.	0.5518	0.5516	0.4082	0.4075	**0.2717**	**0.2637**
Load 20 out.	1.1378	1.1355	0.8986	0.8985	**0.5501**	**0.5246**
Gen 4 out.	-1.1029	-1.1028	-0.6199	-0.6158	**-0.4946**	**-0.4644**
Gen 7 out.	-1.0408	-1.0325	-0.6711	-0.6685	**-0.5331**	**-0.4852**
Line 8-9 out.	0.0804	0.0804	0.0657	0.0655	**0.0537**	**0.0526**
Line 21-22 out.	0.1994	0.1993	0.1840	0.1837	**0.1612**	**0.1564**
Fault at bus 4	**0.3543**	0.0294	0.4585	**0.0133**	0.4245	-0.0294
Fault at bus 8	**0.2865**	0.0276	0.3590	0.0211	0.3257	**0.0150**
Δv (%)	max	at 10 s	max	at 10 s	max	at 10 s
Load 3 out.	1.2126	0.8275	1.5831	1.4612	**1.1632**	**0.6719**
Load 20 out.	2.5097	1.5937	6.4399	6.4291	**2.5097**	**1.4550**
Gen 4 out.	-6.0130	-3.3522	-8.7384	-8.7016	**-6.0130**	**-3.1234**
Gen 7 out.	-3.6201	-2.7031	-6.9113	-6.9113	**-3.6201**	**-2.6622**
Line 8-9 out.	**2.3011**	1.7715	2.3376	1.7594	2.3220	**1.7590**
Line 21-22 out.	-5.5680	-4.0392	-6.1302	**-3.9151**	**-5.5680**	-4.0117
Fault at bus 4	-100	-2.0802	-100	**-2.0603**	-100	-2.1052
Fault at bus 8	-100	-1.2711	-100	**-1.2645**	-100	-1.2762

Table 2 – Use Case FC_A.2 – Frequency/voltage deviations for different contingencies and control modes, constant impedance loads

Load model	ZIP			Constant Impedance		
Control	FP+VQ	FP+FQ	FVP+FVQ	FP+VQ	FP+FQ	FVP+FVQ
μ_{34}	at 15 s	at 15 s	at 15 s	at 15 s	at 15 s	at 15 s
Load 3 out.	1	0.7891	**0.5467**	1	0.7543	**0.5528**
Load 20 out.	1	0.8283	**0.5327**	1	0.8029	**0.5384**
Gen 4 out.	1	0.6278	**0.4953**	1	0.5816	**0.5187**
Gen 7 out.	1	0.7171	**0.5511**	1	0.6857	**0.5665**
Line 8-9 out.	1	0.8671	**0.7708**	1	0.8192	**0.7315**
Line 21-22 out.	1	0.9544	**0.9101**	1	0.9155	**0.8602**
Fault at bus 4	**1**	1.5189	1.1792	**1**	3.4706	1.5001
Fault at bus 8	**1**	1.5611	1.2027	**1**	1.9155	1.0742

Table 3 – Use Case FC_A.2 – Metric μ_{34} (DER 1)

is connected, at $t = 15$ s and for the same disturbances considered in Tables 1, 2. The value of μ_{34} is calculated using the local voltage and its time derivative (v_{34}, dv_{34}/dt) and the variation of the COI frequency. Moreover, results are normalized so that the metric for FP+VQ at $t = 15$ s equals to 1. Comparison between Tables 3 and 1, 2, indicates that μ_h can capture the combined voltage/frequency response with good accuracy. With this regard, recall that smaller values of μ_h imply a better dynamic response. It is also worth noting that in the occurrence of a fault at bus 4 and for constant impedance loads, the FP+FQ control shows the worst dynamic response from the metric point of view, although its $\Delta\omega$ and Δv are not the worst. In fact, the voltage response for FP+PQ control in this scenario is worse than other controllers at the first 4 s of the simulation, which is not shown in Tables 1, 2, and it is not observable unless we check the full time-domain response of both frequency and voltage. μ_h captures these effects and hence, provides an accurate and convenient way to evaluate the joint frequency and voltage response of DERs.

A.4.2.2.4 Application to VPPs

This section assumes that the converter-based resources connected to buses 34, 35, 37 consist of several smaller DERs that form a VPP. For this study we consider that a varying percentage of the VPP DERs utilize the FVP+FVQ scheme, and the rest act based on the classic FP+VQ control. Figure 22 shows the results for two disturbances, (a) outage of the line 21-22, and (b) disconnection of the load connected to bus 20 ($p_{20} = 6.28$ pu, $q_{20} = 1.03$ pu). The results are compared by means of the joint frequency/voltage response metric at bus 34 (μ_{34}), where DER 1 is connected. The metric is calculated as discussed in Section A.4.2.2.3. As expected, the FVP+FVQ mode has the best performance for both disturbances, which confirms the results shown in Tables 1, 2. Interestingly, the classic FP+VQ mode combined with 20-40 % FVP+FVQ control worsens the transient response for disturbance (a). We conclude that, depending on practical requirements, the VPP operator can design its assets to apply and/or switch between different control modes.

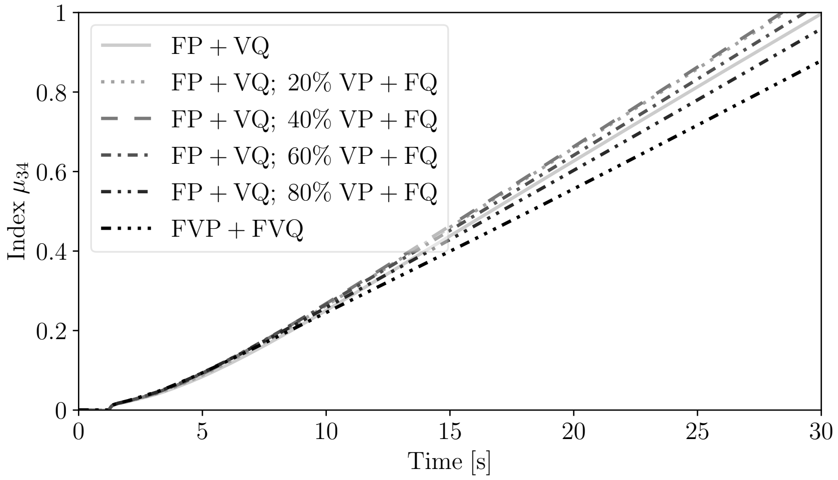

(a) Transient response following the outage of line 21-22

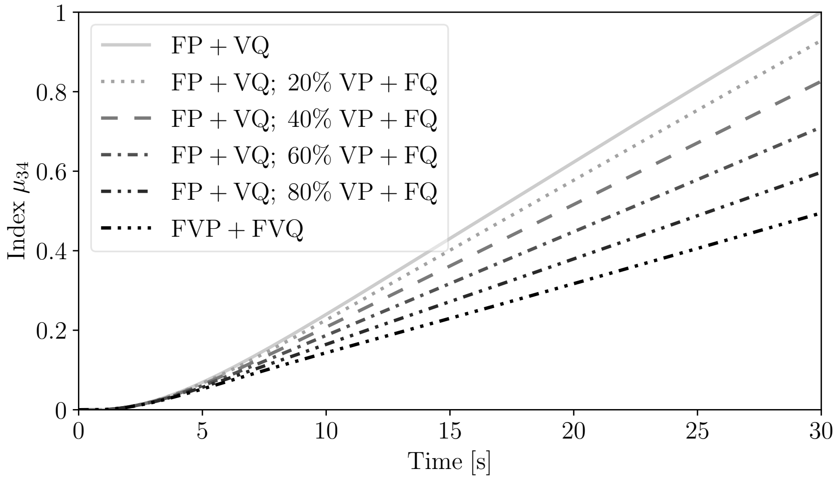

(b) Transient response following the load disconnection at bus 20

Figure 22 – Use Case FC_B.2 – μ_{34} (DER 1) for FVP+FVQ applied to a portion of VPP assets

A.4.2.2.5 Impact of Line Resistance/Reactance Ratio

In this section we study the performance of the examined control when applied to DERs integrated within DNs. To study the DN effect, the R/X ratios of the feeders that connect the DERs to the system are altered so that $R/X \approx 1$. The evolution of μ_{34} for different control modes is presented in Figure 23, where we have considered the loss of Gen 10 at $t = 1$ s. Moreover, the results are normalized so that for FP+VQ μ_{34} equals to 1 at $t = 30$ s when $R/X \ll 1$. When $R \approx X$, all DER control modes have a better performance. It is interesting to observe that for $R \approx X$, VP+VQ has the largest improvement among the examined modes. The same effect can also be observed under different disturbances in this test system. Finally, the FVP+FVQ control shows the best overall dynamic response among the modes compared.

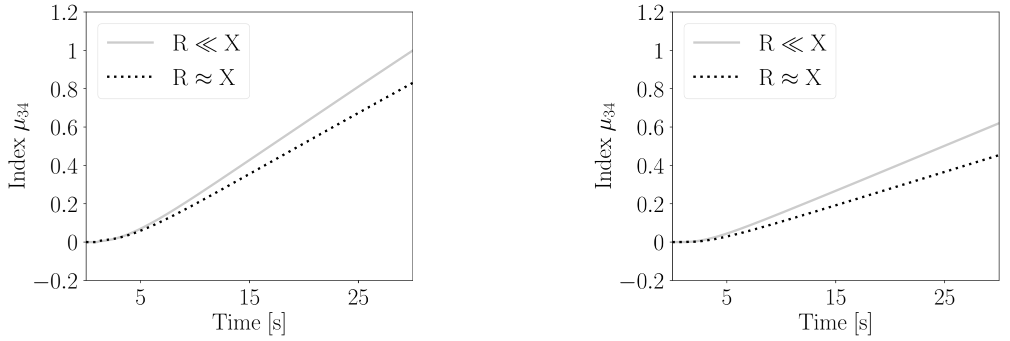

(a) FP+VQ **(b) FP+FQ**

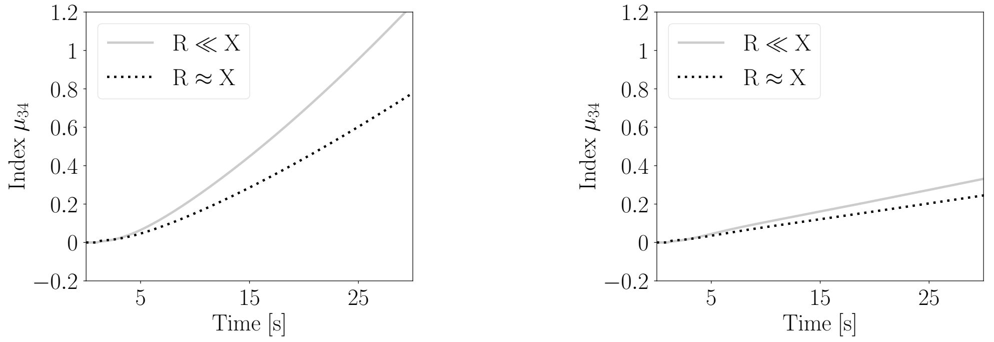

(c) VP+VQ **(d) FVP+FVQ**

Figure 23 – Use Case FC_A.2 – Transient response following the loss of Gen 10

A.4.2.2.6 Impact of DER Penetration Level

In this scenario we study the impact of the share of DERs to the total generation mix of the system on the performance of the examined control scheme. To this aim, and in addition to the DERs at buses 34, 35, 37, DERs are also connected to buses 36 and 38, by replacing the local SMs. As a consequence, the penetration of DERs to the modified IEEE 39 bus system increases to 50 %. A time-domain simulation of the system is carried out by applying the loss of Gen 10 at $t = 1$ s and results are presented in Figure 24. As it can be seen, increasing the DER penetration from 30 to 50 %, although it leads to a worse voltage response, it does not deteriorate the frequency regulation of the system, which interestingly, slightly improves. Compared to the classic FP+VQ, the FP+FQ outperforms in terms of frequency, but leads to a poor voltage response. As expected, the dual effect holds when the VP+VQ scheme is applied. Most importantly, the FVP+FVQ control leads to the best dynamic behavior among the examined control modes.

A.4.2.2.7 Impact of System Granularity

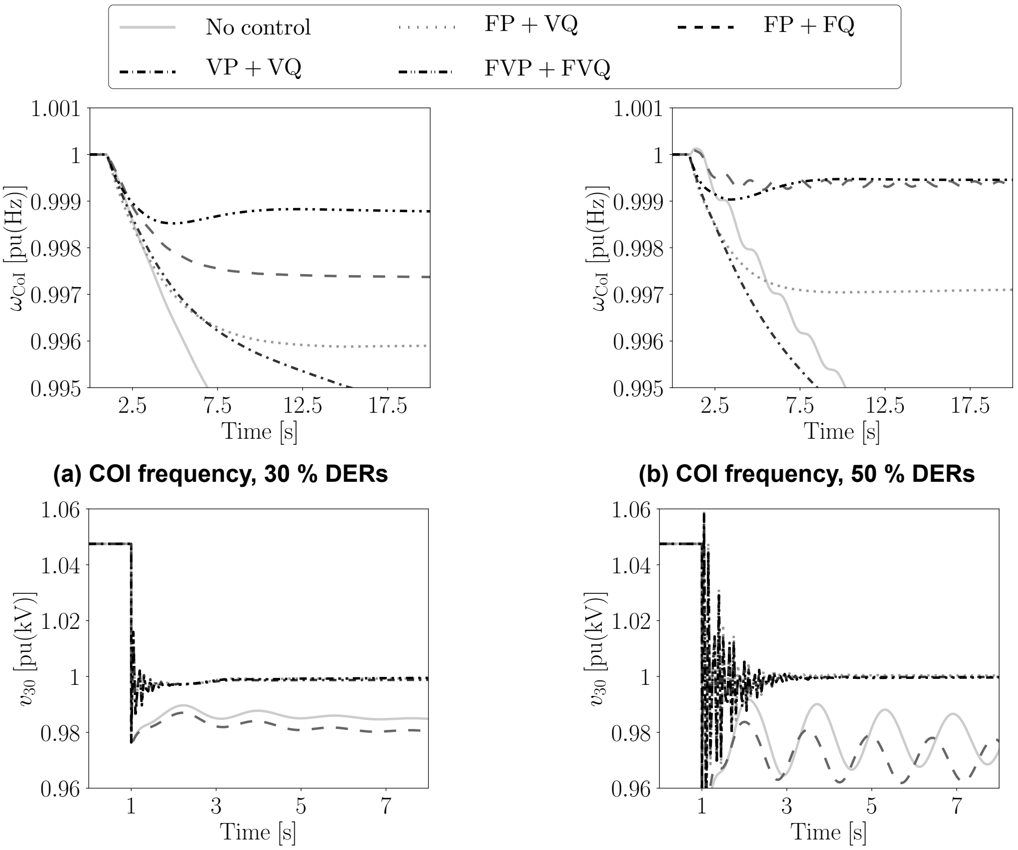

(a) COI frequency, 30 % DERs

(b) COI frequency, 50 % DERs

(c) Bus 30 voltage, 30 % DERs

(d) Bus 30 voltage, 50 % DERs

Figure 24 – Use Case FC_A.2 – Transient response following the loss of Gen 10

In this section we focus on the effect of the system's granularity and further evaluate the examined control when employed for resources at the distribution level. To this aim, a more detailed modeling of the DN and loads is considered. In particular, each of the SMs at buses 32-38 and loads at neighbor buses is substituted by the DN shown in Figure 5 [70] (for illustration, only one DN is shown in Figure 5). As a byproduct, the instantaneous DER power generation is increased to 70 %. Loads in this example are represented using the dynamic model proposed in [71]. Moreover, to account for the proximity of loads, for potential imbalances, and for possible harmonics of the power converters, noise is added on the voltage angle at every bus of the DN. Noise is modeled as an Ornstein-Uhlenbeck's process with Gaussian distribution [23, 65]. We carry out a time-domain simulation considering the disconnection of the load at bus 3.Comparison of the FP+VQ and FVP+FVQ modes is presented in Figure 25 and indicates that FVP+FVQ leads to a better dynamic behavior. Note that the control considered is in general expected to be more effective and thus lead to larger improvement of the system's response, the higher is the coupling between the active and reactive power flows, i.e. at lower voltage levels and DN applications. This is confirmed by Figure 25, when compared to results discussed in previous sections of this case study, for example with Figure 21.

A.4.2.3 Estimation of VDLs

This section presents simulation results on the VDL estimation techniques described in Section 3.4. Recall from Section 3.4 that (3.14), (3.15), although approximated, they are in general simpler to use in practice compared to (3.13), and they can be readily implemented exclusively through standard power and frequency measurements. For this reason, in Section A.4.2.3.1 we use (3.14), (3.15) and show their performance for VDLs connected at the transmission and distribution level. Then, Section A.4.2.3.2 further discusses the accuracy of these formulas by providing a comparison with the exact yet more involved expressions given in (3.13).

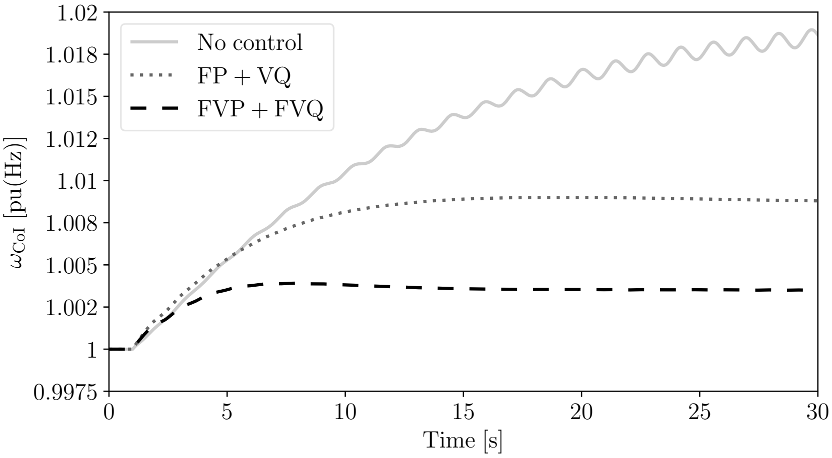

(a) COI frequency

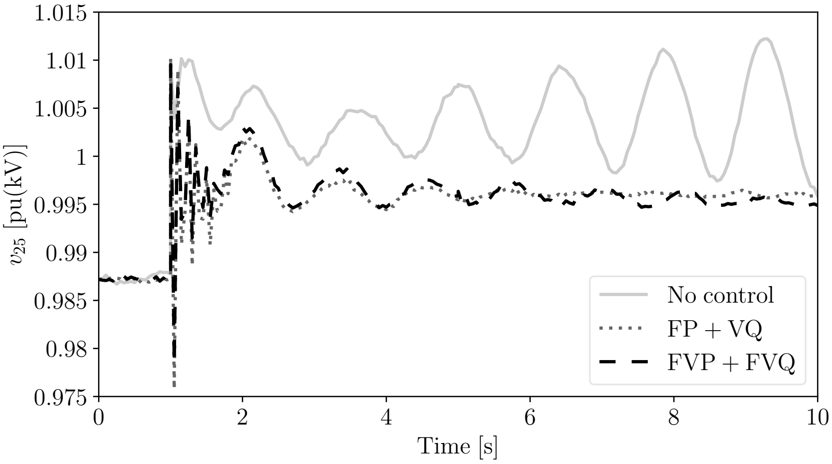

(b) Voltage at bus 25

Figure 25 – Use Case FC_A.2 – Transient response after disconnection of load at bus 3

A.4.2.3.1 Performance of formulas (3.14), (3.15)

We first consider the case of VDLs connected at the transmission level. The WSCC system, which represents a transmission system with $R_{hk}/X_{hk} \ll 1$ is considered to this aim. Figure 26 shows the ratio $\Delta p_8'/\Delta p_8$ for varying γ_p, γ_q of a VDL at bus 8. The curves indicate that the dependence of $\breve{\gamma}_{p,8}$ on $\gamma_{q,8}$ is negligible. This result is general and we have confirmed it through several tests on different systems and loading conditions. From Figure 26, one can also deduce that the corrective factor in (3.14) is $\rho \approx 0.1$ whichis about the ratio R_{hk}/X_{hk} of the lines that connect bus 8 to the rest of the system. Figures 27, 28 show the performance of (3.14), (3.15) for several values of $\gamma_{p,8}$, $\gamma_{q,8}$.

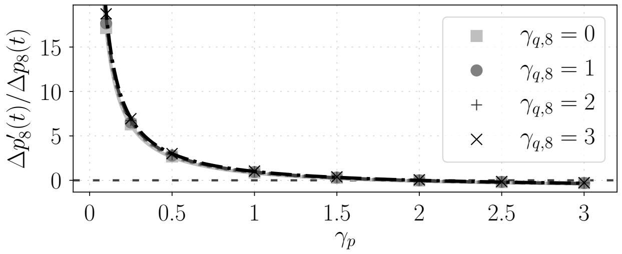

Figure 26 – Use Case FC_E.1 – Ratios of active power variations vs voltage exponents

We consider the case of VDLs connected at the DN level, for which the condition $B_{hk} \approx G_{hk}$

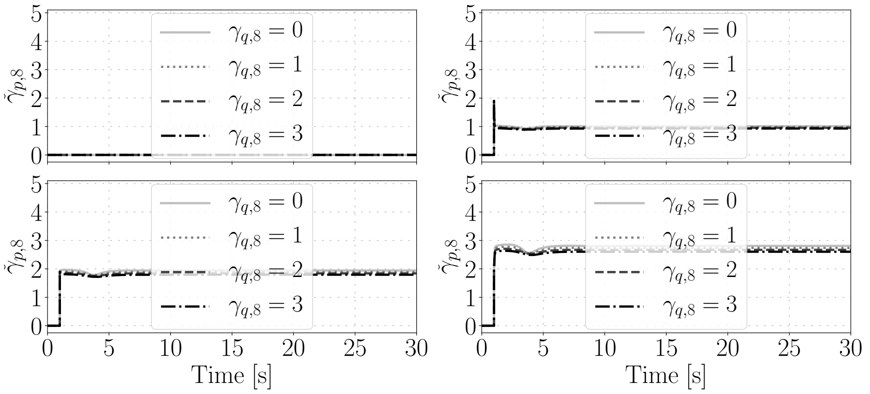

Figure 27 – Use Case FC_E.1 – From left to right and top to bottom, $\check{\gamma}_{p,8}$ $(\gamma_{p,8} \in \{0,\ 1,\ 2,\ 3\})$

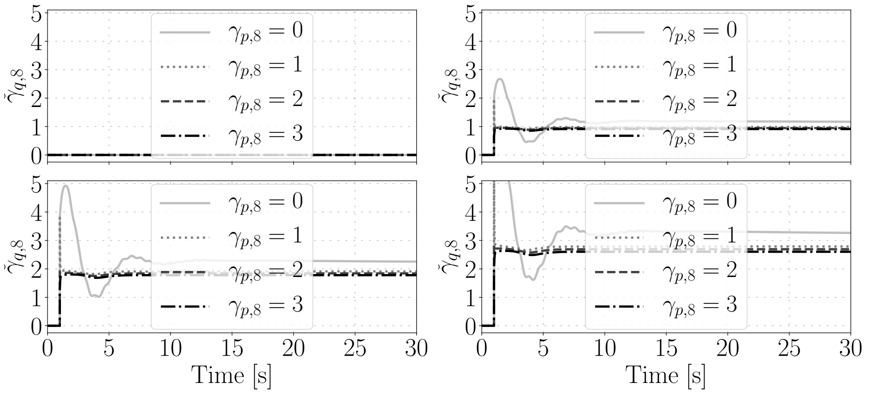

Figure 28 – Use Case FC_E.1 – From left to right and top to bottom, $\check{\gamma}_{q,8}$ $(\gamma_{q,8} \in \{0,\ 1,\ 2,\ 3\})$

holds. With this aim, the IEEE 14-bus system is considered for simulations. This system includes a region at 13.8 kV (buses 7 and 9-14), the lines of which are characterized by a ratio $R_{hk}/X_{hk} \in [0.47, 0.63]$, with some lines with a ratio greater than 1 (line 12–13). Figure 29 shows the ratio $\Delta p'_{14}/\Delta p_{14}$ calculated at the end of the simulation for a range of values of γ_p. The contingency is the disconnection of the load at bus 5. Based on several tests, we have determined that $\rho \approx 0.35$ for systems where $R_{hk}/X_{hk} \approx 1$. Figures 30 and 31 depict the estimated voltage exponent of the active power component of the VDLs at buses 14 and 12, respectively. The accuracy of the estimation is overall very good, although it slightly decreases for higher values of γ_p.

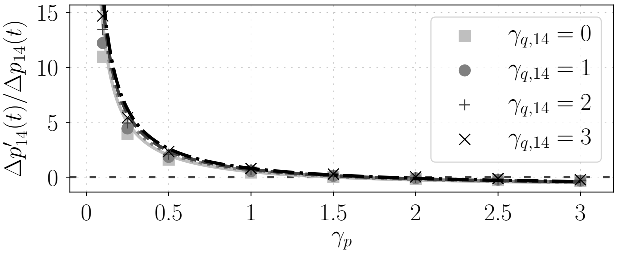

Figure 29 – Use Case FC_E.2 – Ratio of active power variations vs voltage exponents

A.4.2.3.2 Comparison of (3.14), (3.15) with (3.13)

Figure 32 shows the results obtained for the WSCC system where the load at bus 8 is a VDL with $\gamma_p = 2$ and $\gamma_q = 1.5$. The transient refers to the disconnection of 15 % of the load at bus 5. Results show that (3.13) is, as expected, more precise than the approximated expressions (3.14), (3.15).

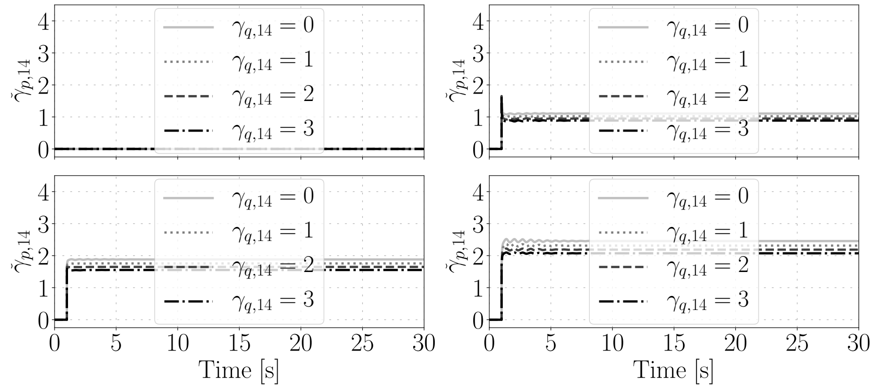

Figure 30 – Use Case FC_E.2 – From left to right and top to bottom, $\breve{\gamma}_{p,14}$ $(\gamma_{p,1} \in \{0,\ 1,\ 2,\ 3\})$

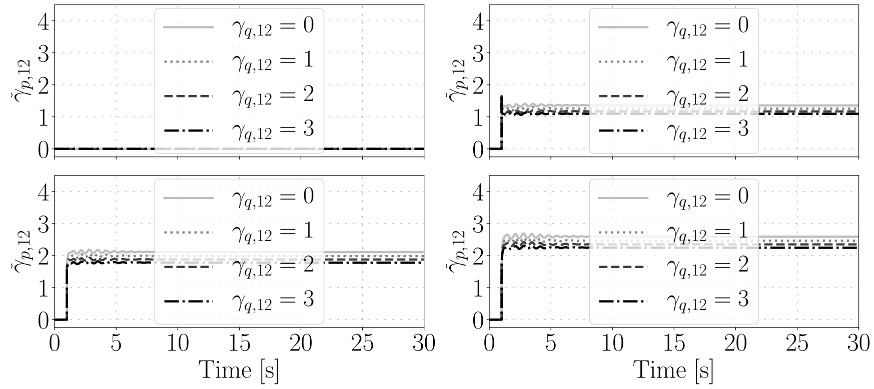

Figure 31 – Use Case FC_E.2 – From left to right and top to bottom, $\breve{\gamma}_{p12}$ $(\gamma_{p,12} \in \{0,\ 1,\ 2,\ 3\})$

Equation (3.13) is, in fact, an exact expression and its accuracy depends exclusively on the accuracy of the measurements of $\bar{\zeta}_h$, $\bar{\zeta}_k$. If the R/X ratio of the transmission lines of the system is changed to resemble that of a DN, (3.13) appears also numerically more robust than its approximated counterparts, see Figure 32b.

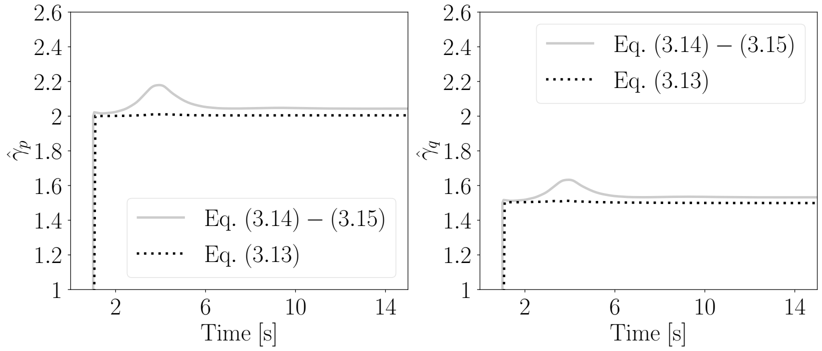

(a) Ratio of transmission lines: $R/X \ll 1$

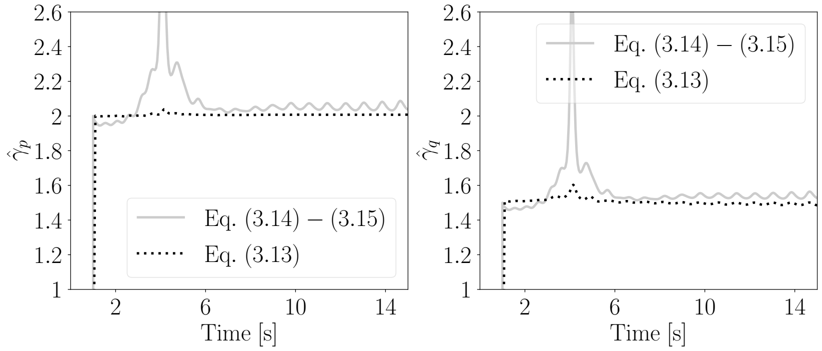

(b) Ratio of transmission lines: $R/X \approx 1$

Figure 32 – Use Case FC_E.1 – Estimation of VDL at bus 8

A.4.3 Aggregated VPP Model

A.4.3.1 Model Validation

A real-time simulation in Matlab/Simulink is utilized in this section to validate the proposed aggregation model against a fully-fledged Electromagnetic Transient (EMT) VPP model. The tested VPP is shown in Figure 33. It consists of 2 GFL-DGs, 2 GFM-DGs and 4 loads connected to an infinite bus, which is modeled as an ideal voltage source with controlled frequency and voltage. The nominal frequency is 50 Hz. The base voltage is 10 kV and the base power is 1 MW. DG parameters, aggregated voltage/current source model settings, and DG converter parameters are given in [39].

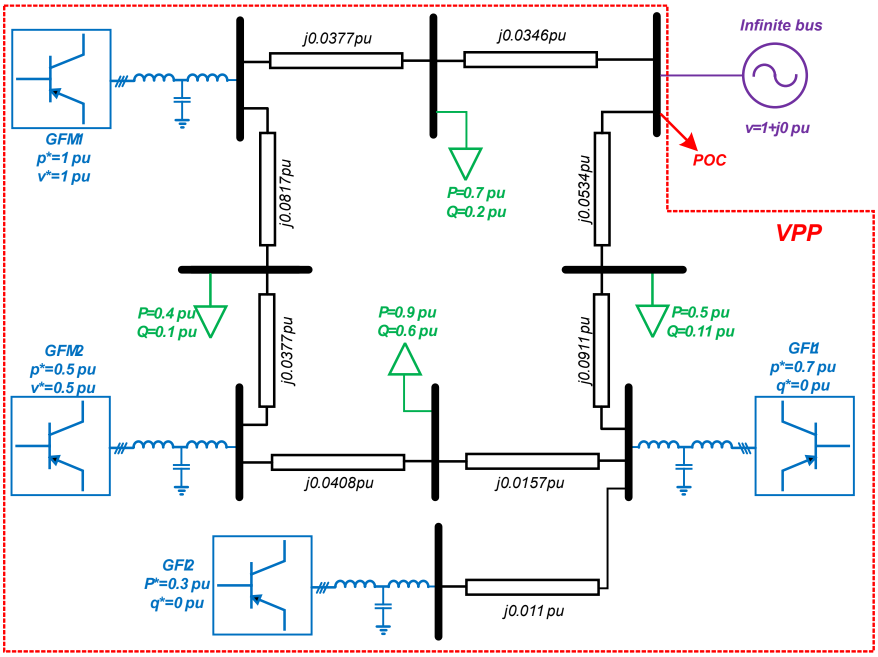

Figure 33 – VPP topology for EMT simulation

We show the accuracy of the aggregated model in response to a frequency variation at the POC. The initial steady-state is characterized by 50 Hz frequency and 1 pu voltage at the POC. At $t = 2$ s, the frequency of the ideal source starts decreasing from 50 Hz s to 49.85 Hz with a 0.3 Hz/s slope. The frequency variation stops at $t = 2.5$ s. Figure 34 compares the total active power of the GFL-DGs (GFM-DGs) of the detailed model and the aggregated current (voltage) source model. The aggregated models capture accurately the overall VPP dynamics.

Figure 35 shows the reactive power transients of the detailed and aggregated models. Both detailed and aggregated models present a reduction of the reactive power. This reduction is due to the power coupling of the GFMs and the VDLs. Although the voltage level of the aggregated voltage source is set to match the initial reactive power of the detailed model, local GFM-DG voltages may be different in the detailed model. Consequently, the reactive power response shows some small difference in the two models, see (4.11). Similarly, as mentioned above, the aggregated load voltage may be different from the local voltages of the actual loads. These are the reasons why Figure 35 shows a reactive power mismatch between the aggregated and the detailed model. However, the voltage mismatches in the GFM-DGs and/or in the load are very small and thus negligible.

We verify the accuracy of the aggregated model in response to voltage step variations. The initial steady-state is characterized by 50 Hz frequency and 1 pu voltage at the POC. The voltage of the ideal source jumps from 1 pu to 0.9 pu at $t = 2$ s and recovers to 1 pu at $t = 2.5$ s. Figure 36 shows the active power transients following the voltage variations. The dynamic response of the GFL-DGs show two aspects: (i) the negative feedback of the PLL synchronization; and (ii) the reactive power compensation. Because of these effects, the active and reactive powers of the GFL-DG are coupled during the transient. This leads to the spike in the active power at the instant of the voltage change. The aggregated model shows a lower peak on the active power than the detailed VPP,

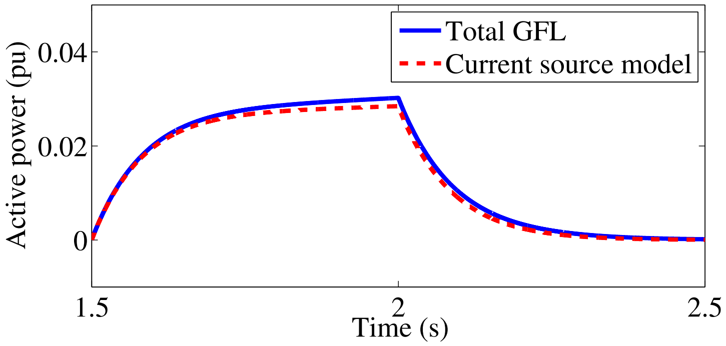

(a) GFL-DGs vs aggregated current source model

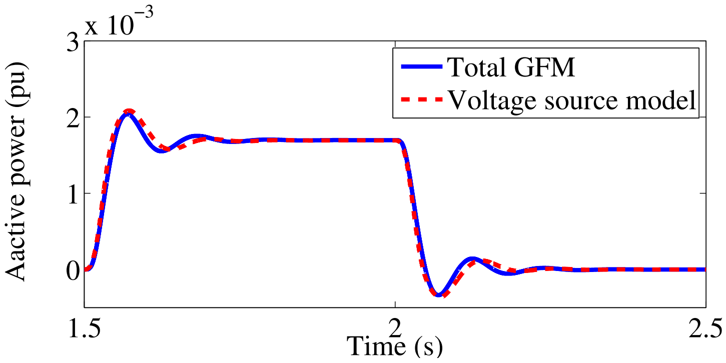

(b) GFM-DGs vs aggregated voltage source model

Figure 34 – Active power transient response after a frequency variation

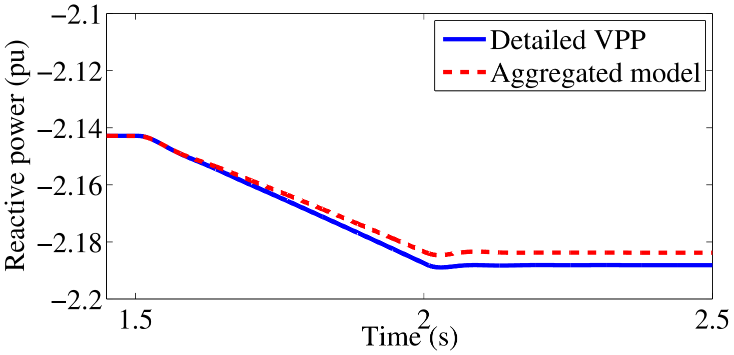

Figure 35 – Reactive power transient response after a frequency change

because it neglects the transients of the current controller.

With regard to the GFM-DGs, the steps in the voltage activates the AVR that, as a consequence, increases the output voltage of the DGs. This voltage regulation leads to the active power change as indicated in (4.11). Then the power synchronization of the GFM-DG moves the phase to re-track its power reference. This transient behavior is well reflected in the aggregated voltage source model. The sub-transient oscillation is due to the dynamic coupling between the swing equation and the system impedance [33]. This behavior is also accurately captured by the aggregated model.

Figure 37 shows the reactive power transient of the detailed and aggregated VPPs. The voltage support of the VPP compensates the reactive power following the POC voltage change. The aggregated model accurately captures such a reactive power compensation. Since the grid voltage before $t = 2$ s and after $t = 2.5$ s is the same, the reactive power trajectories at post fault are perfectly matched. However, during the POC voltage sag, there is a small mismatch due to the different voltage levels in the VPP grid. Again, this mismatch is small and does not affect the overall

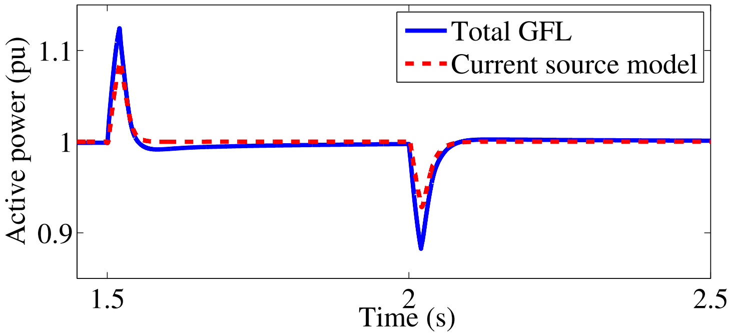

(a) GFL-DGs vs aggregated current source model

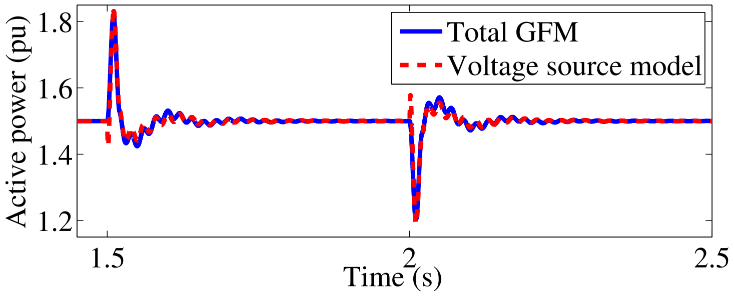

(b) GFM-DGs vs aggregated voltage source model

Figure 36 – Active power transient response after voltage variations

accuracy of the aggregated model.

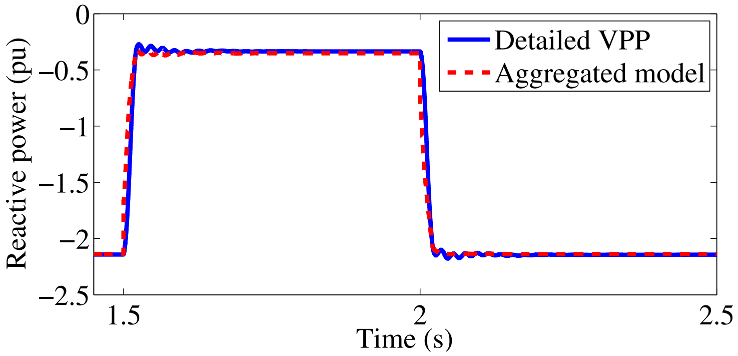

Figure 37 – Reactive power transient response after voltage variations

A.4.3.2 Results

The VPP and its aggregation model parameters used in this section are given in [39]. We first consider the outage of Gen 8. Figure 38 shows the trajectories of the grid frequency, the active power and reactive power of VPP 1 at its POC, and the voltages at nearby grid buses. The active power response of the VPP can be accurately captured by the aggregated model, as shown in Figure 38b, so that the grid frequency response (see 38a) is identical to the one obtained with the detailed model. On the other hand, as expected, the reactive power, e.g. see 38d, obtained from the aggregated model shows a small mismatch with respect to that of the detailed VPP, thus, resulting in a small mismatch on the voltage response, as shown in Figure 38c.

We now consider the outage of the load at bus 8. To avoid repetitions, we only show the system frequency and bus voltages. Since after the contingency generation is greater than the consumption, the system frequency increases. The aggregated model accurately captures such a dynamic response of the frequency as well as the voltage response as shown in Figure 39.

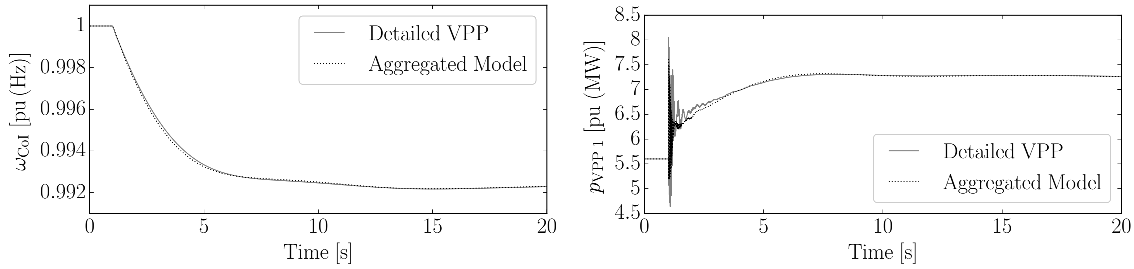

(a) System frequency **(b) VPP1 active power at POC**

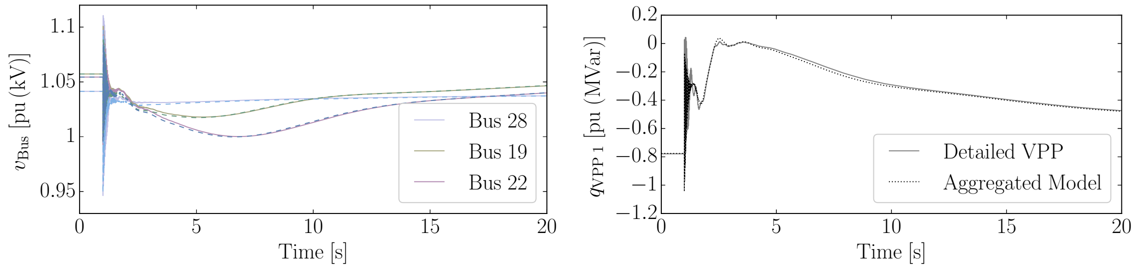

(c) Bus voltages **(d) VPP1 reactive power at POC**

Figure 38 – Use Case FC_B.2 – Generator outage

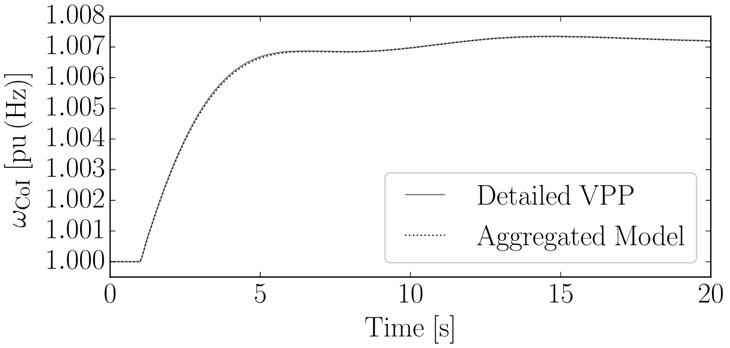

(a) System frequency

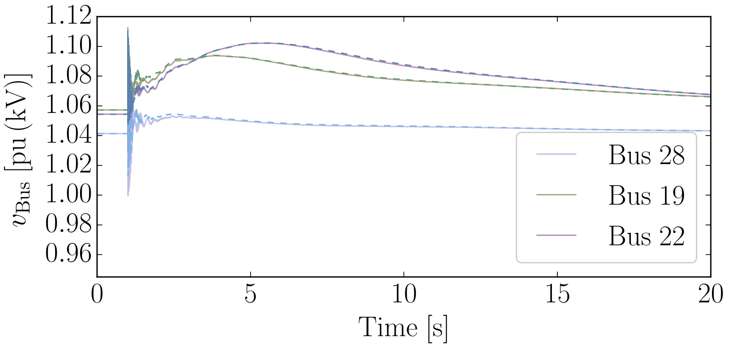

(b) Bus voltages

Figure 39 – Use Case FC_B.2 – Load outage

We finally consider the outage of the line connecting buses 2 and 25. Figure 40 shows the response obtained with the detailed and the proposed aggregated model. In this case, the frequency response of the aggregated model presents a mismatch in the first 7 s after the contingency. This mismatch is due to the converter control dynamics (see also the EMT results discussed in Section A.4.3.1).

Note, however, that the mismatch is very small both in percentage and absolute values.

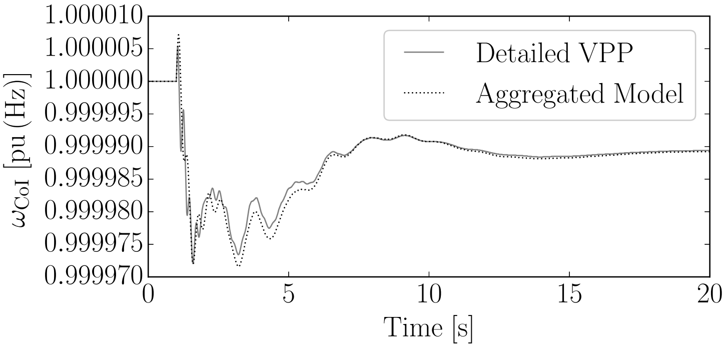

(a) System frequency

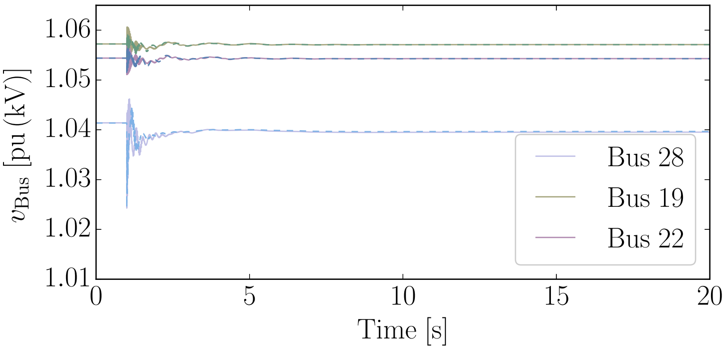

(b) Bus voltages

Figure 40 – Use Case FC_B.2 – Line outage

A.4.4 Decentralized Charging of PEVs

This section presents simulation results on the PEV charging strategy presented in Chapter 5.

A.4.4.1 Uncontrolled Charging

The evening ramp due to the PEVs domestic charge may cause a system collapse, if it is uncontrolled [46]. To simulate such a situation, we assume that PEVs are equally distributed among buses 3, 4, 7, 8 and 12, see Figure 7, and that the arrival rate of PEVs for charging is about 120 veh/s, i.e. after 1 hour of simulation, about 432,000 PEVs are connected for charging. Estimating the total number of cars in New England to $5 \cdot 10^6$ vehicles,[1] this corresponds to assuming that about 8-9% of the total number of cars connect for charging during the evening peak within an hour. Note that we do not give an exact starting time for the evening domestic charging scenario, as this may vary from country to country depending on local habits (e.g., dinner time).

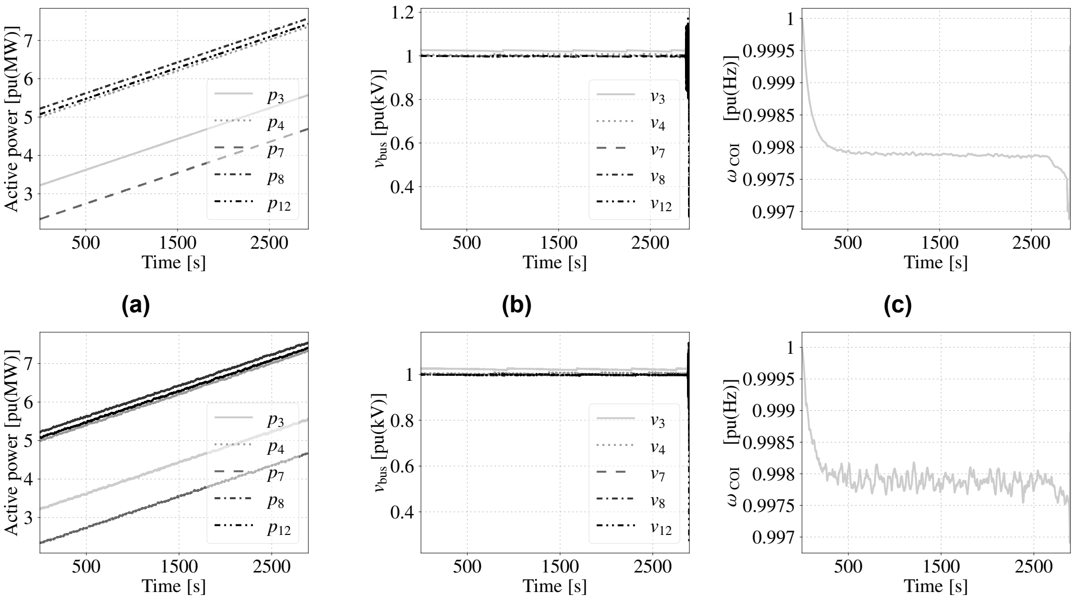

(a) (b) (c)

(d) (e) (f)

Figure 41 – Use Case FC_C.1 – Uncontrolled charging of PEVs; (a) and (d): nodes power load profile; (b) and (e): nodes voltage response; (c) and (f) ω_{COI}. The lower row shows results for a system with noise ten times higher than the upper row

Figures 41a-c show that the system is not able to cope with such a large volume of PEVs, and it finally collapses. Predicting the upcoming instability may not be easy, as the voltages and the COI frequency remain very close to their nominal values, even right before the collapse (see Figure 41b and Figure 41c). In particular, Figure 41(b) shows that the behavior of the voltage values is mainly affected by the action of the ULTC devices. Also, we can observe that the system behavior is independent of the Gaussian process parametrization, which characterizes the load ramp equation – see (A.1). Actually, we get quite the same results if we use a standard deviation ten times higher (see Figures 41d-f) for instance. A careful handling of the reactive power is critical in the problem of charging PEVs in transmission networks. The SVCs included in the system prevent limit-induced bifurcations due to reactive power shortage. So the instability shown in this scenario refers to congestion in the transmission lines (saddle-node bifurcation) [72].

The analysis above can be conveniently carried out using a steady-state analysis, such as the well-known continuation power flow technique [73]. The goal of this simple example, however, is to show that the relatively slow time-scale of the PEVs ramp as well as the small capacity of each individual PEV prevent utilizing the frequency of the system, or the voltages of the buses, as reliable signals

---

[1] https://www.fhwa.dot.gov/policyinformation/statistics/2016/mv1.cfm#foot3

to implement a “smart” control. For this reason, as mentioned in advance, in the next sections we shall show examples where only power signals are used for control purposes. Finally, this example indicates that it is not enough to insert SVCs close to the charging points, as the intrinsic transfer capability limit of the grid cannot be avoided and is thus binding.

A.4.4.2 Synchronized AIMD

We consider the power-based AIMD controller described in Section 5.2, where safety thresholds for the system are defined as a function of the static limits, i.e., the maximum power at load buses. The synchronized AIMD appears as the best approach to solve the problem, as all PEVs have the same priority and should be charged on average with the same power rate. In this section, we present the system behavior using the same settings as in Section A.4.4.1, with the action of the synchronized controller; the parameters of the AIMD are $\alpha = 0.34$ W, $\beta = 0.99$ and the threshold that triggers CEs is $p_s^{\max} = 180$ MW. The values of α and β are the same in all simulations. In practice, the grid operator can tune these parameters as a trade-off between power efficiency (i.e., optimal utilization of the available power) and communication requirements (to prevent the system from frequently showing CEs). Finally, the static limit $p_s^{\max}$ of each bus is set equal to 80% of the actual bus power limit, assuming that grid operators will be conservative in estimating the maximum available power.

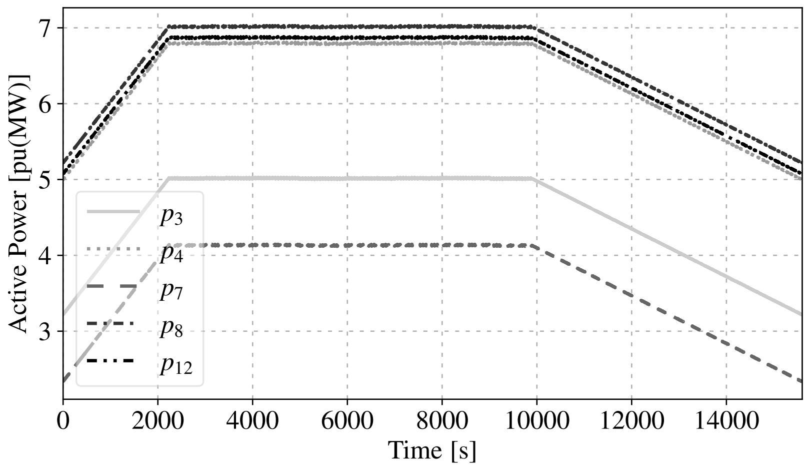

(a)

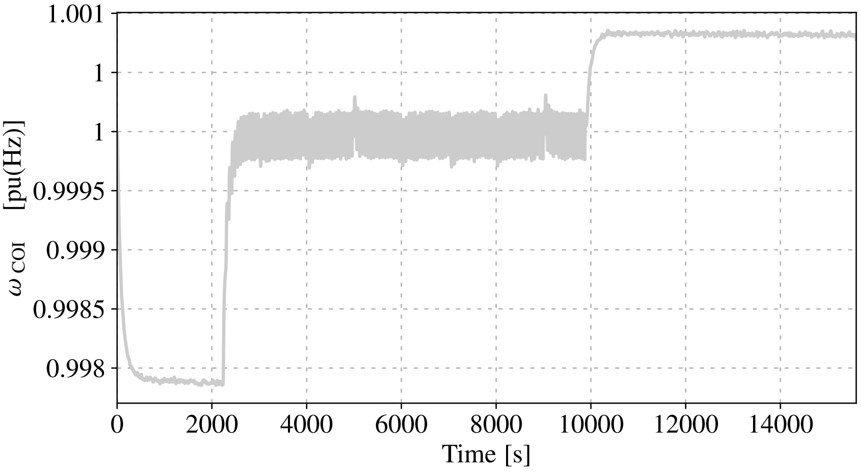

(b)

Figure 42 – Use Case FC_C.1 – Synchronized AIMD; (a) load active power at PEV buses; (b) $\omega_{\rm COI}$ response

Figure 42 summarizes the results obtained; the proposed control successfully accomplishes the charging task, as the control action prevents the power limit from being exceeded. Also, note that during the charging process, the frequency signal ω_{COI} lies within the safe range [0.996, 1.004] pu (Figure 42b). Several simulations have been performed to validate these results, for different values of loads, and different PEV spatial distributions: similar results have been obtained and thus are not reported here. Moreover, we note that selection of parameters or thresholds does not change the main conclusion, i.e. the control strategy is effective to prevent the system collapse.

The determination of the maximum loading condition, namely $p_s^{\max}$, of a grid is an analysis that is commonly carried out by system operators, independently from the presence of PEVs in the grid. This analysis is aimed at determining the available loading condition or, equivalently, the voltage stability margin of the grid. We thus assume that the system operator has a good knowledge of the grid and defines $p_s^{\max}$ based on an analysis of the “available transfer capability”, this takes into account an N-1 contingency analysis and the “transmission reliability margin” as defined by NERC [74]. Of course, $p_s^{\max}$ varies for different topologies of the grid but these are events that require updating the AIMD parameters periodically. For simplicity, however, in the simulations presented in the manuscript, we assume that $p_s^{\max}$ does not change during the PEV ramp-up. It should be noted that system operators often decrease the estimated value of $p_s^{\max}$ for security reasons. In the context of PEV charging, the lower the maximum loading condition limit $p_s^{\max}$, the longer the time required to charge all PEVs than strictly needed. On the other hand, the value of $p_s^{\max}$ is never increased as this would lead to a potential security issue for the grid.

We provide a simple example which further supports that a frequency-based PEV charging control may be inappropriate, as it may give rise to stability issues. In particular, we consider the same case as in Section A.4.4.2, but the AIMD algorithm is performed with respect to the bus frequencies, and a CE (and consequent reduction of power consumption by the connected PEVs) occurs when the frequency falls below a certain threshold. We assume $\omega^{\min} = 0.999$ pu. When PEVs increase their charge rates, the frequency decreases. For this reason the threshold corresponds to a minimum allowed frequency (and not a maximum overall power).

Figure 43 summarizes the obtained results. In particular, the charging process is very slow because a very conservative threshold for the frequency was chosen, and thus only very small load changes are allowed. Despite the conservative frequency threshold, the system collapses, despite its response to reduce the charge rates of the connected PEVs. Several simulations, solved with different thresholds, confirm that small variations of charging powers do not significantly impact on the system frequency, and more importantly, that a local frequency-based strategy may not be appropriate for PEV charging control to avoid line congestion.

A.4.4.3 Unsynchronized AIMD

The unsynchronized AIMD is more interesting than its synchronized version, as it makes possible to prioritize PEVs as desired. This allows implementing policies that favor certain PEVs (for instance because their owners are willing to pay more to be charged earlier) or taking into account energy requirements of the PEVs, or of the power grid). We now assume again that PEVs are equally distributed and connected to buses 3, 4, 7, 8 and 12. The following two cases are compared:

- all PEVs at bus s have the same objective function:

  $$f_s(p_{i,s}) = -\frac{p_{i,s}^3}{3 \cdot p_{\max}}, \tag{A.16}$$

  where $p_{i,s}$ is the power load of the i-th PEV plugged at bus s, and $p_{\max}$ is the maximum charge rate (i.e., 3.3 kW, as described in Section 5.4).

- all PEVs connected to buses 3, 4 and 7 have UF f_{s_1}, while PEVs connected to buses 8 and 12 have UF f_{s_2}, where:

  $$f_{s_1}(p_{i,s}) = -\frac{p_{i,s}^3}{3 \cdot p_{\max}}, \quad f_{s_2}(p_{i,s}) = -\frac{p_{i,s}^4}{4 \cdot p_{\max}^2}. \tag{A.17}$$

In both scenarios, up to $88 \cdot 10^3$ PEVs connect for charging at each bus. We assume $\Gamma = -1$. Fig-

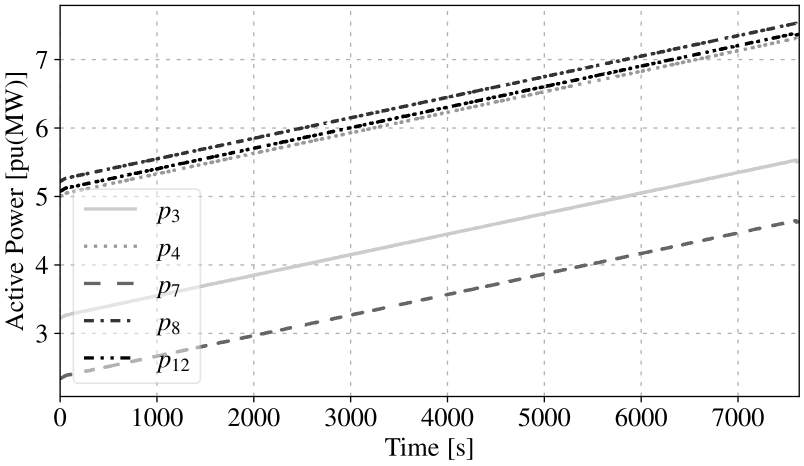

(a)

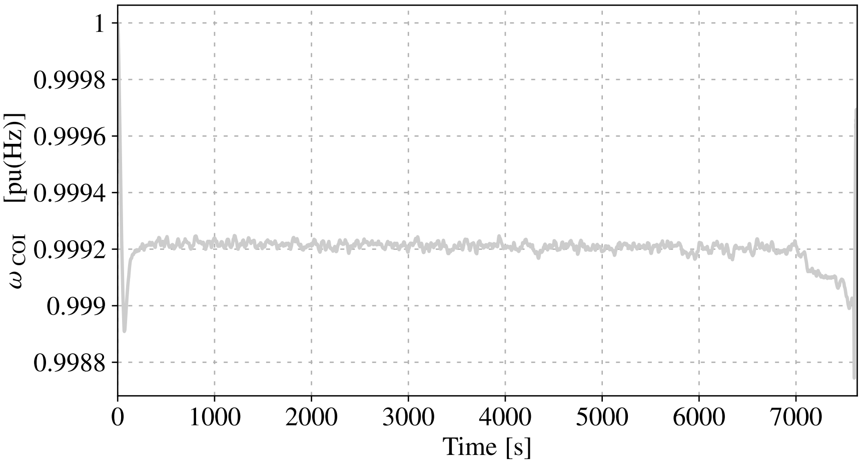

(b)

Figure 43 – Use Case FC_C.1 – Results of the synchronized AIMD frequency-based version; (a) active power of loads at PEV buses; (b) frequency ω_{COI} response

ure 44 summarizes our results for the examined cases. The effect of the different objective functions can be noticed by comparing Figure 44a, where the algorithm fairly manages to complete charging at all buses at about the same time, and Figure 44c, where PEVs with steeper UF (prioritized PEVs) finish earlier than PEVs of other buses. Hence, results confirm qualitatively our expectations. To better appreciate the effect of the prioritization in a quantitative way, we compare the 5 buses characteristics also in Table 4. In addition, Figures 44b and 44d show that the frequency always lies in a safe range [0.998, 1.001] pu. These results show that by designing steeper, or less steeper UFs, it is possible to prioritize some vehicles, if desired, as an alternative to a fair approach.

A.4.4.4 Different Priorities at the Same Bus

The previous example assumes that all PEVs connected to the same bus have the same UF. While this is convenient to illustrate the proposed control strategy, in practice, PEVs connected to the same bus may have different UFs. In this section, we consider that PEVs are equally distributed and connected to buses 3 and 4. At each bus, half of the PEVs have UF f_{s_1} and the other half have UF f_{s_2} (see (A.17)). Figure 45 shows the system behavior in terms of the power loads at buses 3-4. The control strategy is effective, as with the same number of PEVs, the power grid would have collapsed in an uncontrolled scenario. Moreover, prioritized PEVs finish charging earlier than those without priority, independently from the bus to which they are connected.

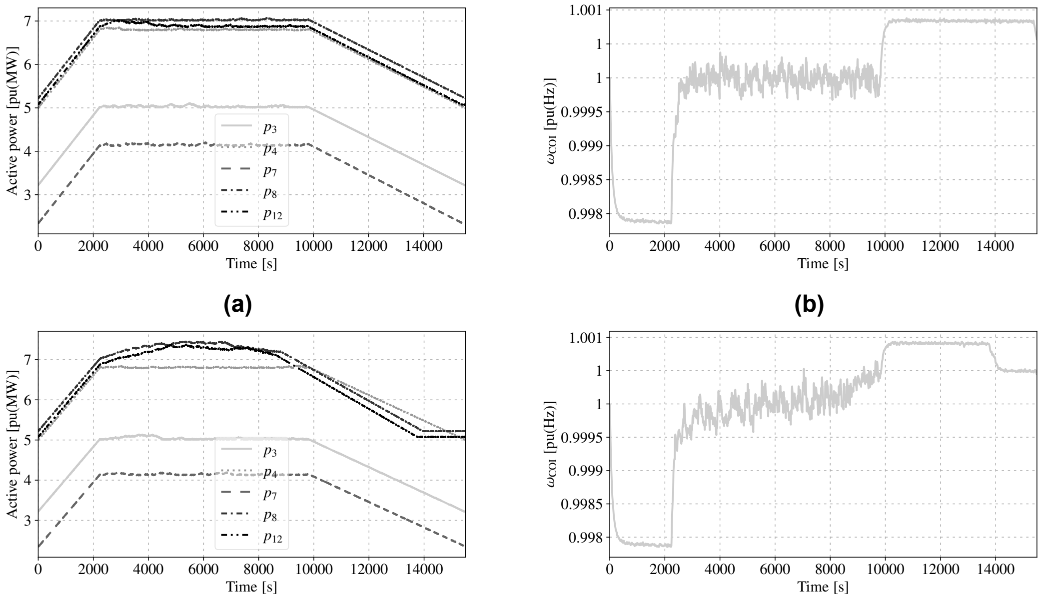

(a) (b)

(c) (d)

Figure 44 – Use Case FC_C.1 – Unsynchronized AIMD; (a) load active power at PEV buses, control without priorities; (b) ω_{COI}, control without priorities; (c) load active power at PEV buses, control with priorities; (d) ω_{COI}, control with priorities

Bus #	Mean power rate (kW)	Global charge duration
3	1.537	4 hours, 18 minutes
4	1.531	4 hours, 19 minutes
7	1.530	4 hours, 19 minutes
8	1.702	3 hours, 53 minutes
12	1.727	3 hours, 49 minutes

Table 4 – Use Case FC_C.1 – Unsynchronized control performance with priorities

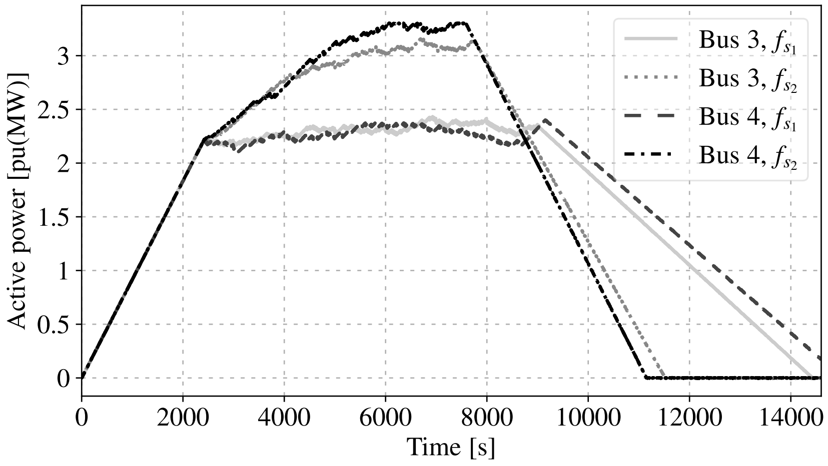

Figure 45 – Use Case FC_C.1 – Active power of PEV subgroups at buses 3 and 4